Design of the Secondary Mirror Support Structure

for the Deployable Space Telescope

A. Krikken

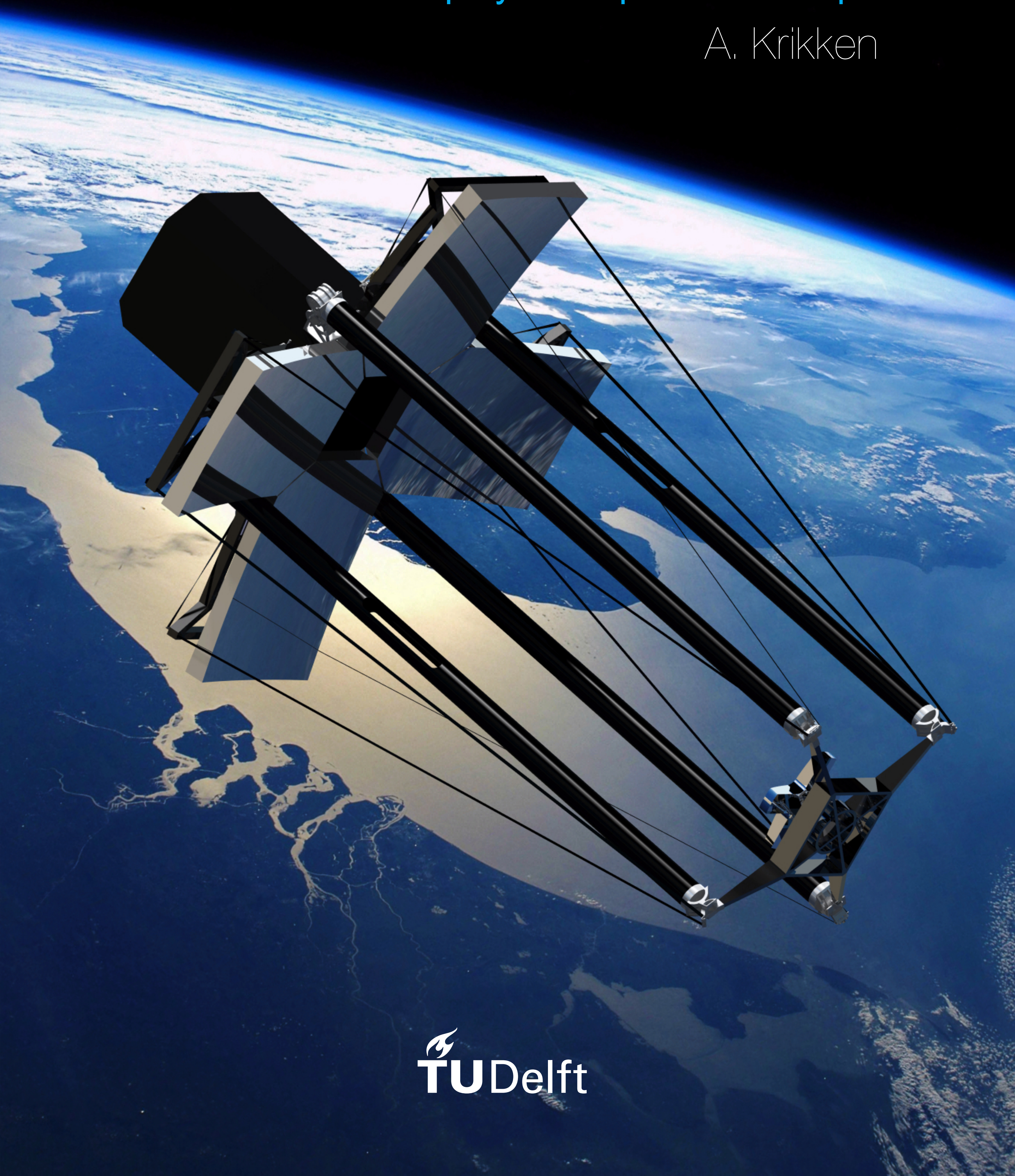

TU Delft

Design of the Secondary Mirror Support Structure
for the Deployable Space Telescope

by

A. Krikken

to obtain the degree of Master of Science
at the Delft University of Technology,
to be defended publicly on Monday July 9, 2018 at 14:00.

Student number:	4147235	
Project duration:	September 1, 2017 – July 9, 2018	
Thesis committee:	Prof. dr. E. K. A. Gill,	TU Delft, SSE, Chair
	Dr. ir. J. M. Kuiper,	TU Delft, SSE, supervisor
	Ir. B. C. Root,	TU Delft, AS

This thesis is confidential and cannot be made public until July 7, 2019.

Front cover: Background image courtesy of NASA

TU Delft

Summary

In the modern world, the need for Earth observation data is getting bigger and bigger. To fulfil the demand of high resolution Earth surface images, the spacecraft mass and volume are high due to the required large diameter of the primary mirror and long focal length of the telescope. The Deployable Space Telescope (DST) project aims to reduce the mass and volume of the spacecraft in stowed configuration, without reducing the performance of the telescope. In the design of the DST, the secondary mirror has to deploy before operations. In previous work, it was decided to use articulated booms for the deployment of the secondary mirror. This design was in a conceptual phase. In this thesis, the secondary mirror support structure (SMSS) was designed in more detail.

It was decided to investigate a three boom, exactly constrained design. For this design, a trade-off for the mid hinges was performed. Three concepts were considered: ball bearing hinges, integral slotted hinges, and shape memory composite (SMC) hinges. The trade-off was partially based on a modal analysis and the result was the selection of the integral slotted hinges. The working principle of these hinges rely on the elastic deformation of the boom material and thus the hysteresis in the hinge is low. Furthermore, since the hinge is part of the booms, this concept is a light weigth solution.

For the top and root hinges of the SMSS, four concepts were considered: Integral slotted hinges, large deflection flexures, ball bearing hinges, and Compliant Rolling-contact Element (CORE) hinges. The trade-off between the concepts resulted in the selection of the CORE hinge concept for both hinges. This concept was designed in detail. Three design parameters were identified: the bending radius of the strips, the total strip width, and the strip thickness. These parameters were optimised for the applied load cases. A final detailed design was made for both hinges. The preload on the strips was applied to the strips with a combination of bolt tension and belleville washers. This method of applying the preload was selected from five different concepts.

The mirror interface concept was selected to be a hexapod structure. The length of the mirror mount is made such, that the total system is athermal. This reduces the effect of bulk temperature change to the system. This however does not reduce the effects of thermal gradients within the system.

In the results from the modal analyses it was observed that the spider tends to translate significantly during vibrations. In order to minimise this motion, ribbons were introduced to the design. The ribbons span between the primary mirror support structure (PMSS) and the SMSS. Since the ribbons attach to the PMSS, the number of booms was again increased to four. In the three booms concept, the ribbons would introduce a torsional load on the PMSS, which was deemed unwanted. The effect of these ribbons were investigated using an harmonic analysis. The result was a significant reduction of the amplitude of the secondary mirror motion. It was reduced from 25.4 micron to 0.73 micron, which means that the system fulfils the optical stability requirements.

The overall mass of the sysem was reduced from 12 to 7.8 kg compared to the previous design iteration.

Preface

I worked on this thesis during this last year. The thesis is the conclusion of my years at the Delft University of Technology and I look back on this period with a lot of joy. It is the period where I first lived on my own, lived abroad for a full year in total, and met a lot of amazing people.

First of all, I would like to thank my supervisor Hans Kuiper for his support and his believe in my independence and my ability to contribute to the DST project. Further, I would like to thank Dennis Dolkens and Victor Villalba Corbacho for their support and feedback on my work. I would also like to thank Victor for his mental support by asking me every day how my life was.

I would also like to thank Henk Cruijsen and Guus Borst from Airbus Defence and Space for their useful feedback on the designs and method I presented. A special thanks goes out to Pierrot Greff from SpaceTech for the discussion on the integral slotted hinges. This discussion proved to be very helpful in the trade-off for the mid hinge and helped me to get the momentum back in my thesis. I would also wish to thank Just Herder from the faculty of 3ME at TU Delft for making time for discussions about hinge concepts and the SMSS in general. The discussions with Just Herder proved to be critical in the development of the SMSS, and with that on the results presented in this thesis for which I am really thankful.

Apart from my supervisors, I would like to thank my fellow DST and MSc. thesis students on the 8^{th} floor for their support, and of course the *gezelligheid*. This helped me through the periods where the thesis work went less smooth. Besides the welcome *banana time* breaks at 4 o'clock, I am going to miss the karaoke nights at *De Koperen Kat*.

I want to thank all my friends and family who supported me throughout not only the thesis, but my entire student life. I especially want to thank my parents for always supporting me in whatever I do. Even when I suddenly decided to study half a year in Sweden, decided out of the blue to take a gap year at the Eco-Runner Team Delft, or suddenly decided to do my internship in Denmark, I could always count on their support.

Contents

List of Figures

List of Tables

List of Symbols

	Roman alphabet	
Symbol	**Description**	**Unit**
A	Area	m^2
$A_{z,0}$	Azimuth angle of centre eclipse	rad
$A_{z,eclipse}$	Azimuth range eclipse	rad
a	Acceleration	m/s^2
b	Width flexure	m
b	Herzian contact parameter	-
CTE	Coefficient of thermal expansion	micron/m/K
c_{eq}	Equivalent damping coefficient	-
E	Young’s modulus	GPa
F	Force	N
f	Force vector	-
f_n	Natural frequency	Hz
G	Shear modulus	GPa
h	Pitch screw	-
h	Height	m
I	Area moment of inertia	m^4
K	Torsional constant	m^4
k	Spring stiffness	N/m
l	Length	m
M	Moment	Nm
m	Mass	kg
P	Compression load	N
P_{max}	Maximum contact pressure	MPa
R	Radius	m
r	constraint position vector	m
SF	Safety factor	-
T	Twist	-
t	Thickness	m
t	Time	s
U_{max}	Maximum delfection	m
W	Wrench	-
w	Width	m
X	Length CFRP	mm
X	Response amplitude	m
Y	Length mirror interface	mm
Y	Base amplitude	m

	Greek alphabet	
Symbol	**Description**	**Unit**
α	Solar absorbtivity	-
β	Solar beta angle	rad
β_c	Variable stiffness multiplier	-
β_s'	Angle between the sun and orbit pole	rad
Γ	Reciprocity matrix	
γ	Angle between surface normal and orbit pole	rad
ΔA_z	Azimuth difference surface normal and sun	rad
ΔE	Material hysteresis energy loss	J
ΔF	Difference preload force	N
δ	Deflection	m
ϵ	Absorbtivity	-
ΔT	Temperature difference	k
η	Material loss factor	-
Θ	Beam delfection angle	rad
θ	Strip angle in CORE hinge	rad
ν	Poisson's ratio	-
ξ	Constant damping ratio	-
σ	Normal stress	MPa
σ'	Von Mises stress	MPa
σ_{cr}	Critical buckling stress	MPa
τ	Shear stress	MPa
ω	Angular velocity	rad/s

List of Abbreviations

ADS	Airbus Defence and Space
AHP	Analytic Hierarchy Process
AIT	Assembly, Integration , and Testing
CFRP	Carbon Fibre Reinforced Polymer
CORE	Compliant Rolling-contact Element
CTE	Coefficient of Thermal Expansion
CTM	Collapsible Tube Mast
DM	Deformable Mirror
DOF	Degree of Freedom
DST	Deployable Space Telescope
EOL	End of Life
FBD	Free Body Diagram
FBS	Functional Breakdown Structure
FFD	Functional Flow Diagram
HDRM	Hold-Down Release Mechanism
ITAR	International Traffic in Arms Regulations
IXO	International X-ray Observatory
JWST	James Webb Space Telescope
LEOP	Launch and Early Operations
M1	Primary Mirror of the DST
M2	Secondary Mirror of the DST
M3	Tertiary Mirror of the DST
PMSS	Primary Mirror Support Structure
RAAN	Right Ascension of the Ascending Node
RDT	Requirement Discovery Tree
RPM	Rotations Per Minute
SMC	Shape Memory Composite
SMSS	Secondary Mirror Support Structure
TBC	To Be Confirmed
TBD	To Be Determined

1
Introduction

Modern day life depends more and more on the availability of all sorts of data. One of these forms of data is high resolution images of the Earth surface. These images can for example be used for the investigation in deforestation, and the effects of natural disasters like forest fires, earthquakes, vulcanic eruptions etc. Other examples are the monitoring of farmlands or the monitoring of potential military interesting areas. The images are currently provided by large spacecraft like WorldView 4, which has a ground sampling distance of around 30 cm [14]. These large spacecraft have a monolithic primary mirror and a rigid, non-deployable structure. Due to launcher volume and mass limitations, the size of the primary mirror is limited, and with that the possible resolution of the images. Furthermore, the launch cost of these satellites is high. Currently, the Delft University of Technology is working on a deployable space telescope, in which the primary mirror is segmented. These segments are stored next to the spacecraft body during launch, which saves volume. The secondary mirror of the telescope is mounted on a deployable structure, again decreasing the volume of the telescope in stowed configuration.

This thesis describes the detailed design of the deployable secondary mirror support structure (SMSS). The thesis will continue the work performed by J.W. Lopes Barreto for his MSc. thesis. The focus in the thesis will be on the concept selection and detailed design of the hinges of the articulated boom system. During the design process, several analyses will be performed to check the effect of design parameters on the system behaviour.

The thesis is split into three parts. In the first part, the SMSS subsystem definition is presented. In this part, Chapter 2 will give the introduction to the DST project. In this chapter, the research objective and question of this thesis will also be given. In the following chapter, the requirements for the system will be discussed. These requirements form the base for the design, and the final design will be checked on these requirements. In Chapter 4, the standard load cases the system will be subjected to are given. These load cases form the basis on which the design will be made.
The thesis continues with the second part which discusses the design of the SMSS subsystem. In Chapter 5, the top level system design of the mechanism will be discussed, followed by a chapter on the conceptual design of the top and root hinges. These concepts form a baseline design used for the mid hinge trade-off given in Chapter 7. During the mid hinge trade-off, it was observed that certain design parameters might influence the stiffness of the system. These parameters are investigated in Chapter 8. Based on the results in Chapter 8, a design iteration was performed. This iteration is given in Chapter 9. In Chapter 10, the detailed design of the top and root hinges is given. The following chapter the effect of introducing ribbons to the design is investigated by performing an harmonic analysis on the concepts.
In the final part of the thesis, an overview of the final design is given, together with the conclusions and recommendations. In Chapter 12, the final design is summarised, and the system performance is checked with the requirements given in Chapter 3. Conclusions are drawn in Chapter 13, and recommendations are given in Chapter 14.

I

Secondary Mirror Support Structure Definition

2
DST Project Overview

The thesis that is presented in this report was performed as part of the Deployable Space Telescope (DST) project. The DST is a project of the Delft University of Technology. In this chapter, the overview of the mission will be given, starting with the mission background, where the motivation of the project will be explained. In the following section, the current design will be presented.

2.1. Mission Background

In the modern society of today, there is a constant need for up-to-date Earth observation data. There are multiple satellites that take images of the Earth surface in the visible spectrum, both military and commercial. A good example of a commercial Earth observing satellite is WorldView 2. This satellite takes images with a ground sampling distance of 0.46 m panchromatic and 1.85 m multispectral from an altitude of 770 km [15]. The next satellites in this family, the WorldView-3 and WorldView-4, have a ground resolution of 0.31 m panchromatic and 1.24 m multispectral at an altitude of 617 km [13, 14]. The performance of the WordView satellites is good, however the spacecraft are expensive. The satellites have both a high volume and mass. The WorldView-2 is 5.7 m tall and 2.5 m across in stowed configuration, while having a mass of 2615 kg [15]. WorldView-3 has similar dimensions, but has a mass of 2800 kg [13]. Both the high mass and large volume contribute significantly to the total cost of the missions. This issue can be captured in a need statement:

There is a need to bring down both the mass and volume of Earth observation satellites without a reduction in the resolution of the images.

The DST project aims to bring down both the stowed volume and mass of the telescope, without lowering the optical performance of the system. This is realised by making both the primary and the secondary mirror deployable. This decision was based on the observation that the large volume of the telescope is only useful in the operational phase of the mission. During the launch and transportation of the system, the volume does not have a specific purpose. The mission statement of the DST project can be summarised in the following mission statement:

The Deployable Space Telescope mission shall produce images of the Earth surface with a resolution comparable to the current state of the art (2017) while having a lower launch volume and mass than the convential Earth observation satellites (2017).

2.2. Team Structure & System Overview

The DST team consists of a mix of master and PhD students working on their theses. The team is supervised and managed by Hans Kuiper. The team is split in an optical and a mechanical subteam. The two PhD students (Dennis Dolkens and Victor Villalba Corbacho) are each responsible for one of the subteams. The team structure is given in Figure 2.1.

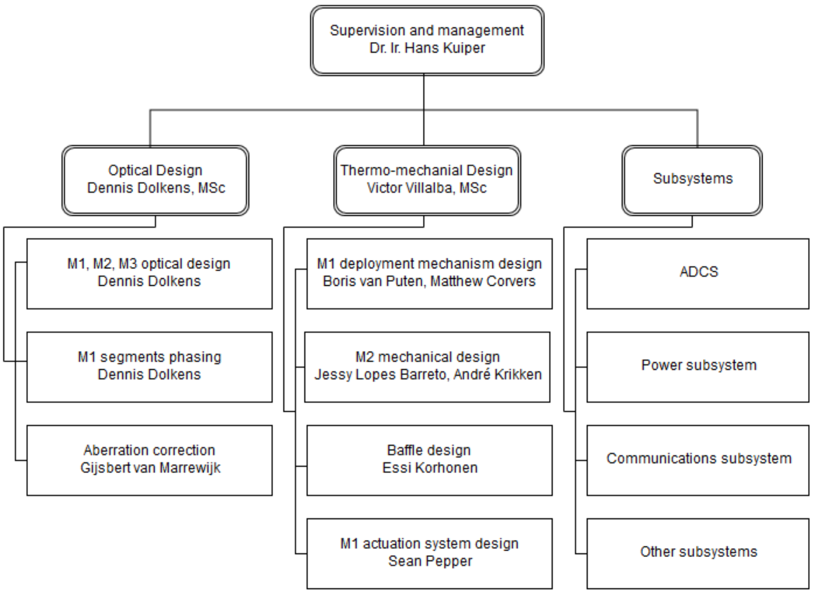

Figure 2.1: The team structure of the DST project. The image was taken from the internal document *DST engineering budget document*, and was made by G.P. van Marrewijk.

Before the previous design iterations are discussed, first an overview of the components within the DST will be given. The overview is given in Figure 2.2. In this figure, the different mirrors can be seen, together with a schematic representation of the structure supporting the mirrors.

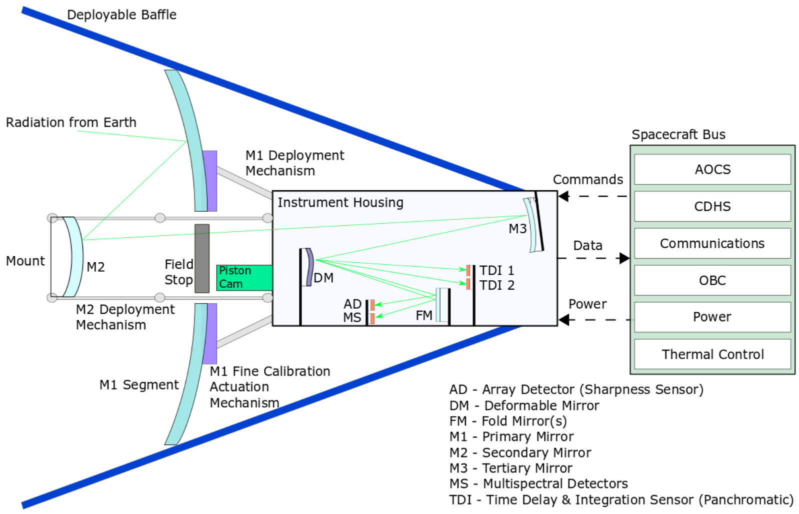

Figure 2.2: Schematic overview of the subsystems present within the DST. Image was taken from the nternal document *DST engineering budget document*, and was made by S. Pepper.

2.3. Previous Design Iterations

The first design of the DST was made by D. Dolkens in his MSc. Thesis. The first design had three primary mirror segments with the second mirror deployed using an articulated boom system. An impression of the first version of the DST is given in Figure 2.3 [16]. In a later design stage, it was decided by D. Dolkens to use four instead of three primary mirror segments, based on the optical performance of the system. Furthermore, the deployment mechanisms of both the primary and secondary mirror were investigated.

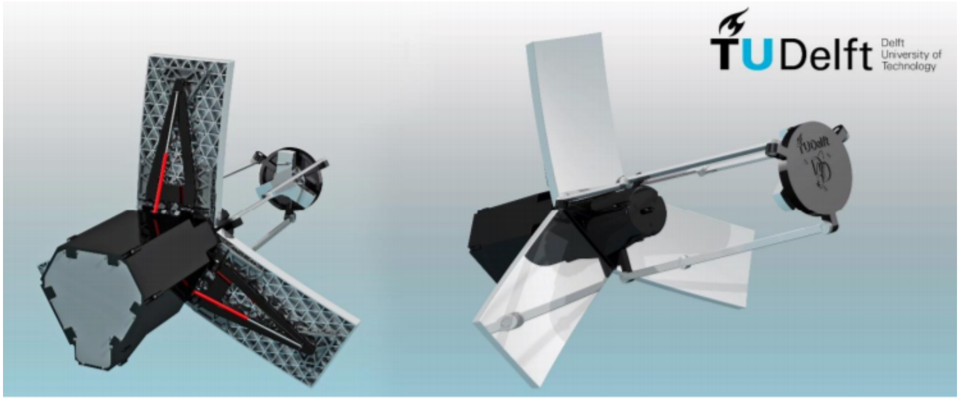

Figure 2.3: The first version of the DST as presented in the MSc. Thesis of D. Dolkens (2015)[16]

2.3.1. Optical Design

In the first conceptual design, Dolkens chose to use a full-field Korsch telescope design[16]. In a later design iteration however, it was chosen to go for an annular field Korsch telescope design. In the Korsch telescope design, there are three mirrors.

The primary mirror of the telescope is divided into four segments that have to be deployed when in space. The challenge in this design is to get the segments of the mirror properly aligned. Furthermore, also the secondary mirror has to be extended when in space, increasing the risk of aberrations due to alignment errors. A deformable mirror is included in the design. The design and modelling of this deformable mirror was performed by G.P. van Marrewijk.

2.3.2. Primary Mirror Design

B. T. van Putten's design iteration was finished in March 2017 [62]. This design will be shortly introduced in this section.

The main support structure was formed by a frame in the shape of an A. This A-frame was connected to the bus at two hinge points at the base of the A-frame, and a mid-hinged strut connecting the instrument bus and the centre of the A-frame. This A-frame was made out of Carbon Fibre Reinforced Polymers (CRFP) in Van Putten's design iteration. The interface with the mirror was formed by whiffle trees with two forms of flexures. Between the A-frame and the whiffles, actuated flexure were placed. These made it possible to adjust the mirror in three degrees of freedom. An image of the actuated flexure is given in Figure 2.4. In the centre, an eccentric nut on a shaft was used to move the middle flexure up and down. Due to the motion of the middle flexure, the top flexure was actuated. The layout of the flexure reduced the motion of the mid flexure, resulting in a lower amplitude of the top of the flexure than that of the mid flexure. The flexure was actuated by a stepper motor having 500 steps in combination with a harmonic drive having a reduction ratio of 50, resulting in 25000 steps per revolution [62].

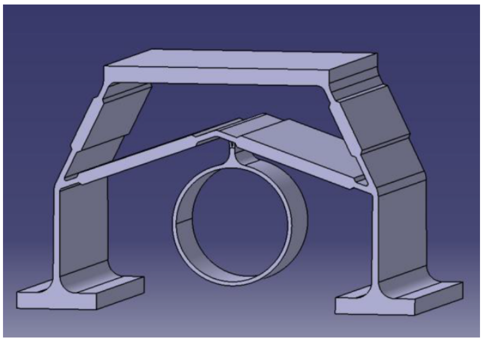

Figure 2.4: Actuated flexure design used to adjust the primary mirror segments in the DST. Image taken from [62]

Between the whiffle trees and the mirror, three small flexures were mounted per whiffle. These flexures would keep the mirror in its position, while allowing for thermal expansion with reference to the support structure. An overview of the different components of the support structure of a primary mirror segment is given in Figure 2.5.

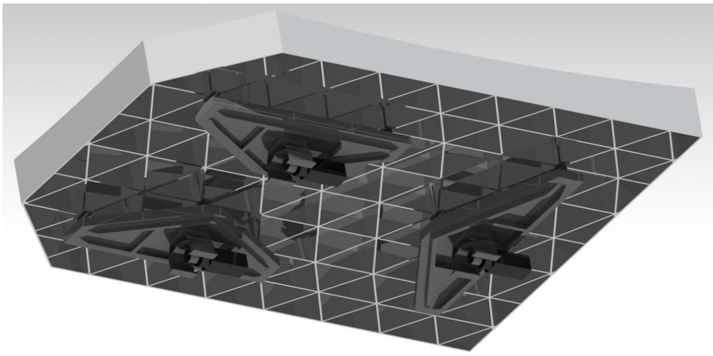

Figure 2.5: Overview of the support structure of a primary mirror segment. Image taken from [62]

The structure was supported by a mid-hinged rod. All three hinges had ball bearings to reduce hysteresis. Furthermore, the middle hinge was a self locking hinge. Although the middle hinge was the locking mechanism, the driving mechanism was located at the interface between the bus and the A-frame. It consists of a stepper motor with a simple spur gear assembly. The deployment of a primary mirror segment is given in Figure 2.6.

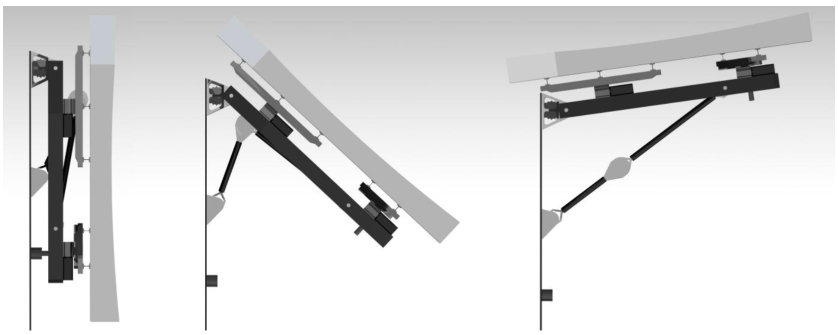

Figure 2.6: The deployment of a primary mirror segment of the DST. Image taken from [62].

2.3.3. Secondary Mirror Design

The design of the secondary mirror system is still in a conceptual phase. The first design iteration was performed by Dolkens [16]. The first concept was based on the deployment mechanism of the secondary mirror of the International X-ray Observatory (IXO), and was made out of invar. Due to the high density of invar, this concept was rather heavy. The mirror itself was made out of SiC, and cut in the shape of the aperture to save weight.

The first concept of Dolkens was deemed too heavy and lacked sufficient level of detail. The second iteration was performed by J. W. Lopes Barreto [42]. In his work, he made several trade-offs between deployment mechanisms. From the first trade-off, it became clear that the two deployment mechanisms best suited for this purpose were the articulated boom concept and the concept using shape memory composite (SMC). These two concepts were investigated in more detail. There are several types of SMC booms, and for his work, Lopes Barreto focussed on a Coilable Tubular Mast (CTM).

In the final trade-off, Lopes Barreto came to the conclusion that an articulated boom structure was the best option for the deployment of the secondary mirror of the DST. The articulated booms needed to be attached to the spacecraft bus and secondary mirror. It was chosen to attach the booms on the outside of the spacecraft bus. When installed on the outside, the booms will not interfere with the light path of the optical system. The attachment of the articulated booms to the bus is given in Figure 2.7.

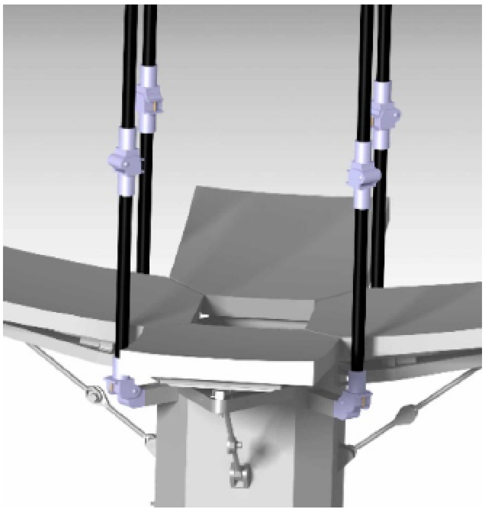

Figure 2.7: Attachment points on the outside of the spacecraft bus with the articulated booms of the secondary mirror support system. Image taken from [42].

The secondary mirror was connected to the booms with a structure referred to as the spider. The spider was made such, that the blockage of light was kept to a minimum. This was especially important at the interface between two mirror segments, since these areas will be used to calibrate the optical system. An image of the interface between booms and mirrors is given in Figure 2.8.

Figure 2.8: Render of the interface between the articulated booms and the secondary mirror of the DST. Image taken from [42].

2.4. Future Work

Up to this point, work was performed on the DST project by Dolkens, Van Putten, and Lopes Barreto. However, the spacecraft design is not ready yet and there is still work to be done. In this section, some of the work that still needs to be done is introduced.

2.4.1. Mission Budgets

Currently, there is not a clear overview of the budgets of the DST project. This is true for all the budgets of the project, like cost and schedule, but also the mass, power, and volume budgets and the optical alignment budgets need to be made and maintained throughout the project.

2.4.2. Primary Mirror Support Structure Design

As presented, the primary mirror support structure (PMSS) was already designed to a detailed level by Van Putten during his work for his MSc. Thesis. However, there is still work to be done. It became clear that the thermal effects on the support structure and mirrors are big, and effect the optical performance of the system in a negative way. It was further observed that the selected self-locking mid hinge does not work as expected. A redesign of this part is thus required. One of the conclusions of Van Putten was that a baffle was required to keep the thermal deformations within the satellite within budget. Furthermore, some more in depth mechanical analysis could be performed on vibrations, since currently a conservative approach was applied [62]. The driving mechanism of the structure is designed in a conceptual manner, and this deployment mechanism of the primary mirror segments needs to be investigated into more detail. The further development of the PMSS will be done by M. Corvers as part of his MSc. Thesis. The fine actuation of the primary mirror segments will be part of the MSc. Thesis of S. Pepper.

2.4.3. Secondary Mirror Support Structure Design

Currently, the design of the secondary mirror support structure (SMSS) is still in a conceptual phase. The deployment technique is currently selected to be an articulated boom system, and the first vibration and thermal analysis have been performed. The result of these preliminary investigations show that the current design does not meet every requirement yet. This means that detailed design of the boom system and the mirror support still have to be done, followed by a thorough mechanical and thermal analysis covering both the (pre-)launch and the operational phase.

The hinges of the booms are currently not designed in detail. Furthermore, the hinges selected currently do not allow the system to fold down in stowed configuration. A detailed design of the booms and the hinges is required.

The spider is currently a flat plate. The design was not made in detail. This has still to be done. Together with this, the interface between the mirror and the spider has to be designed. Currently no concept has been selected yet.

The above stated work will be the subject of this Thesis.

2.4.4. Baffle Design

In order to reduce stray light and isolate the mirrors and their structures from the external heat fluxes, it was proposed to use a baffle. There is currently no design for the baffle yet. In her MSc. Thesis, E. Korhonen will work on the design of the baffle.

2.4.5. Thermal Design

Currently, the thermal analyses were only performed on specific subsystems. However, a thermal analysis on the whole instrument has still to be done. This will be the responsibility of V. Villalba Corbacho together with S. Leegwater and T. van Wees.

2.5. Thesis Outline

This thesis will focus on the SMSS. The work of Lopes Barreto will be continued and the design presented in his thesis will form the baseline for further design. The most important conclusion from the thesis of Lopes Barreto was that the articulated boom concept was the best option for the SMSS. Since the hinges and the booms were not designed in detail, the starting point for the design will be the concept selection. This is also true for the spider design and the mirror interface. Furthermore, Lopes Barreto's design was based on a separation of 1.3 m between the primary and secondary mirror. From the optical subsystem, it was beneficial to increase this length to 1.6 m. This will require that the design for the booms have to be redone as well. It can thus be concluded that the design has to start at the top level system design, although the deployment concept is fixed to be an articulated boom system. This can be summarised in the research objective:

The research objective is to design the secondary mirror support structure of the Deployable Space Telescope project in detail, that can deploy the secondary mirror to the desired position within the deployment budgets, and keep it within the drift and stability budgets during the operational phase of the DST.

The main research question can be derived from this:

How can the secondary mirror support structure of the Deployable Space Telescope project be designed such that it fulfils the optical alignment budgets?

This thesis will try to find an answer on this research question.

3

SMSS Function & Requirements

In this chapter, the requirements of the SMSS will be introduced. First, the functions of the SMSS will be investigated, after which the requirements are formulated based on the SMSS functions and a requirement discovery tree (RDT).

3.1. SMSS Function

Before the requirements can be determined, first the function of the system has to be investigated. In this section, the function of the M2 support structure will be investigated with the help of a functional breakdown structure and a functional flow diagram.

3.1.1. Functional Breakdown Structure

To find all the functions the system has to fulfil, a functional breakdown structure (FBS) was made. This FBS covers all operational phases of the mission, from assembly and testing to End of Life (EOL). Each main function is split in several subfunctions. The FBS for the SMSS is given in Figure 3.1.

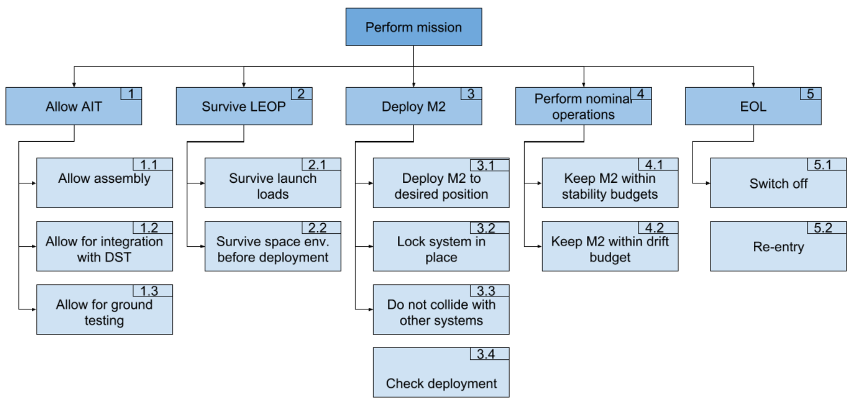

Figure 3.1: Functional Breakdown Structure of the M2 support structure.

3.1.2. Functional Flow Diagram

The FBS gives a good overview of the functions the system has to fulfil. However, the FBS does not give the relation between the functions. In order to provide a better overview of the order in which the functions have to be performed, a Functional Flow Diagram (FFD) was made. The top level FFD for the secondary mirror support system is given in Figure 3.2, while in Figure 3.3 a detailed FFD of the SMSS is given.

Figure 3.2: Top level Functional Flow Diagram for the SMSS.

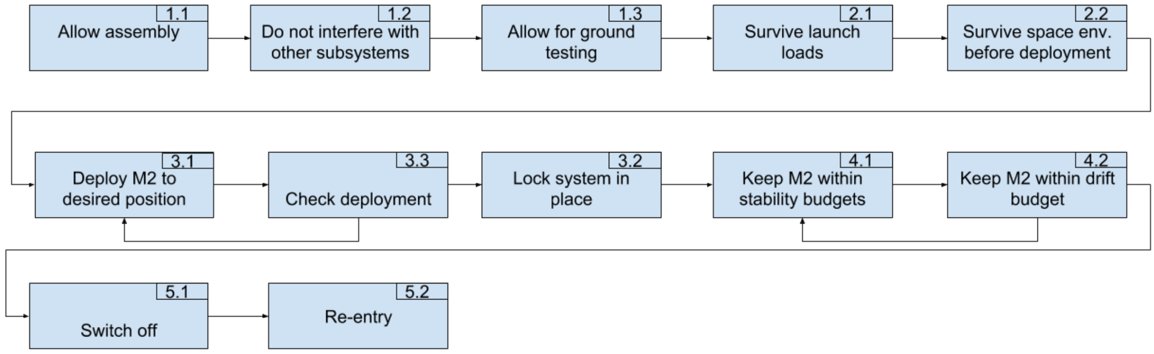

Figure 3.3: Detailed Funcitonal Flow Diagram for the SMSS

3.2. Requirements

In this section, the requirements for the SMSS will be presented. These requirements will not only be used during the design of the system, but also to determine if the final design of the system will satisfy the customer needs. The top level requirements are presented first, followed by a section on the subsystem requirements.

3.2.1. Top Level Requirements

The top level requirements are not subsystem specific but affect the entire telescope. The mission objective and mission requirements were made by other DST members, and are presented in Figure 3.7. The layout of the requirements was made by M. Corvers and S. Pepper. These mission requirements will be used to determine the subsystem requirements of the SMSS.

3.2.2. Subsystem Requirements

In this section, the subsystem requirements for the SMSS will be presented. Based on the mission objective and requirements, and the FBS and FFD given in Section 3.1, a Requirement Discovery Tree (RDT) was made for the SMSS. The RDT for the SMSS is given in Figure 3.4. Based on this RDT, some design aspects are investigated in more detail before the actual requirements were formulated. First, the alignment budgets and the volume constraints will be investigated, after which the subsystem requirements for the SMSS will be presented.

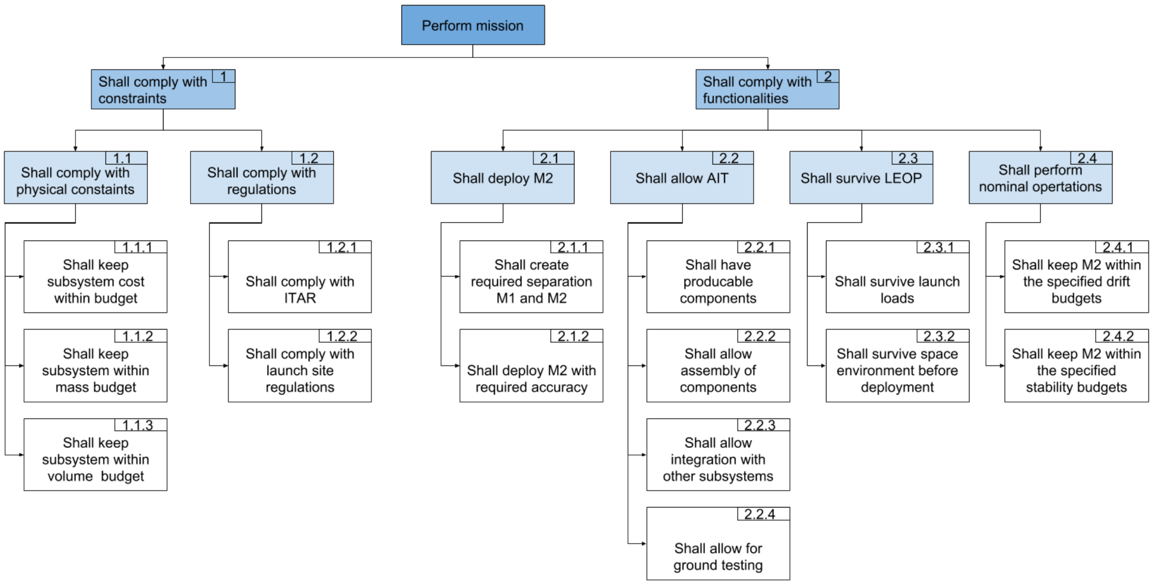

Figure 3.4: Requirement Discovery Tree for the SMSS of the DST.

Alignment Budgets

The alignment of the mirrors is of great importance for the optical performance of the system. In the different stages of the mission, different alignment budgets are important. There are 3 different alignment budgets important for the secondary mirror [17]:

- Deployment budget
- In-orbit drift budget
- Stability budget

As the name suggests, the deployment budget concerns with the alignment tolerances just after deployment. Alignment means in this context the actual position/orientation of the mirror with respect to the ideal position. The SMSS shall thus deploy the secondary mirror within these boundaries to the required position.

The second budget is the drift budget. Drift is determined as long term variations of the secondary mirror with respect to the nominal position. All vibrations with a frequency lower than around 1 Hz are considered as drift. A good example is the drift due to thermal variations of the spacecraft during a single orbit.

The last budget is the stability budget. This budget concerns the misalignment of the mirror due to vibrations with frequencies above 1 Hz, and are thus the short term disturbances. A good example for this budget is the disturbance due to reaction wheel vibrations.

An overview of the optical budgets is given in Figure 3.5.

Element	Position [µm]			Tilt [µrad]			Radius [%]	Shape Error [nm]
	X	Y	Z	X	Y	Z		
Coarse Alignment Tolerances								
M1	2	2	2	2	4	50	$1*10^{-3}$	50
M2	15	15	10	100	100	100	$1*10^{-2}$	25
M3	4	4	4	10	10	50	$1*10^{-3}$	10
In-Orbit Drifts								
M1	$2*10^{-2}$	$2*10^{-2}$	$2*10^{-2}$	$1*10^{-2}$	$2*10^{-2}$	5	$1*10^{-4}$	5
M2	4	4	2	6	6	12	$1*10^{-4}$	5
M3	$1*10^{-1}$	$1*10^{-1}$	$1*10^{-1}$	1	1	5	$1*10^{-4}$	5
Stability Budget								
M1	$5*10^{-3}$	$5*10^{-3}$	$5*10^{-3}$	$2.5*10^{-3}$	$1*10^{-2}$	$5*10^{-1}$	n/a	n/a
M2	1	1	$5*10^{-1}$	1.5	1.5	3	n/a	n/a
M3	$2.5*10^{-2}$	$2.5*10^{-2}$	$2.5*10^{-2}$	$2.5*10^{-1}$	$2.5*10^{-1}$	1.25	n/a	n/a

Figure 3.5: Alignment budgets for the three mirrors of the DST. Table taken from [17].

System Physical Constraints
Apart from optical performance, the system also has to fulfil requirements on mass and volume. The aim of the project is to produce an optical Earth observation space telescope with a fraction of the mass and volume of current state of the art Earth observation satellites. This limits the volume and mass budgets available for the SMSS.

The SMSS cannot be placed on the inside of the spacecraft bus. This is not because it is mechanically impossible, but it would interfere with the optical path. The border area between two primary mirror segments will be used for alignment of the system and thus may not be blocked by the secondary mirror support structure.

The current goal is to create a system that has a stowed volume of 0.75 m^3, with a threshold threshold of 1.5 m^3, see Requirement *MIS-REQ-09* in Figure 3.7. The design volume is currently based on the more detailed design of the primary mirror segments. In stored configuration, the secondary mirror support structure should not extend outside the envelope determined by the primary mirror segments in the X-Y plane. In deployed condition, the system may not interfere with the primary mirror segments. The dimensions of the primary mirror segments in stored and deployed condition can be seen in Figure 3.6. The projected area of the DST in stowed configuration is currently 0.767 X 0.767 m. This means that the height of the system in stowed configuration shall be equal to or lower than 1.27 m (goal) or 2.55 (threshold). Besides the limitations due to the primary mirror, the M2 may also not interfere with the field stop. The field stop extends 120 mm from the vertex of the primary mirror.

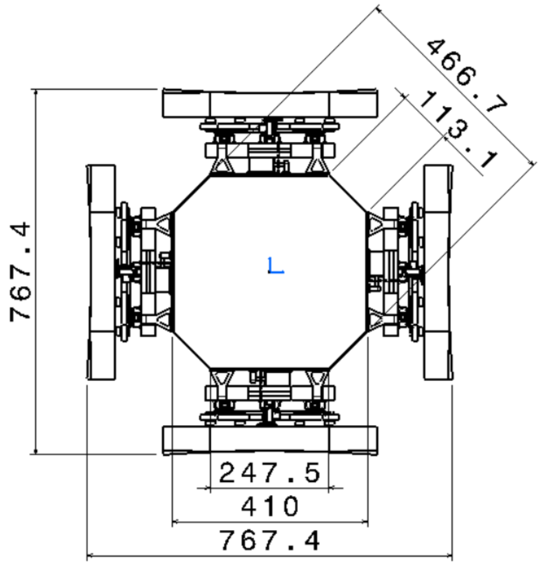

(a) Stored configuration

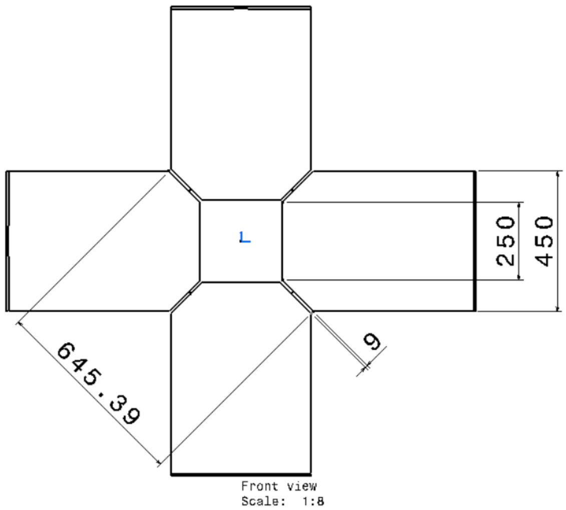

(b) Deployed configuration

Figure 3.6: Dimensions of the DST primary mirror segments in stored and deployed configuration.

Subsystem Requirements

With the top level requirements stated and the more detailed investigation given in the previous sections, the SMSS subsystem requirements were formulated. The requirements are given in Figure 3.8. The requirements that have an old identifier are taken from the thesis of J.W. Lopes Barreto [42]. The new identifiers are introduced to have a single consistent requirement identification system within the DST project. As stated, these requirements will be used to verify the system, which will be done in Chapter 12. There are four verification methods that can be used to verify the design:

- Inspection (I)
- Analysis (A)
- Demonstration (D)
- Test (T)

The verification methods used for the subsystem requirements are given in Figure 3.9.

Table 1 - Mission Objectives

Old ID	New ID	Description	Create	Last Upd	Parent	Comment	Responsible
N/A	MIS-OBJ-01	The Ground Sample Distance of the DST shall be no larger than the state of the art in commercial visual spectrum Earth Observation imaging platforms. As of 2017 this is DigitalGlobe's WorldView-4 satellite with a Ground Sample Distance of 0.31 m in the panchromatic	8-3-2018	8-3-2018	N/A	TBC	Kuiper
N/A	MIS-OBJ-02	The lifetime cost of the DST shall be less than the state of the art in commercial visual spectrum Earth Observation imaging platforms. As of 2017 this is DigitalGlobe's WorldView-4 satellite with an estimated cost of USD$850 million including ground network upgrades.	8-3-2018	8-3-2018	N/A	TBC	Kuiper

Table 2 - Mission/ Stakeholder Requirements

Old ID	New ID	Description	Create	Last Upd	Parent	Comment	Responsible
REQ-1	MIS-REQ-01	The Ground Sampling Distance of the instrument shall be equal to 25 cm in the panchromatic band from an orbital altitude of 500 km	1-2-2015	2-3-2018	MIS-OBJ-01	Dolkens, 2015 MSc thesis	Dolkens
REQ-2	MIS-REQ-02	The swath width of the instrument shall be wider than 1 km (threshold) / 5 km (goal)	1-2-2015	2-3-2018	MIS-OBJ-01	Dolkens, 2015 MSc thesis	Dolkens
REQ-3	MIS-REQ-03	The system shall have one panchromatic channel from 450 to 650 nm with a 25 cm GSD at an altitude of 500 km.	1-2-2015	9-3-2018	MIS-OBJ-01	Dolkens, 2015 MSc thesis.	Dolkens
REQ-3	MIS-REQ-04	The system shall have four multispectral bands with the wavelength ranges and GSD indicated (at 500 km): Blue (450 - 510 nm) - 100 cm Green (518 - 586 nm) - 100 cm Yellow (590 - 630 nm) - 100 cm Red (632 - 692 nm) - 100 cm	1-2-2015	9-3-2018	MIS-OBJ-01	Dolkens, 2015 MSc thesis.	Dolkens
REQ-4	MIS-REQ-05	The Signal-to-Noise Ratio (SNR) of the instrument shall be higher than 100 for a reflectance of 0.30 and a sun Zenith angle of 60°	1-2-2015	2-3-2018	MIS-OBJ-01	Dolkens, 2015 MSc thesis	Dolkens
REQ-5	MIS-REQ-06	The nominal Modulation Transfer Function (MTF) at both the Nyquist frequency and half the Nyquist frequency shall be higher than 5%	1-2-2015	2-3-2018	MIS-OBJ-01	Dolkens, 2015 MSc thesis	Dolkens
REQ-6	MIS-REQ-07	After calibration, the residual Strehl ratio of the system shall be higher than 0.80.	1-2-2015	2-3-2018	MIS-OBJ-01	Dolkens, 2015 MSc thesis	Dolkens
REQ-7	MIS-REQ-08	The mass of the instrument shall be lower than 100 kg (threshold) / 50 kg (goal).	1-2-2015	2-3-2018	MIS-OBJ-02	Dolkens, 2015 MSc thesis	Dolkens
REQ-8	MIS-REQ-09	In the stowed configuration, the volume of the instrument shall not exceed 1.5 m3 (threshold) / 0.75 m3 (goal)	1-2-2015	2-3-2018	MIS-OBJ-02	Dolkens, 2015 MSc thesis	Dolkens
N/A	MIS-REQ-10	The DST shall not use any ITAR controlled components or technology.	8-3-2018	8-3-2018	MIS-OBJ-02	TBC	Kuiper
N/A	MIS-REQ-11	The DST shall be designed for compatibility with the TBD launcher.	8-3-2018	8-3-2018	MIS-OBJ-02	TBC	Villalba Corbacho
N/A	MIS-REQ-12	The DST shall comply with national (NL) and international regulations during AIT activities, launch, operations and end of life.	14-3-2018	14-3-2018	MIS-OBJ-01	Must not violate laws.	Kuiper

Figure 3.7: Mission objectives and requirements

Table 4 - M2

Old ID	New ID	Description	Create	Last Upd	Parent	Comment	Responsi
		System					
R-M2D-GEN-3	M2-SYS-01	The total mass of the M2 mechanism shall be lower than 14 kg	19-5-2017	2-3-2018	MIS-REQ-08	Lopes Barreto, 2017 MSC	Krikken
R-M2D-GEN-2	M2-SYS-02	The mechanism shall provide structural support for M2	19-5-2017	2-3-2018		Lopes Barreto, 2017 MSC	Krikken
N/A	M2-SYS-03	The M2 mechanism in stowed configuration shall stay within the boundary box given by the primary mirror segments.		16-6-2018	MIS-REQ-09		Krikken
N/A	M2-SYS-04	The M2 mechanism in stowed configuration height, including the instrument bus, shall be equall or less than 1.27m (goal)/2.55m (threshold)		16-6-2018	MIS-REQ-09		Krikken
N/A	M2-SYS-05	The development, production, assembly, integration, and test cost of the M2 mechanism shall be equal to or lower than TBD			MIS-OBJ-02	Cost budget not available yet	Krikken
		Functionality requirements					
~~R-M2D-GEN-1~~		~~The mechanism shall extend M2 1.3m fromM1~~	~~19-5-2017~~	~~2-3-2018~~		~~Lopes Barreto, 2017 MSC~~	~~Krikken~~
N/A	M2-MEC-01	The M2 mechanism shall deploy the M2 along the optical axis (Z axis) to obtain a distance of 1.6 m between M1 and M2, measured between the vertex of both mirrors			MIS-REQ-07		Krikken
~~R-M2D-STR-1~~		~~The deployed mechanism shall have a maximum deflection of 15 µm in the x- and y- direction, measured from the root~~	~~19-5-2017~~	~~2-3-2018~~		~~Lopes Barreto, 2017 MSC~~	~~Krikken~~
~~R-M2D-STR-2~~		~~The deployed mechanism shall have a maximum deflection of 10 µm in the z-direction, measured from the root~~	~~19-5-2017~~	~~2-3-2018~~		~~Lopes Barreto, 2017 MSC~~	~~Krikken~~
~~R-M2D-STR-3~~		~~The deployed mechanism shall have a maximum twist of 100 µrad about all axes, measured from the root~~	~~19-5-2017~~	~~2-3-2018~~		~~Lopes Barreto, 2017 MSC~~	~~Krikken~~
N/A	M2-MEC-02	The M2 mechanism deployment accuracy shall be equal to or less than 15µm measured along the X axis of the telescope coordinate frame		16-6-2018	MIS-REQ-07	deployment budget	Krikken
N/A	M2-MEC-03	The M2 mechanism deployment accuracy shall be equal to or less than 15µm measured along the Y axis of the telescope coordinate frame		16-6-2018	MIS-REQ-07	deployment budget	Krikken
N/A	M2-MEC-04	The M2 mechanism deployment accuracy shall be equal to or less than 10µm measured along the optical axis (Z axis) of the telescope		16-6-2018	MIS-REQ-07	deployment budget	Krikken
N/A	M2-MEC-05	The M2 mechanism deployment accuracy shall be equal to or less than 100µrad measured around the X axis of the telescope coordinate		16-6-2018	MIS-REQ-07	deployment budget	Krikken
N/A	M2-MEC-06	The M2 mechanism deployment accuracy shall be equal to or less than 100µrad measured around the Y axis of the telescope coordinate frame of the telescope coordinate frame		16-6-2018	MIS-REQ-07	deployment budget	Krikken
N/A	M2-MEC-07	The M2 mechanism deployment accuracy shall be equal to or less than 100µrad measured around the optical axis (Z axis of the telescope		16-6-2018	MIS-REQ-07	deployment budget	Krikken
N/A	M2-MEC-08	The radius of curvature of the M2 mirror shall change less than 0.01% due to the deployment of the mechanism		16-6-2018	MIS-REQ-07	deployment budget	Krikken
N/A	M2-MEC-09	The shape error of the M2 shall be less than 25 nm due to the deployment of the mechanism		16-6-2018	MIS-REQ-07	deployment budget	Krikken
N/A	M2-MEC-10	The M2 mechanism in-orbit drift shall be equal or less than 4 µm measured along the X axis of the telescope coordinate frame		16-6-2018	MIS-REQ-07	Drift budget	Krikken
N/A	M2-MEC-11	The M2 mechanism in-orbit drift shall be equal or less than 4 µm measured along the Y axis of the telescope coordinate frame		16-6-2018	MIS-REQ-07	Drift budget	Krikken
N/A	M2-MEC-12	The M2 mechanism in-orbit drift shall be equal or less than 2 µm measured along the optical axis (Z axis of the telescope coordinate frame)		16-6-2018	MIS-REQ-07	Drift budget	Krikken
N/A	M2-MEC-13	The M2 mechanism in-orbit drift shall be equal or less than 6 µrad measured around the X axis of the telescope coordinate frame		16-6-2018	MIS-REQ-07	Drift budget	Krikken
N/A	M2-MEC-14	The M2 mechanism in-orbit drift shall be equal or less than 6 µrad measured around the Y axis of the telescope coordinate frame		16-6-2018	MIS-REQ-07	Drift budget	Krikken
N/A	M2-MEC-15	The M2 mechanism in-orbit drift shall be equal or less than 12 µrad measured around the Z axis of the telescope coordinate frame		16-6-2018	MIS-REQ-07	Drift budget	Krikken
N/A	M2-MEC-16	The radius of curvature of the M2 mirror shall change less than 0.0001% due to in-orbit drift		16-6-2018	MIS-REQ-07	Drift budget	Krikken
N/A	M2-MEC-17	The shape error of the M2 shall be less than 5 nm due to in-orbit drifts		16-6-2018	MIS-REQ-07	Drift budget	Krikken
N/A	M2-MEC-18	The M2 mechanism stability shall be equal to or less than 1 µm along the X axis of the telescope reference frame		16-6-2018	MIS-REQ-07	Stability budget	Krikken
N/A	M2-MEC-19	The M2 mechanism stability shall be equal to or less than 1 µm along the Y axis of the telescope reference frame		16-6-2018	MIS-REQ-07	Stability budget	Krikken
N/A	M2-MEC-20	The M2 mechanism stability shall be equal to or less than 0.5 µm along the Z axis of the telescope reference frame		16-6-2018	MIS-REQ-07	Stability budget	Krikken
N/A	M2-MEC-21	The M2 mechanism stability shall be equal to or less than 1.5 µrad around the X axis of the telescope reference frame		16-6-2018	MIS-REQ-07	Stability budget	Krikken
N/A	M2-MEC-22	The M2 mechanism stability shall be equal to or less than 1.5 µrad around the Y axis of the telescope reference frame		16-6-2018	MIS-REQ-07	Stability budget	Krikken
N/A	M2-MEC-23	The M2 mechanism stability shall be equal to or less than 3 µrad around the Z axis of the telescope reference frame		16-6-2018	MIS-REQ-07	Stability budget	Krikken
R-M2D-STR-4	M2-MEC-24	The deployed mechanismshall have a minimumnatural frequency of 5 Hz	19-5-2017	16-6-2018		Lopes Barreto, 2017 MSC	Krikken
		Launch					
~~R-M2D-LAU-1~~		~~The stowed mechanism shall be able to withstand accelerations up to 30 g~~	~~19-5-2017~~	~~2-3-2018~~		~~Lopes Barreto, 2017 MSC~~	~~Krikken~~
N/A	M2-MEC-25	The M2 mechanism shall be able to survive launch in the stowed configuration. Survival is defined as no impairment to the nominal functional capabilities of the system resulting from exposure to a given set of environmental conditions.		16-6-2018		Based on ADS advice	Krikken
N/A	M2-MEC-25-01	The M2 mechanism shall be able to survive a quasi static acceleration of 30 G simultaniously applied in the X and Y direction in the telescope coordinate frame		16-6-2018	M2-MEC-25	Based on ADS advice	Krikken
N/A	M2-MEC-25-02	The M2 mechanism shall be able to survive a quasi static acceleration of 30 G simultaniously applied in the Y and Z direction in the telescope coordinate frame		16-6-2018	M2-MEC-25	Based on ADS advice	Krikken
N/A	M2-MEC-25-03	The M2 mechanism shall be able to survive a quasi static acceleration of 30 G simultaniously applied in the X and Z direction in the telescope coordinate frame		16-6-2018	M2-MEC-25	Based on ADS advice	Krikken
R-M2D-LAU-2	M2-MEC-25-04	The stowed mechanism shall have a minimum natural frequency of 100 Hz	19-5-2017	2-3-2018	M2-MEC-25	Lopes Barreto, 2017 MSC	Krikken
		Program					
R-M2D-GEN-5	M2-SYS-06	The M2 mechanism shall not contain ITAR related components	19-5-2017	2-3-2018	MIS-REQ-10	Lopes Barreto, 2017 MSC	Krikken
R-M2D-GEN-6	M2-SYS-07	The mechanism shall comply with the Guiana Space Centre safety regulations	19-5-2017	2-3-2018	MIS-REQ-12	Lopes Barreto, 2017 MSC	Krikken
		Subsystem interfaces					
~~R-M2D-GEN-4~~		~~The mechanism shall have a minimumdeployment ratio of 2~~	~~19-5-2017~~	~~2-3-2018~~		~~Lopes Barreto, 2017 MSC~~	~~Krikken~~
N/A	M2-MEC-26	The M2 system shall not come in contact or interfere with other subsystems during any mission phase		16-6-2018			Krikken
N/A	M2-MEC-26-01	The M2 mechanism in stowed configuration shall not interfere with the interface between the launcher and the spacecraft		16-6-2018	M2-MEC-26		Krikken
N/A	M2-MEC-26-02	The M2 mechanism, with the exception of the spider, shall not block the light path of the M1 or M2 mirrors		16-6-2018	M2-MEC-26		Krikken
N/A	M2-MEC-26-03	The width of the spider of the M2 mechanism shall be 15 mm or less, covering no more than 3 mm of mirror of each segment		16-6-2018	M2-MEC-26		Krikken
N/A	M2-MEC-26-04	The M2 mechanism shall be connected to the outside of the instrument bus		16-6-2018	M2-MEC-26		Krikken
N/A	M2-MEC-26-05	The parts of the M2 mechanism covering part of the light path of the mirrors shall have a regular, predictable shape that minimises scattering		16-6-2018	M2-MEC-26		Krikken
N/A	M2-MEC-26-06	The M2 system shall not interfere with the field stop, extending 120 mm form the M1 vertex		16-6-2018	M2-MEC-26	Based on forta	Krikken
		AIT requirements					
N/A	M2-MEC-27	The components of the SMSS shall be producable without the need to develop new production tools			MIS-OBJ-02		Krikken
N/A	M2-MEC-28	The components shall be able to be assembled without interfering with other systems			MIS-MEC-26		Krikken
N/A	M2-MEC-29	The system shall be able to be tested on ground multiple times without the need to change permantly locked components				Allow ground calibration	Krikken

Figure 3.8: Mission objectives and requirements

Old ID	New ID	Verification method
System		
R-M2D-GEN-3	M2-SYS-01	I
R-M2D-GEN-2	M2-SYS-02	I
N/A	M2-SYS-03	I
N/A	M2-SYS-04	I
N/A	M2-SYS-05	I
Functionality		
~~R-M2D-GEN-1~~		
N/A	M2-MEC-01	I
~~R-M2D-STR-1~~		
~~R-M2D-STR-2~~		
~~R-M2D-STR-3~~		
N/A	M2-MEC-02	A/T
N/A	M2-MEC-03	A/T
N/A	M2-MEC-04	A/T
N/A	M2-MEC-05	A/T
N/A	M2-MEC-06	A/T
N/A	M2-MEC-07	A/T
N/A	M2-MEC-08	A/T
N/A	M2-MEC-09	A/T
N/A	M2-MEC-10	A/T
N/A	M2-MEC-11	A/T
N/A	M2-MEC-12	A/T
N/A	M2-MEC-13	A/T
N/A	M2-MEC-14	A/T
N/A	M2-MEC-15	A/T
N/A	M2-MEC-16	A/T
N/A	M2-MEC-17	A/T
N/A	M2-MEC-18	A/T
N/A	M2-MEC-19	A/T
N/A	M2-MEC-20	A/T
N/A	M2-MEC-21	A/T
N/A	M2-MEC-22	A/T
N/A	M2-MEC-23	A/T
R-M2D-STR-4	M2-MEC-24	A/T
Launch		
~~R-M2D-LAU-1~~		
N/A	M2-MEC-25	A/T
N/A	M2-MEC-25-01	A/T
N/A	M2-MEC-25-02	A/T
N/A	M2-MEC-25-03	A/T
R-M2D-LAU-2	M2-MEC-25-04	A/T
Program		
R-M2D-GEN-5	M2-SYS-06	I
R-M2D-GEN-6	M2-SYS-07	I
Interfaces		
~~R-M2D-GEN-4~~		
N/A	M2-MEC-26	I/T
N/A	M2-MEC-26-01	I/T
N/A	M2-MEC-26-02	I/T
N/A	M2-MEC-26-03	I
N/A	M2-MEC-26-04	I
N/A	M2-MEC-26-05	I/A/T
N/A	M2-MEC-26-06	I
AIT		
N/A	M2-MEC-27	I/D
N/A	M2-MEC-28	I/D
N/A	M2-MEC-29	I/D

Figure 3.9: Verification methods used for the verification of the requirements

4 Design Loads during LEOP & Standards

The SMSS will be subjected to different loads during the different mission phases. The load cases presented in this chapter are used in the design process to ensure that the system can survive all mission phases. In the design process the failure criterion is used to determine when the component fails. Since this, together with the safety factors, are common for all components, they will be presented in this chapter together with the design load cases. In the first section, the mechanical loads experienced during launch are discussed, followed by a section on the thermal loads during the Launch and Early Operations (LEOP) phase. In the last section, the failure criterion used in this thesis is discussed.

4.1. Launch Loads

The launch loads used in this thesis are the standard cases used within the DST project. A launch load of +30 G in the (x + y), (y + z), and (x + z) directions is applied, resulting in three load cases. This 30G semi static load is an estimate of the combination of the semi static and dynamic loads experienced during launch. This load was based on advice from Airbus Defence and Space Netherlands as used in the thesis of Van Putten [62]. As this is currently used as the DST standard, other subsystems will use this condition as well. The standards used are given in the *DST Requirements Document*, which is an internal document.

4.2. LEOP Thermal Environment

During LEOP, the SMSS will be subjected to the largest thermal variations. In this section, the thermal environment during LEOP is discussed. But first, the thermal margins are discussed.

Within the DST project standard thermal margins are used. The temperature range is calculated using a simulation. On the obtained thermal range, margins are applied. Five temperature ranges are identified: the calculated temperature range, the predicted temperature range, the design temperature range, the acceptance temperature range, and the qualification temperature range.

The **calculated temperature range** is the temperature range resulting from the thermal simulations. An uncertainty margin is applied on this range to cover the model uncertainties. This obtained temperature range is called the **predicted temperature range.** For the DST project an uncertainty margin of 15 K is used. This number was based on [53], clause A1. In the DST project, the **design temperature range** is equal to the predicted temperature range. The design temperature range is the design input for the thermal subsystem. An acceptance margin of 5 K is added to this range to account for unpredicted behaviour of the thermal control system. The temperature range obtained is called the **acceptance temperature range**. An additional 5 K is added to this range to account for unexpected events. This temperature range is the **qualification temperature range**. The temperature ranges are summarised in Figure 4.1, while Figure 4.2 gives the margins used in the DST project. The temperature ranges were investigated and determined by S. Pepper, not by the author. They are presented here to give a full overview of the thermal requirements.

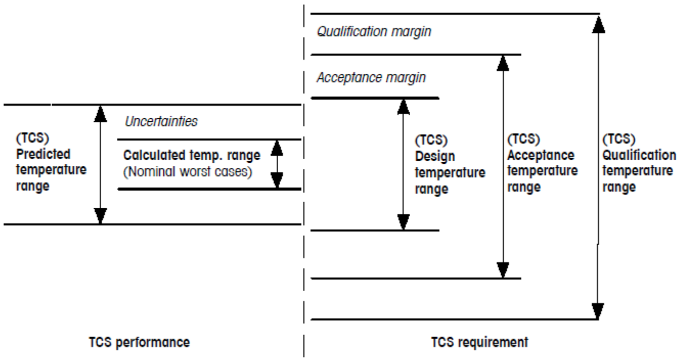

Figure 4.1: Temperature ranges used in the DST project. Image taken from [53]

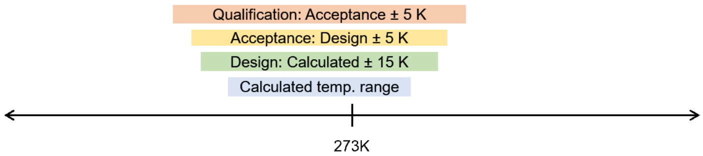

Figure 4.2: Temperature ranges used in the DST project. Image was made by S. Pepper

The thermal design of the DST is still in an early phase. To get an idea of the extreme temperatures encountered by the DST, the author and S. Pepper worked on a preliminary thermal model of the DST in stowed configuration in LEOP. The thermal network was the task of S. Pepper, while the author was responsible for the heat fluxes on the spacecraft. In this section, only the calculation of the heat fluxes are given. For more information on the thermal network, refer to the *DST-WP1-CALC-001* document.

The spacecraft is modelled as a square box, where the bottom of the box is perfectly thermally insulated. The thermal properties of the sides are given in Table 4.1. The normal of the top surface points in the velocity direction, while one of the sides of the box always points nadir.

Side	α	ϵ
Instrument sides (Polished silver, M1 segments)	0.04	0.02
Instrument top (CFRP, spider)	0.93	0.85

Table 4.1: Thermal properties used in the priliminary thermal model of the instrument during LEOP.

The orbit chosen is a 500 km Sun Synchronous Orbit (SSO), with a right ascension of the ascending node (RAAN) of 22:30 local ground time. The angles between the sun and the surface normals are calculated in the spacecraft centred celestial sphere, with the x-axis pointing nadir, the y-axis pointing towards the orbit pole. For each moment in time, the angle between each surface and the vector towards the sun is calculated. This angle is called β and is calculated with [40]:

$$cos(\beta) = cos(\gamma)cos(\beta_S') + sin(\gamma)sin(\beta_S')cos(\Delta A_z) \tag{4.1}$$

In this equation, β_S' is the angle between the sun and the orbit pole, γ is the angle between the surface normal and the orbit pole, and ΔA_z is the difference between the azimuth of the sun and the normal of the surface, see Figure 4.3a.

The eclipse the spacecraft will experience is calculated using the following equation [40]:

$$A_{z,eclipse} = A_{z,0} \pm cos^{-1}\left(\frac{cos(\rho)}{sin(\beta_S')}\right) \tag{4.2}$$

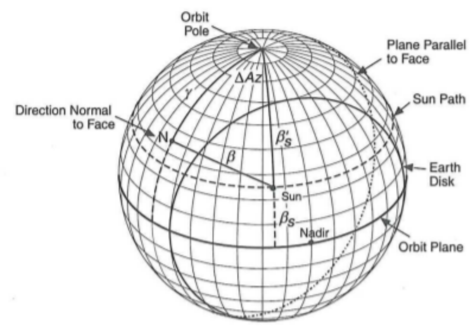

(a) Solar angles

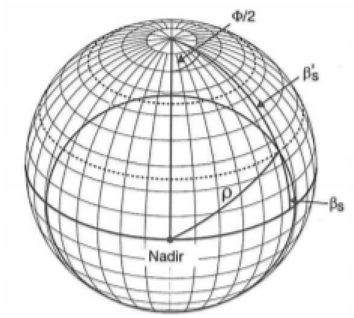

(b) Eclipse angle

Figure 4.3: Angles used in the solar angle calculations for the preliminary thermal model. Images taken from [40]

Where $A_{z,eclipse}$ is the azimuth range the spacecraft is in eclipse. $A_{z,0}$ is the azimuth angle of the centre of eclipse, which is 0 in this case. For the angles, see Figure 4.3b. The result can be seen in Figure 4.4. The solar input was calculated using these beta angles. This was added to the Earth IR and albedo heat inputs. The temperature was calculated for the worst hot and cold cases. This resulted in a temperature range of 180 to 411 K. Adding the 25 K margin, this resulted in a temperature range of 155 - 436 K.

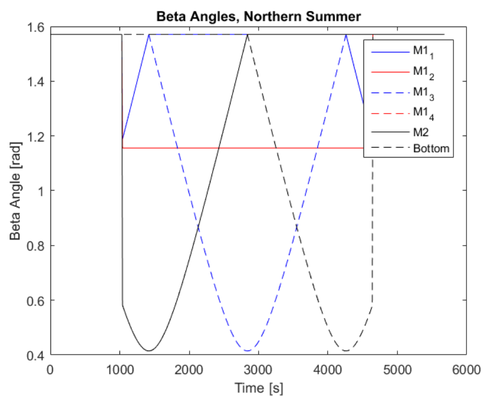

(a) Summer

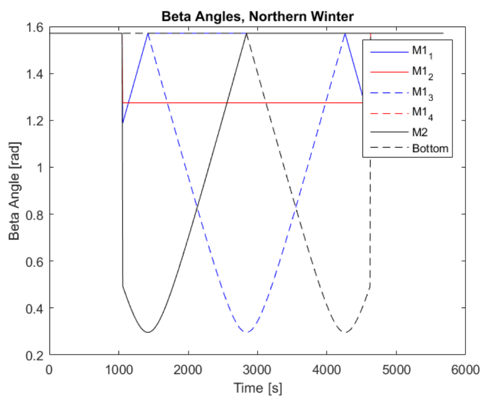

(b) Winter

Figure 4.4: Beta angles of the spacecraft as calculated for the Northern hemisphere summer and winter.

4.3. Failure Criterion & Safety Factors

The failure criterion used in this thesis is the Distortion-energy hypothesis, sometimes called the shear-energy hypothesis, the von Mises-Hencky hypothesis, or the octahedral-shear-stress hypothesis [54]. This criterion was preferred over the other theories like the maximum shear stress theory, and after discussion with the team the von Mises-Hencky theory was set as the standard within the DST project and added to the *DST Requirements Document*. This theory states that the material starts to yield when the effective stress, or von Mises stress σ', exceeds the yield stress of the material [54]:

$$\sigma' \geq \sigma_{yield} \tag{4.3}$$

It must be stated that not all materials yield. In these cases the ultimate stress is used. The von Mises stress within the material can be calculated when the principle stress within the material is known [54]:

$$\sigma' = \sqrt{\frac{(\sigma_1 - \sigma_2)^2 + (\sigma_2 - \sigma_3)^2 + (\sigma_3 - \sigma_1)^2}{2}} \tag{4.4}$$

The von Mises stress can also be expressed as function of the stress state in a given reference frame instead of the principal stress [54]:

$$\sigma' = \sqrt{\frac{\left(\sigma_x - \sigma_y\right)^2 + \left(\sigma_y - \sigma_z\right)^2 + \left(\sigma_z - \sigma_x\right)^2 + 6\left(\tau_{xy}^2 + \tau_{yz}^2 + \tau_{zx}^2\right)}{2}} \tag{4.5}$$

The safety factors are introduced to cover uncertainties within the load cases. The safety factors have to be applied on the loads, not on the stress. This is because some load cases do not have a linear relation with the resulting stress. A good example of this is the buckling of a structure. Since the strength of the component is expressed in the applied load, a safety factor on the stress would give a wrong representation of the strength of the component, and possible overloading can take place. The used safety factors are listed below in Table 4.2. The table is based on the work of S. Pepper, who reported his findings in the DST requirements document from which the table is taken.

Table 4.2: Safety factors used within the DST project. The safety factors were investigated and reported by S. Pepper. The table is based on the work done by S. Pepper, who based the table on [40].

Description	$\mathrm{SF}_{\mathrm{yield}}$	$\mathrm{SF}_{\mathrm{ult}}$
Static	1.25	1.4
Sine	1.25	1.4
Random/Accoustic	1.6	1.8

II

Secondary Mirror Support Structure Design

5

M2 System Level Design

In the previous chapters the current state of the design of the SMSS was discussed. In these chapters it was concluded that the current design of the SMSS has some points of improvement. This chapter will discuss the top level design of the SMSS based on the recommendations on the previous design. In the first section, the number of booms will be discussed, followed by a section covering the degrees of freedom (DOF) of the links used in the booms. The tolerances on these links are discussed in the next section, followed by a section about the stowed configuration of the system.

In the requirements stated in Chapter 3. These requirements can be translated in a wish list for the SMSS:

- Deploy the M2 1.6 m above the primary mirror segments, measured between the vertex of both mirrors
- Stay within the given volume budget
- Have a low mass
- Do not interfere with the telescope optics
- Have a low thermal sensitivity
- Form an exactly constrained design for high deployment repeatability
- Provide a stiff support for M2 for a high stability.

With this wish list in mind, the top level system design was started.

5.1. Number of Booms and Orientation

The first design of the SMSS made by Dolkens had three booms connecting the M2 and the bus. In the design made by Lopes Barreto the SMSS has four booms that support the spider. The reason to increase the number of booms to four was that the number of M1 segments was increased to four. This meant that a symmetrical design with three booms was impossible without blocking the light of the M1 segments.

The advantage of four booms is that the system is again symmetrical, giving symmetrical eigenmodes. Apart from that, an extra boom could result in an increase in stiffness of the system. The downside is that the system becomes overconstrained. When there are errors in deployment or production, one or multiple components have to deform in order to come to a deployed condition. This introduces unpredictability in the system.

Another option is to use three booms, and designing the links such that the system is exactly constrained. The repeatability of an exact constrained design is high. If there are production or assembly errors present in the system, the accuracy of the system is reduced, but the system remains repeatable. Production and assembly errors can then be compensated on ground. The removal of one of the booms could lead to a reduction in stiffness and will make the system asymmetrical.

The positive and negative aspects discussed above are given in Table 5.1. In order to compare the two options, a small trade-off table was made. This is given in Table 5.2.

Table 5.1: Strong and weak points of the SMSS with three and four booms.

Concept	**Positive aspects**	**Negative aspects**
Four booms	• Possibly higher stiffness • Symmetric design	• Overconstrained design, unpredictable deformations • Higher mass
Three booms	• Can be made exactly constrained • Lower mass	• Asymmetric design • Possibly lower stiffness

Table 5.2: Trade-off table for the number of booms of the SMSS

Option	Stiffness	Deformations	Mass
Four booms	Green Higher stiffness due to extra boom	Yellow Overconstrained, unpredictable deformations	Blue Higher mass
Three booms	Blue Possibly lower	Green Predictable deployment behaviour	Green Lower mass

Green	Excellent
Yellow	Sufficient
Blue	Good
Red	Unacceptable

From the arguments mentioned in Table 5.1 and Table 5.2, it can be seen that it could be beneficial to decrease the amount of booms from four to three. It must be stated that the trade-off was performed in an early stage of the project, at which not much information is known. When more information about the system comes available during the design, the results of this trade-off may change. It is thus important to re-evaluate this trade-off during the design process.

In the design iteration of Lopes Barreto, the booms were parallel to each other in deployed condition. With the type of hinges used in the design, this led to a problem in stowed condition. A solution to this is to increase the length of the spider, which results in non-parallel booms. A schematic representation of the difference between the parallel booms and the booms under an angle is given in Figure 5.1. This concept of non-parallel booms is interesting, since it could be possible that by changing the orientation of the booms the stiffness of the system is increased. This hypothesis is based on the fact that a rectangular shaped system with parallel booms has a lower stiffness than a pyramid shaped system with non-parallel booms. The current design iteration was then equipped with non-parallel booms to test this hypothesis. The booms are standing outwards, since they are not allowed to cross the primary mirror segments. As stated before, this decision has to be re-evaluated when more information is available.

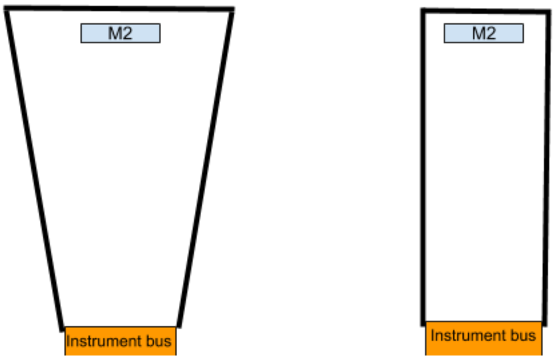

Figure 5.1: Schematic representation of the system with parallel booms (r) and booms under an angle (l).

5.2. SMSS Constraint Analysis

By locking the hinge between the boom segments with high accuracy, the segments will form single, straight boom which reduces the degrees of freedom of the system. To exactly constrain the system, additional hinges have to be locked. Care must be taken not to overconstrain the system. In this section, this is investigated.

5.2.1. Mount Concept

During the literature study, different forms of mounts for optical systems were investigated. From this study, it became clear that a mount using the kinematic mount principle is the best candidate for this problem. There are two main forms of kinematic mounts: the Kelvin kinematic coupling and the Maxwell kinematic coupling, see Figure 5.2.

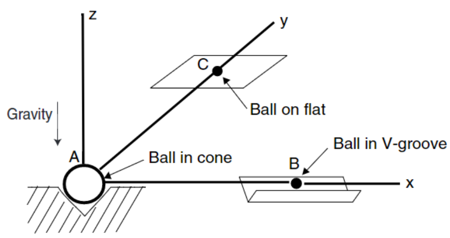

(a) Kelvin kinematic mount [4]

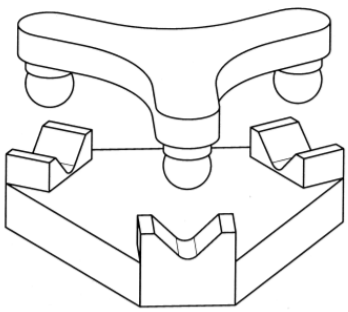

(b) Maxwell kinematic coupling [27]

Figure 5.2: Two forms of kinematic mounts. In a) the principle of the Kelvin kinematic coupling and in b) the principle of the Maxwell kinematic coupling. Images taken from [4, 27]

The layout of the system is suitable for a Kelvin kinematic coupling. This means that one boom has to act as the ball-in-cone interface, and thus restrict translation in the x, y, and z direction. Another beam has to act as the ball-in-V-groove interface, and has to restrict translation in the y, and z direction. The third boom has to act as the ball-on-plane interface, and thus only restrict translation in the z direction. Together, the booms will restrict all DOFs. This means however that the hinges must allow translation and rotation in multiple directions. To check if this concept works, a constraint analysis was performed.

5.2.2. Constraint Analysis

The constraint analysis was done using a mathematical approach. The constraints acting on the spider are given in Figure 5.3.

The spider is supported by three booms. Each boom has a hinged connection to the spider, and to the instrument bus. This means that each boom is a serial system, and these serial systems are

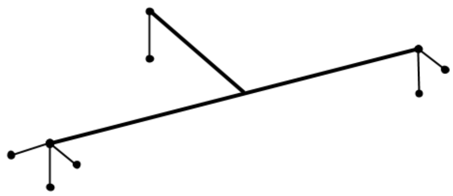

Figure 5.3: Constraints acting on the spider in the Kelvin mount configuration.

connected in parallel to the spider. Both the DOF (twist) and the constraints (wrench) form screws. Twists and wrenches are vectors with the size 6x1 (in 3D space) [32]:

$$T = \begin{bmatrix} Rotation \\ Translation \end{bmatrix} = \begin{bmatrix} \omega \\ r \times \omega + h\omega \end{bmatrix} \tag{5.1}$$

$$W = \begin{bmatrix} Force \\ Moment \end{bmatrix} = \begin{bmatrix} f \\ r \times f + hf \end{bmatrix} \tag{5.2}$$

Where ω is the rotation vector which is a unit vector, r is the position of the constraint/DOF with reference to the used axis system measured in meters, f is the force vector which is also a unit vector, and h is the pitch of the screw. For a pure rotational DOF (a revolute joint for example) the pitch is zero. For a translation DOF (a prismatic joint), the pitch is infinite. In the current problem, only revolute joints are present, and thus the pitch of the twists and wrenches are all zero. When a set of twists or wrenches is given, the reciprocal system can be found by the following rule [32]:

$$W^{\perp} = ker\left(T^T\Gamma\right) \tag{5.3}$$

$$T^{\perp} = ker\left(W^T\Gamma\right) \tag{5.4}$$

Where ker is the kernel, and $Gamma$ is the reciprocity matrix:

$$\Gamma = \begin{bmatrix} 0 & \mathrm{I} \\ \mathrm{I} & 0 \end{bmatrix} \tag{5.5}$$

In Equation 5.5, ***0*** is the 3x3 null matrix, and ***I*** is the 3x3 identity matrix. Thus the size of the Γ matrix is 6x6.

To add the twists and wrenches in a correct way, one single reference frame has to be used. Since the body of interest is the spider, the reference frame is placed at the centre of the spider. The x-axis connects the two facing booms. The y-axis points in the direction of the remaining boom, and the z-axis points upwards. The constraints acting on the spider are given in Figure 5.4.

The DOFs given in the figure have to be represented as twists in order to see if this system is exactly constrained. The twist matrix for the first boom is given below. The columns of the matrix are the individual twists, introduced by the DOFs given in Figure 5.4.

$$T_1 = \begin{bmatrix} 0 & 0 & 1 \\ 1 & 0 & 0 \\ 0 & 1 & 0 \\ 0 & 0 & 0 \\ 0 & 0.38 & 0 \\ -0.39 & 0 & 0 \end{bmatrix} \tag{5.6}$$

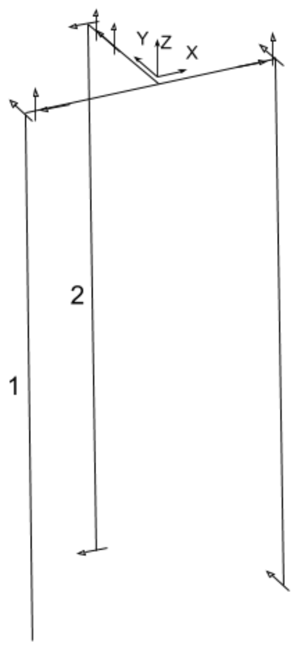

Figure 5.4: The degrees of freedom within the concept. The arrows with a hollow end represent the allowed rotation within the hinge or flexure.

Using the relation given in Equation 5.3, the reciprocal wrenches can be determined:

$$W_1 = \begin{bmatrix} -0.36 & -0.93 & 0 \\ 0 & 0 & -0.93 \\ -0.87 & 0.34 & 0 \\ 0 & 0 & 0 \\ -0.34 & 0.13 & 0 \\ 0 & 0 & 0.36 \end{bmatrix} \tag{5.7}$$

The same can be done for boom 2 and 3:

$$T_2 = \begin{bmatrix} 1 & 1 & 0 & 0 & 0 \\ 0 & 0 & 0 & 1 & 0 \\ 0 & 0 & 1 & 0 & 1 \\ 0 & 0 & 0.38 & 0 & 0.34 \\ -1.6 & 0 & 0 & 0 & 0 \\ -0.39 & -0.39 & 0 & 0 & 0 \end{bmatrix} \tag{5.8}$$

$$T_3 = \begin{bmatrix} 0 & 0 & 0 & 1 \\ 1 & 1 & 0 & 0 \\ 0 & 0 & 1 & 0 \\ 1.6 & 0 & 0 & 0 \\ 0 & 0 & -0.38 & 0 \\ 0.39 & 0.39 & 0 & 0 \end{bmatrix} \tag{5.9}$$

$$W_2 = \begin{bmatrix} 0 \\ 0 \\ -0.93 \\ -0.36 \\ 0 \\ 0 \end{bmatrix} \tag{5.10}$$

$$W_3 = \begin{bmatrix} 0.72 & -0.59 \\ 0 & 0 \\ -0.59 & -0.72 \\ -0.23 & -0.28 \\ 0 & 0 \\ -0.27 & 0.23 \end{bmatrix} \tag{5.11}$$

Now all the wrenches are known from the three booms. Since the three booms form a parallel system with the spider, the wrenches can be added. The matrix given in Equation 5.12 represents all the constraints imposed on the spider. An underconstrained system will have a rank lower than six, and thus at least one DOF is not constrained. An overconstrained system has a rank lower than the amount of columns in the wrench matrix, and thus at least one DOF is constrained by multiple constraints. An exactly constrained system has thus a wrench matrix with six columns and a rank of six, and so all DOFs are constrained, and each DOF is constrained by only one constraint. The rank of the matrix in Equation 5.12is six, thus the concept is exactly constrained.

$$W = \begin{bmatrix} -0.36 & -0.93 & 0 & 0 & 0.72 & -0.59 \\ 0 & 0 & -0.93 & 0 & 0 & 0 \\ -0.87 & 0.34 & 0 & -0.93 - 0.59 & -0.72 & \\ 0 & 0 & 0 & -0.36 & -0.23 & -0.28 \\ -0.34 & 0.13 & 0 & 0 & 0 & 0 \\ 0 & 0 & 0.36 & 0 & -0.27 & 0.23 \end{bmatrix} \tag{5.12}$$

5.3. Boom Stowed Configuration

The booms will be folded to reduce the required launch volume during launch. There are two options for storing the boom segments, either next to each other along the mounting face of the instrument bus, or stored next to each other perpendicular to the mounting face of the spacecraft bus. The two options are visualised in Figure 5.5. In the figure, it can be seen that there is more space available for the SMSS to be stowed in radial direction, and with that allow for larger boom diameters.

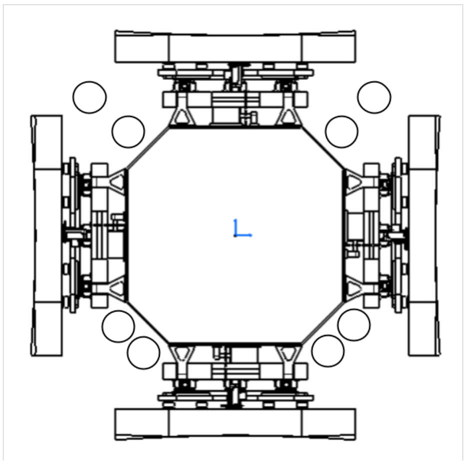

Figure 5.5: The two stowage options for the articulated booms. In the two top corners the booms are placed parallel to each other in radial direction. On the two lower corners, the booms are placed parallel to each other along the mounting face.

A trade-off is required to determine what orientation the boom segments will be stored. It was chosen to use a graphical trade-off table. To perform the trade-off, first the criteria were determined:

- Space for hinges, latches, and hard stops.
- Stiffness of the hinges.
- Interference with other systems.
- Size of the spider.

The first two criteria were seen as most important, since they both directly influence the performance of the system. More room for the hinges, latches, and hard stops means that the accuracy is less constrained by limited volume. The stiffness of the hinges influences the stability of the system when deployed. The interference with the other system is seen as less important because the DST design is still in an early phase, and the designs are still flexible. The last criterion is about the spider size. A larger spider means higher mass, but also different mechanical properties. The trade-off is given in Table 5.3.

Table 5.3: Graphical trade-off table for the orientation of the boom segments in stored position.

Options	Room for hinges	Stiffness of hinges	Interface other subsystems	Size of spider
Booms parallel in radial direction	Green Booms stored in direction with largest space	Green More room for hinges	Blue Centered between M1 segments	Blue Limited by boom rotation
Booms parallel along face	Blue Booms stored close to other subsystems over short face	Blue Asymmetric loading, small distance between contact points	Yellow Close to other systems	Green Not limited by booms

Green	Excellent	Yellow	Sufficient
Blue	Good	Red	Unacceptable

Before getting to the conclusions, first a brief explanation of the scores. On the first criterion, the first option scores better than the second. As stated before, this direction is the space limited, resulting in less space for the mechanisms. This comes also into play in the second criterion. Due to the possibility or larger hinges, the contact points between the booms can be more separated, which is beneficial for the stiffness and stability of the system. The second option has more chance of interfering with the other subsystems simply because the stored booms are closer to the primary mirror segments. The second option scores better on the last criterion. In the first option, the location of the booms in stored position require a longer spider. The spider must always radially extend further than the bottom hinge, otherwise the boom segments would intersect with each other. The second option does not have this problem, and thus scores better.

The result of the trade-off is that the first option is selected.

5.4. Hinge Tolerances

The budgets given by the optical department of the DST team cannot directly be used for the design of the SMSS. The budget provided by the optical team only gives information on the position and orientation of the mirror. This has to be translated to tolerances useful for the design of the system, like deployment accuracy and production tolerances in the components of the system. This will give the top-down budgets for the components of the system, that can be used to assess the needed precision in the components during the design. After the design is complete, a bottom-up tolerance analysis/test can be performed, which can be compared to this analysis.

The given tolerances of the mirror position are not hard boundaries, but rather represent the 2σ range of a normal distribution. It was decided to model the component errors as random distributions as well. The model was build based on the decisions made up to this point, meaning that three booms are used of which one boom restricts translation in the x, y, and z direction, one boom restricts translation in the y and z direction, and the last boom restricts translation only in the z direction.

Before the model could be made, first the method of modelling the mechanical tolerances needed to be investigated. One method is to use the extreme values of the tolerances. This results in the worst case deflection of the mirror. This method is not a statistical method, and is very simple. however this method is very pessimistic. Another option is to use the Root-Sum-Squared method, in which the tolerances are taken as normal distributions. This method is also simple, but the method is too optimistic. Both methods use unrealistic assumptions and thus the results are often not very accurate [38, 52, 56]. There are more methods developed to model the tolerances in an assembly, but most methods use the assumption that the tolerances of a single component can be approximated by a normal distribution. The tolerance value is given by the 6σ range, or $\pm 3\sigma$ from the nominal value. At this point in the design, the design of the hinges is still unknown. In the first iteration of the modelling, the hinge errors were modelled as normal distributions in a monte carlo simulation. The mirror alignment errors were then calculated with these hinge errors using the geometry of the system. The hinge errors were modelled as inputs and were altered until the resulting mirror alignment error was similar to the provided optical deployment budget. The hinge errors that resulted in this optical deployment budget are used as first estimates for the requirements on the hinges.
From this model, it became clear that the error in the hinges must be equal or smaller than 1 arcsec (1σ). With these results, a mirror position error of close to the given budget is realised. The mirror position using the given hinge errors is given in Figure 5.6.

In order to go to a deeper level, the hard stops of the hinges can be modelled instead of the hinge as a whole. According to [38, 52, 56] it is unrealistic to model the production tolerances in an assembly by a normal distribution. These papers report on the method suggested by Croft, in which the natural tolerance of the process is assumed larger than the imposed tolerance. This results in a truncated normal distribution. Croft assumed a rectangular distribution to model the tolerances. Since a rectangular distribution has more mass on the edges of the tolerance compared to the truncated normal distribution, the approximation is a pessimistic representation. On the other hand, the method does not include any bias in the production, which is an optimistic assumption. Croft suggested that those effects cancel each other, resulting in a good estimation [38, 52, 56]. For this analysis, the method of Croft is used. To get a first insight in the system, ball bearing hinges are used with hard stops with production tolerances. This decision was based on the previous design iteration, which uses ball bearing hinges for all joints. Besides the errors in the joints itself, the mounting errors are also included. From this analysis, which is for now not more than an indication on the required accuracy, it became clear that the required tolerances of the hard stops lies in the order of 0.3 micron.

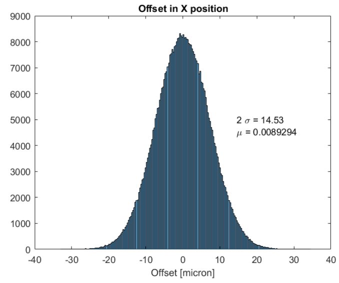

(a) X position

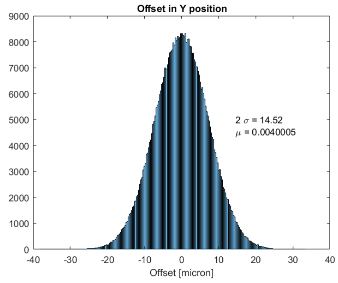

(b) Y position

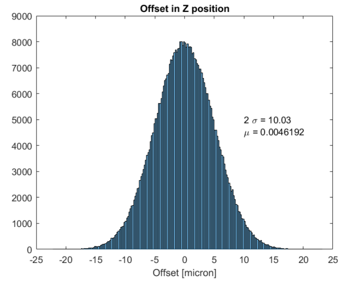

(c) Z position

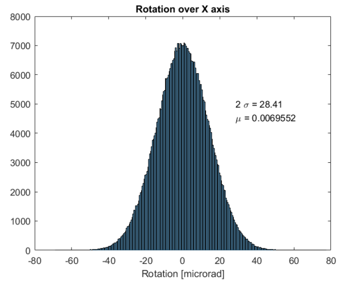

(d) X rotation

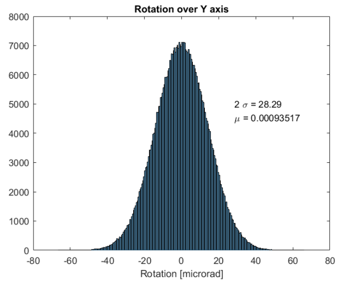

(e) Y rotation

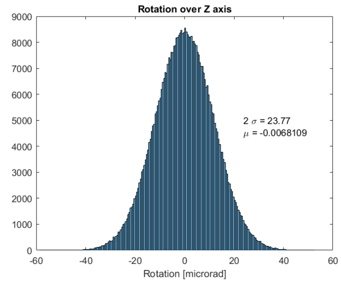

(f) Z rotation

Figure 5.6: Translation and rotation deployment tolerances of the secondary mirror, based on the tolerances of the components of the secondary mirror support structure. On the X axis, the position or rotation error is given in microns or microrad. The Y axis represent the amount of times the mirror has the given alignment offset in the monte carlo simulation.

5.5. Conclusion

In this chapter, the top level design of the SMSS was discussed. The starting point was the results of the last design iteration, performed by Lopes Barreto. It was observed that this design was overconstrained, which can result in unpredictable deformations during deployment. It was chosen to reduce the number of booms from four to three booms. This solves the constraining problem and reduces the weight of the system. However, it could result in a less stiff structure. In a later stage of the design when there is more information on the system, this trade-off has to be re-examined.

It was chosen to place the booms not parallel to each other in stowed configuration to increase the stiffness of the system. This hypothesis must still be tested.

Apart from the mid hinges, one root hinge has to be locked to exactly constrain the system. This was the outcome of the constraint analysis performed in this chapter.

Furthermore, the hinges must deploy with an accuracy with a standard deviation of 0.9 arcsec. With this accuracy, the system will deploy within the given alignment budget.

Figure 5.7 gives a top level representation of the concept chosen.

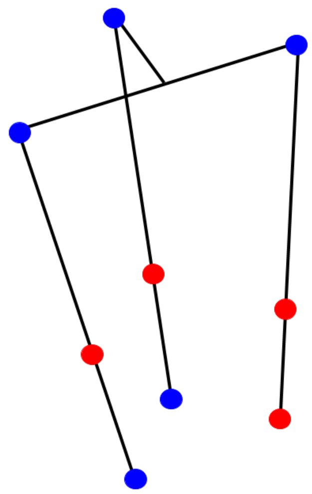

Figure 5.7: Schematic overview of the selected concept. The blue dots represent hinges, while the red dots represent latching hinges. The mirror is not drawn at the top on the spider, and the bus at the bottom is also left away.

6
System Conceptual Design

In the previous chapter, the focus was on the system as a whole. It was decided to focus first on the detailed design of the mid hinge. Before the mid hinge design can be performed in detail, first the rough concepts for the other parts of the system have to be determined. These concepts will be used in the analysis performed for the mid hinge trade-off, which is treated in the next chapter.
In the first section, the design of the spider is treated, followed by a section on the interface between the M2 and the SMSS. Then, the concept selection for the top hinge will be discussed.

6.1. Spider Conceptual Design

The spider is the structure connecting the booms and the M2. In the design made by Lopes Barreto, the spider was modelled as a stiff, flat plate. This concept was extended further in more detail. The concept was based on the space available.

Figure 6.1 gives a render of the new spider concept. The spider is made up of two perpendicular beam sections with rectangular cross sections. The width of the beams are set to 9 mm for now. This width was chosen because the gap between two primary mirror segments is 9 mm, and thus with this width the spider does not block light of the primary mirror segments. The height of the spider is for now set to 40 mm, and the thickness to 2 mm. These numbers are for now first estimates, and have to be determined later in the project.
In the Figure, the circular section is clearly visible. The flexures connecting the mirror and the spider will be placed on this circular section of the spider. From literature, it became clear that the best position to fasten a circular mirror is at 2/3 of the radius of the mirror [4, 67]. The exact mounting points have to be determined when the mass distribution of the mirror is known, however the topology optimisation of the M2 mirror is not part of this thesis.

The last features that are visible on the figure are the straight cross connections. These are placed such, that they mark the inner edge of the primary mirror segments and thus do not block the light of the M1 segments. The function of these cross connections is to increase the stiffness of the spider structure.

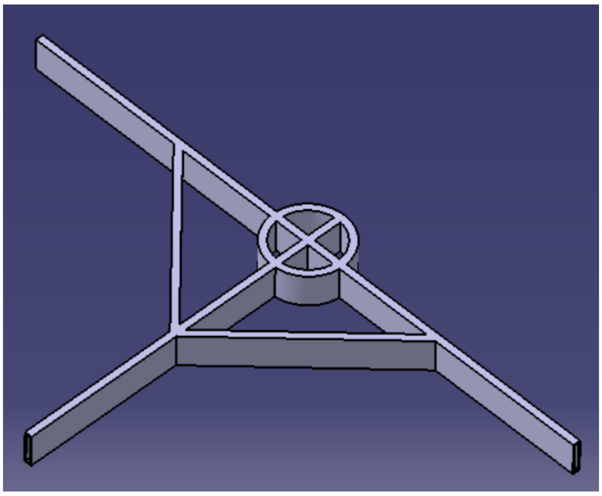

Figure 6.1: Render of the spider used in the modal analysis models.

6.2. Mirror Interface

As stated in the previous section, the mirror is connected via a support to the circular structure on the spider. The mirror should be connected to the spider in a (semi) kinematic way to prevent mirror deformations due to thermal loading. A kinematic mount has limited contact area, resulting in high stress concentrations. Semi kinematic interfaces use a larger contact area, and thus reduce the stress concentrations in the mirror. For now a simple interface is chosen with flexures. The blade flexures are equally separated over 360 degrees, centred at the mirror centre. In this setup, the compliant DOF of each flexure acts in radial direction of the mirror. The design of the flexures are taken from the work of Van Putten, which are blade flexures with a thickness of 0.5 mm [62].

6.3. Top Hinge Concepts

The top hinges form the interface between the booms and the spider. In the previous chapter it was decided to use a kinematic interface layout for the spider. This increases the complexity of the hinges, since the hinges need to allow more movement than just the rotation around the main axis. In this section, the top hinge preliminary concept is discussed.

6.3.1. Morphological Table

To identify different options, a morphological table was made from which a preliminary design is chosen. The morphological table is given in Table 6.1.

In the first column of the table, the different required functions of the concept are listed. In the columns next to that, different design options are presented. From this table, concepts can be formulated by selecting from each row a design option. However, not all combinations lead to a feasible concept. Before the concepts are generated, first the different options are briefly explained.

Location radial translation

Two of the three booms of the system have to allow for translation in the radial direction, seen from the centre of the spider. This translation can happen at two locations: in the top at the interface between the boom and the spider, or at the bottom where the total boom can rotate. When the translation is allowed in the top, it requires that the boom itself is fixed, and thus a hard stop is required at the bottom.

Rotation of the spider

For all three booms, the top hinge shall allow the spider to rotate over all three axes to prevent overconstraining the system. The first option is to use spherical joints. These joints restrict all forms of translation, but allow for rotation around all three axes. The disadvantage of these types of joints is the backlash in the joint, which is in all three directions.

Table 6.1: Morphological table for the concept of the top hinge design.

Location radial translation	At the top, connection between the spider and boom 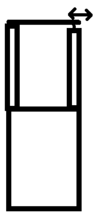	Whole boom movable, no hard stop at bottom 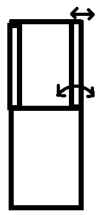		
Rotation of spider	Spherical joints 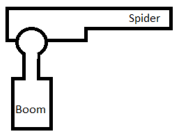 	Flexures with a simple hinge 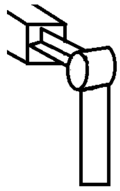	Three separate hinges in series 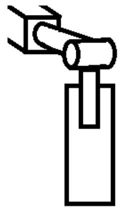	
Translation spider	Ball in groove 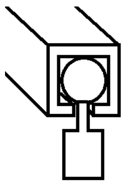	Flexures on spider 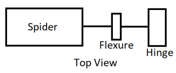 	Flexures on the boom at the spider interface 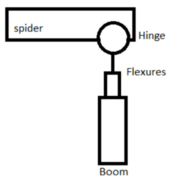 	Two degrees of freedom hinges 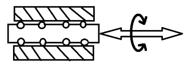

The second option is to use a 'regular' hinge with only one DOFin combination with a flexure that allows rotation around two axes. Together, rotation around all three axes is realised. Due to the large deflection required during deployment, the regular hinge cannot be replaced by a flexure. The advantage of this concept is that the flexures do not introduce backlash and hysteresis in the system. The third option is to use three one DOF hinges in series. Each hinge will allow for a rotation around an axis. Each hinge can then be made such, that backlash and hysteresis is minimised. However, this option can become complex and large in both volume and mass.

Translation of the spider
One of the booms has to allow for translation in two directions. The first option is an expansion on the spherical joint. By placing the ball in a 'groove' instead of a spherical socket, the ball can be translated along the groove. The advantage is that the functions of the hinge are bundled in a single mechanism, making it more compact. The disadvantage is that it is hard to make this system without introducing backlash into the system. The second option uses flexures to allow translation. The advantage of this option is the simplicity, it does not require moving parts. It also doesn't introduce backlash or hysteresis and can be made compact. The third option also makes use of flexures, but now they are located on the booms instead. This option is feasible when it is decided to fix the boom, and allow for radial translation at the top. Due to the bending of the flexures, it would be best to use a spherical joint at the top. The

last option is to use 2-DOF hinges. This option is based on a patent. The bearing consists of multiple rows of balls in a single race. The race is not restricted, and can thus rotate around the main axis, but also translate over this axis. An illustration of the 2-DOF hinge is given in Figure 6.2 [26].

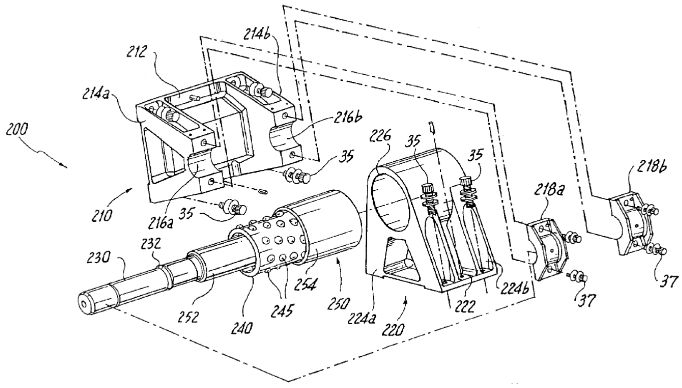

Figure 6.2: Illustration of the 2 DOF hinge as described in [26]. The numbers 240, 245, and 254 indicate the 2 DOF hinge components. Image taken from [26].

6.3.2. Concept generation

From the morphological table, several concepts were generated by combining the different options in the table. The concepts are listed below. It must be noted that not all possible combinations are taken, since it would give too many concepts to perform a good trade-off. Furthermore, the concepts are generated for the most difficult case, for the boom that has to allow translation in two directions.

- **Concept 1:** Location radial translation: Top (1), Rotation of spider: Spherical joint (1), Translation spider: Flexures on boom (3).
- **Concept 2:** Location radial translation: Top (1), Rotation of spider: Flexures with regular hinge (2), Translation spider: Combination of flexures on spider (2) and flexures on boom (3).
- **Concept 3:** Location radial translation: Top (1), Rotation of spider: Flexure with regular hinge (2), Translation spider: Combination of flexures on boom (3) and 2 DOF hinge (4).
- **Concept 4:** Location radial translation: Top (1), Rotation of spider: Three separate hinges in series (3), Translation spider: 2 DOF hinges (4).
- **Concept 5:** Location radial translation: Bottom (2), Rotation of spider: Spherical joints (1), Translation spider: Ball in groove (1).
- **Concept 6:** Location radial translation: Bottom (2), Rotation of spider: Spherical joints (1), Translation spider: Flexures on spider (2).
- **Concept 7:** Location radial translation: Bottom (2), Rotation of spider: Flexures with regular hinge (2), Translation spider: Flexures on spider (2).
- **Concept 8:** Location radial translation: Bottom (2), Rotation of spider: Flexures with regular hinge (2), Translation spider: 2 DOF hinge (4).
- **Concept 9:** Location radial translation: Bottom (2), Rotation of spider: Three separate hinges in series (3), Translation spider: 2 DOF hinge (4)

6.3.3. Trade-off and Concept Selection

From these 9 concepts, one has to be selected that needs to be designed into more detail. In this section, the trade-off will be given.

First, the type of trade-off has to be decided upon. For this trade-off, it is chosen to use a weighted average. The score different concepts can get ranges from 0 to 5. The concept with the overall highest score will be selected. The concepts will be assessed on different criteria. The criteria are listed below.

- **Nonlinear behaviour:** Moving parts introduce nonlinear behaviour in the system, which decreases the repeatability and predictability of the system, which is undesirable.
- **Complexity:** Not only the production benefits from a simple system, complex systems often have a higher failure risk.
- **Mass:** The mass of the system is important for the stability of the system after deployment, and to keep the SMSS within the mass budget.
- **Locking:** When the concept is able to be locked, the stiffness of the system can be increased when deployed, which benefits the stability of the system.
- **Compactness:** The volume of the total system in stored position is limited. A smaller volume concept is thus preferred.

The criteria will get different weights to represent the importance of the different criteria in the trade-off. The weights are determined using the Analytical Hierarchy Process (AHP). The matrix with the relative weights that was used to get to the overall weights of the criteria is given below:

$$\begin{bmatrix} 1 & 1.5 & 2.5 & 2 & 4 \\ 1/1.5 & 1 & 2 & 1.5 & 3 \\ 1/2.5 & 1/2 & 1 & 1/1.5 & 2 \\ 1/2 & 1/1.5 & 1.5 & 1 & 3 \\ 1/4 & 1/3 & 1/2 & 1/3 & 1 \end{bmatrix} \tag{6.1}$$

The order of the criteria are the same as presented above, thus criterion 1 is nonlinear behaviour, criterion 2 is complexity, criterion 3 is mass, criterion 4 is locking, and criterion 5 is compactness. The results are given in Table 6.2.

Table 6.2: Weights as used in the top hinge concept trade-off

Criterion	Weight
Nonlinear behaviour	0.35
Complexity	0.25
Mass	0.13
Locking	0.19
Compactness	0.08

With these weights the actual trade-off between the concepts can be performed. The trade-off is given in Table 6.3.

Table 6.3: Trade-off table for the concepts for the top hinge design. The scores range from 0 to 5.

	Nonlinear behaviour	Complexity	Mass	Locking	Compactness	Total
Weight	0.35	0.25	0.13	0.19	0.08	
Concept 1	2	3	4	2	3	2.59
Concept 2	4	3	3	3	2	3.27
Concept 3	4	2	3	3	3	3.10
Concept 4	3	1	1	4	1	2.27
Concept 5	2	4	4	3	5	3.19
Concept 6	3	4	4	3	5	3.54
Concept 7	5	5	4	3	5	4.49
Concept 8	5	4	4	3	5	4.24
Concept 9	4	2	1	4	2	2.95

From this trade-off table, several things can be concluded. First of all, the concepts having the radial translation at the top score on average worse than those at the bottom. The reason for this is that the system would become more complex since the booms have to be locked at the bottom with high precision. To then allow for translation, an extra DOF has to be introduced in the top. This results in an heavier, more complex solution.

The spherical joint performs worse than the flexure-regular hinge combination in this trade-off. Reason for this is that the spherical joints requires some backlash in order to function properly. Since the spherical joint has to rotate over all three axes, the backlash is also present in all three axes, making it less predictable. Normal ball bearings also have backlash, but since this is only in one direction, the backlash can be minimised more easily. The regular hinge is only used for the axis over which a larger rotation is required. For the other rotations flexures are used. The third option, using three regular hinges in series, has the main downside that it is a complicated system. Due to the complexity, the predictability of the system decreases. Minimising backlash and other forms of nonlinear behaviour is then harder to control. Furthermore, the mass and volume may increase significantly.

The trade-off shows that concepts 7 and 8 perform the best. The concepts are rather similar. They both use a combination of a regular hinge and flexures to account for the rotations. The difference lies in the method of allowing translation. Concept 7 uses a flexure attached to the spider, while concept 8 uses a 2 DOF hinge. The reason that concept 7 wins, is that the concept already uses flexures to account for rotations. With a minor change to the flexure, it can also allow for translation. This saves extra complexity and mass. This means that the final concept of the top hinge is concept 7, which has a regular hinge for the large deflection during deployment.

It must be stated that this trade-off was performed at a top level. Not much is known about the system's behaviour. It is thus very important to keep in mind that results of future analyses can prove some assumptions made in this trade-off invalid, and can thus change the outcome of this trade-off. This concept was thus selected to be used as baseline, but it was kept in mind that the trade-off has to be critically reevaluated when more information about the system is known and that the outcome of this trade-off is not written in stone.

6.3.4. Flexure Design

The rotation about the axis parallel to the spider can be provided by a cruciform flexure. The rotation about the axis parallel to the boom can be provided by a simple strip flexure. The last boom has also to facilitate an extra translation. This can be done by connecting two simple strip flexures connected to each other [63]. The flexures are given in Figure 6.3.

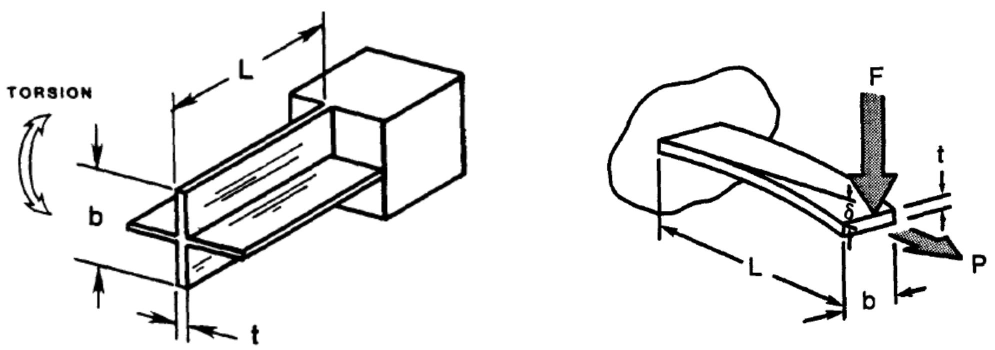

(a) Cruciform flexure

(b) Single strip flexure

Figure 6.3: General layout of the cruciform and single strip flexures. Images taken from [63].

The material of the flexures is an important parameter in the design of the flexures. The largest compliance of a given flexure is given by the material with the largest reduced tensile modulus, the ratio between the tensile modulus and the Young's modulus. Further, creep is an issue with flexures. A rule of thump is that the higher the melting temperature, the higher the creep resistance of a material is [63]. Titanium has a high reduced modulus and a high melting temperature. For that reason, titanium is chosen as material for the flexures for now. Due to its properties, titanium is often used for this application [3, 4, 22, 67].

In this application, the flexures have to allow for multiple DOF. This can be done by putting two flexures into series [63]. The cruciform flexure and the strip flexures can be combined into a single flexure. By starting with a full cruciform form, and then removing the last part of the horizontal flanges, the flexure also allows for rotation along the vertical axis. This concept can be seen in Figure 6.4b. When doing the same at the other end of the cruciform flexure, also translation in the horizontal direction perpendicular to the flexure is allowed. This concept can be seen in Figure 6.4a.

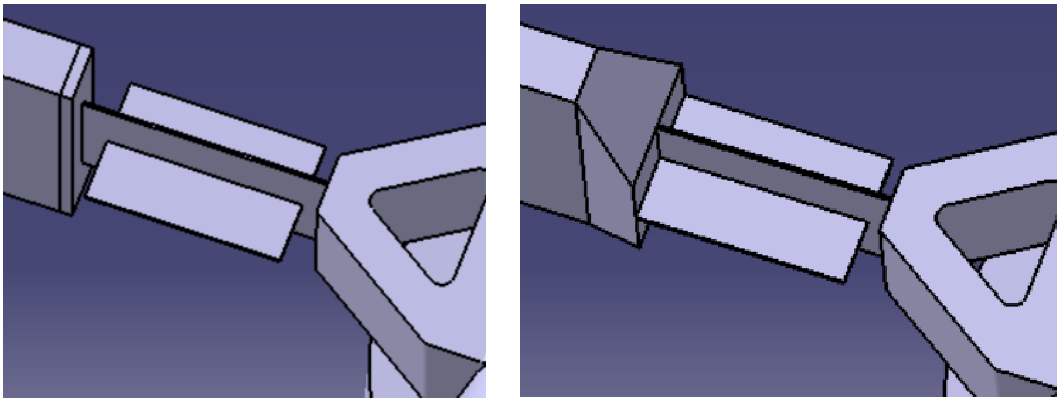

(a) (b)

Figure 6.4: Renders of the two flexure types used to attach the spider to the rest of the structure. In a), the flexure with two rotational and one translation degrees of freedom is given. In b), the flexure with only two rotational degrees of freedom is given.

The flexures were sized using hand calculations on the deflection of the spider under different load cases. The load case depends on the flexure type under consideration. The first flexure to be sized was the flexure allowing small rotations about the vertical z axis. When the flexure bends due to misalignment or deployment errors, a moment will develop within the flexure which is transmitted to the spider. The spider will also deform under the applied moment. When taking a limit allowed deformation of the spider, a maximum moment can be determined. With this moment and the maximum rotation of the flexures from the budgets, the dimensions of the flexure can be determined.

The deformation of the spider can be calculated using standard deformation cases from the *Handbook of Solid Mechanics* [58]. The spider is deformed by two moments on each end, which is represented by case 5 on page 349 of the book. The case is given in Figure 6.5.

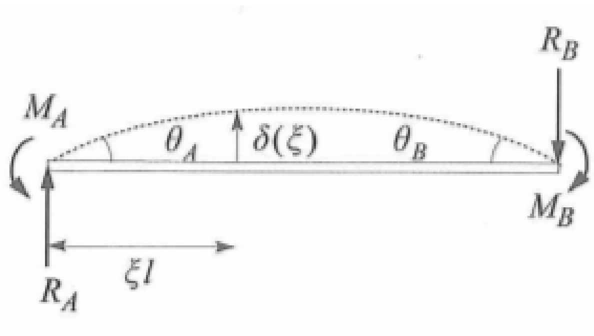

Figure 6.5: Deflection of a beam under two moments applied on each end of the beam. Image taken from [58].

The deflection of the beam under the load specified in Figure 6.5 can be calculated by the following equation [58]:

$$\delta(\xi) = \frac{l^2}{6EI}\left[M_A\left(2\xi - 3\xi^2 + \xi^3\right) + M_B\left(\xi - \xi^3\right)\right] \tag{6.2}$$

In this equation δ is the deflection of the beam, l is the total length of the beam, E is the Young's modulus of the material of the beam, I the moment of inertia of the beam, and ξ is defined as x/l, where x is the location on the beam and thus $0 \leq \xi \leq 1$.

In this particular case the two moments on the ends of the spider are equal in magnitude and direction (the flexures on each end are equal). Using the definition of a positive moment of M_B, it means that $M_B = -M_A$ in Equation 6.2. This means that the equation can be rewritten to:

$$\delta\left(\xi\right) = \frac{Ml^2}{6EI}\left(\xi - 3\xi^2 + 2\xi^3\right) \tag{6.3}$$

The maximum deflection occurs at $\xi = 0.2113$. The maximum deflection of the spider under the load was set to 0.5 micron. This is 1/30 of the maximum offset of the mirror and was seen as a good first estimate.

For the torsional flexures, the same approach was used. The torsion of a beam with a torque applied can be calculated as follows [58]:

$$\Theta = \frac{M_v L}{GK} \tag{6.4}$$

Where M_v is the applied torque, L the length of the beam, K the torsion constant of the cross section, and G the shear modulus. In Chapter 6, it was decided to produce the spider from thin walled rectangular tubes bonded together. The torsion constant for a thin walled rectangular cross section can be calculated with [58]:

$$K = \frac{4\left(hb\right)^2}{2\left(\frac{b}{t} + \frac{h}{t}\right)} \tag{6.5}$$

Where h is the height of the cross section, b the width of the cross section, and t the thickness of the wall. For open cross sections build up from n strips, another equation can be taken [58]:

$$K = \sum_i \frac{h_i t_i^3}{3} \tag{6.6}$$

In this equation, h_i is the height of one strip, t_i is the thickness of the strip. A cruciform flexure can be seen as two equal sized strips. The equation then simply becomes:

$$K = \frac{2}{3} h t^3 \tag{6.7}$$

With Equations 6.4-6.7 the dimensions of the flexure can be determined. For a maximum deflection angle of the spider a value of 10 microrad was taken, which is 1/10 of the allowable deployment budget. The rotation range the flexure has to provide was taken to be 200 microrad, which is the deployment budget with a safety factor of 2. The results for both flexure types are given in Figure 6.6.

A material thickness of 0.5 mm was chosen, based on the flexures used by B. T. van Putten in his thesis [62]. This results in a bending flexure length of about 1.7 mm and torsional flexure of about 26 mm. However, the edges of the flexures have to be rounded at the interface with the structure to prevent high stress concentrations. To account for this, a first length of 4 mm was taken for the bending flexure, and 31 mm for the torsional flexure. These flexure sizes are probably too large, since the stiffness of the spider is underestimated. Currently, it is considered a straight beam, but due to cross links, the stiffness will be larger in reality. However, since for now the main focus lies on determining the performance of the midhinges, the flexures are taken as they are now.

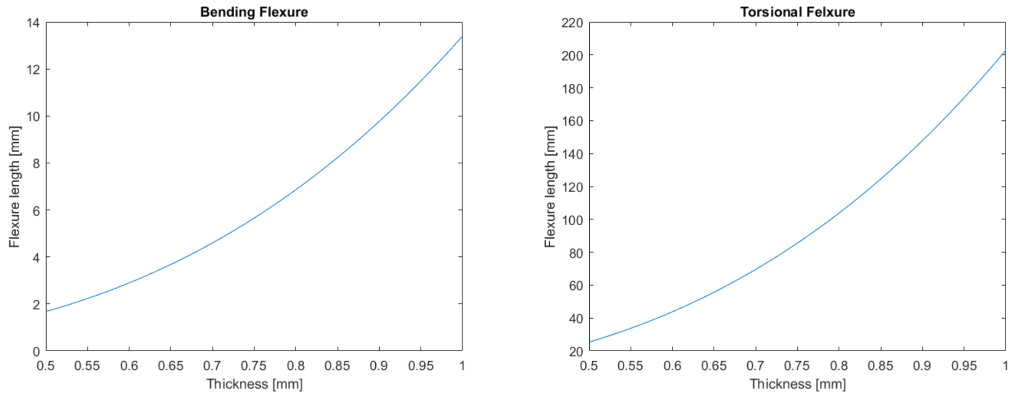

(a) Bending (b) Torsion

Figure 6.6: Results of the preliminary flexure sizing. In a) the required length of the bending flexure is given as function of material thickness. In b), the required length of the torsional flexure is given as a function of the material thickness.

6.4. Conclusion

In this chapter the top level concept selection was performed for the spider, mirror interface, and top hinges. These concepts are used as baseline in the analyses performed in next chapter. In the first section, the layout of the spider was given. It was decided to make the width of the spider legs 9 mm. With this width, the legs do not block any light of the M1 segments. Two cross beams were added to increase the stiffness of the spider. The mirror itself is mounted on the circular section of the spider with three blade flexures. The top hinge concept that was selected is a combination of a single DOF hinge and flexures. The hinge allows for the large deflection required during deployment, while the flexures allow for small translations/rotations to keep the system exactly constrained. The trade-offs performed in this chapter are performed on a top level. When more information about the system becomes available during the design process, the trade-offs have to be critically reevaluated to check if the assumptions made are still valid.

7

Mid Hinge Concept Selection

It was decided to start the design process with the mid hinge concept selection. In the previous chapter, the preliminary concept selection for the spider, mirror interface, and top hinges were performed. These concepts form the baseline design for the mid hinge concept selection in this chapter. The chapter starts with the considered concepts for the mid hinge, followed by a section discussing the trade-off criteria. During the process, it was found that extra analysis on the stiffness of the concepts was needed. This was done by modal analysis in ANSYS. after that, the actual trade-off for the mid hinge is presented.

7.1. Mid Hinge Concepts

Before any concept selection can take place, first the concepts have to be generated. That will be done in this section. An overview of the concepts considered will be given, after which the concepts are explained in more detail.

To get from stored to deployed position, the hinges have to rotate over 180 degrees. After deployment the two halves should be locked in order to form a single, rigid boom. If the joint would not be locked the system would have extra DOF, which makes the system underconstrained. Furthermore, the locking and latching must be performed with high accuracy. Any errors in locking has a direct influence on the positioning of the secondary mirror. The options considered in this concept selection are given below. These options were identified during the literature study.

- Ball bearing hinges
- Strain energy deployment hinges
- Shape Memory Composite (SMC) hinges

These concepts will be briefly explained in the following text.

7.1.1. Ball Bearing Hinge

This type of hinge is the more common hinge compared to the other two options. It consists of two halves, joint together over an axle with ball bearings. The ball bearings supply a good load path between the two segments while keeping the contact area close to non-conform, limiting the nonlinear behaviour of the system.

The advantage of this type of hinge is that after latching, it forms a stiff link and will resist rotations over all axes. Furthermore, both the deployment and the locking can be made controllable, reducing shock loads in the system [61].

The disadvantage of this type of hinge is that the mass is relatively high. This will have an influence on the dynamic behaviour of the system. If the hinge needs to be locked, a separate locking mechanism has to be included in the design. This will increase both the complexity and the mass of the system. The thermal conductivity of the hinge might be an issue as well. The contact area between the two hinge halves will be small to keep the accuracy of the system high. This will limit the thermal conductivity between the two halves of the boom which can cause gradients, and with that deformations of the system [61].

HTS GmbH is currently developing a hinge of this type, the Articulated Boom Deployment System Hinge (ABDS). This hinge has a latch mechanism included, together with a driving motor. It is developed for articulated booms of 6 m and larger. In the current state, the hinge measures 185x98x247 mm with a mass of 3.5 kg [24]. When this option is used, the current hinge design has to be downscaled to a size more suitable for the DST. The development time for this is long, around 18 months according to the company. In Figure 7.1, the ABDS hinge in its current form is presented.

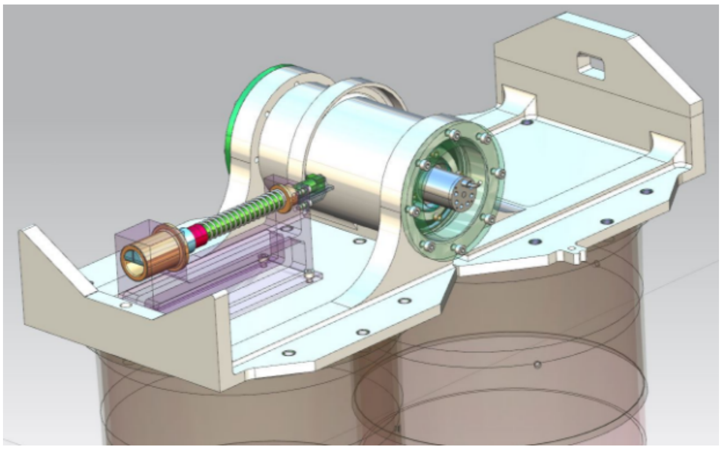

Figure 7.1: The ABDS hinge system as developed by HTS GmbH. Image taken from [24]

7.1.2. Strain Energy Deployment Hinge

The working principle of this type of hinge is based on the elastic deformation of the hinge material. When released, the stored elastic energy drives the deployment of the hinge up to the deployed state, where the hinge is locked due to its shape. A good example are the tape springs, which work according to the same principle as measuring tape. Another form of hinge is the integral hinge. This can be used in a CFRP tube. At the location where the hinge is required, two opposite facing slits are cut into the tube. This allows the tube to bend over this area. An example of an integral slotted hinge is given in Figure 7.2.

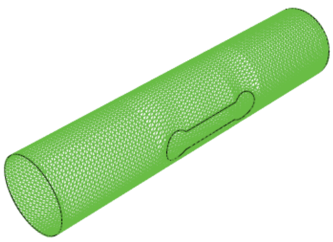

(a) Deployed

(b) Stowed

Figure 7.2: An example of a integral slotted hinge in deployed and stored configuration. Images are taken from [45]

Since the hinge is self locking, the hinge system is a simple, lightweight solution. However, in this application also the accuracy of the hinge is important. In several studies, it was proven that this type of hinges is capable of arsec deployment accuracy, although the accuracy is dependent on the shape and material of the hinge. Some of the hinges do not reach this accuracy [5, 18, 23, 55, 61, 65]. Since integral hinges are actually part of the boom, there are no contact points where the conductivity is hard to predict. Besides conductivity, the CTE of the hinges are generally also very low [65].

Like all systems, this mechanism has also some drawbacks. First of all, the behaviour of the hinge is dependent on temperature. In the Mars Express mission, one of the antennas did not deploy since the low temperature decreased the internal moment in the hinge. This problem was solved by turning the spacecraft, putting the hinge in sunlight which raised the temperature of the hinge [1, 49]. Furthermore, this type of hinge can suffer from creep. Due to long storage times, the response of the hinge is influenced, resulting in a lower deployment torque and longer creep recovery times [6]. For the DST, this would mean that the system is only fully deployed after the creep has recovered. Only then, the optical system can be calibrated. In [55], a high precision hinge that fulfils the requirements for the DST is presented. However, in the data presented a clear drift in some of the parameters can be seen.

One of the companies that have experience with integral hinges is SpaceTech GmbH in Germany. This company designed the boom for the ESA JUICE mission. Some information concerning this boom was obtained after a phone call with Mr. P. Greff, which is discussed below.

(a)

(b)

Figure 7.3: The integral slotted hinge as used in the design of the boom for the ESA JUICE mission. Image is taken from [25]

The hinges used in the JUICE mission were a one off product, since the design of this type of hinge is very specific for the application. However, the size of the hinge is not very limited. The JUICE mission uses booms with a diameter of 40 mm, but 60 mm shouldn't be a problem either, just like diameters below 40 mm. The thickness of the wall of the tube was 0.4 mm and the slotted area was about 20-25 mm long.

The deployment accuracy of the hinge is high. When giving the required alignment budget of 15 micron, Mr. Greff did not foresee problems. It would become difficult when sub-micron precision would be required.

The stored energy within the hinges depend on the design. When there is no friction in the system, the system will always deploy, albeit slower with lower levels of stored energy or higher inertia of the to be deployed system. A high level of stored energy may result in overshoot during deployment. However, due to the design of the hinge, the hinge will eventually lock after a view oscillations. Dampers or stops can be implemented to stop the system from overshooting, however this will add extra mass to the system. Another point is the inertia. During deployment a high inertia will limit the deployment speed, but can also cause overshoot. During operations high inertial forces due to high slew rates can cause the hinge to collapse and fold again. No damage is done to the hinge when this happens, and it will return to the locked position when in rest again. This could be harmful for the calibration of the system though.

The thermal properties of the hinge, and thus boom, are dominated by the layup of the fibres. The hinge uses a layup of 0-(15-20)/90 degrees. There is still some room to play with the layup, but it is limited. According to Mr. Greff, the system can be made with a CTE close to zero. The conductivity cannot be changed that easily, only by varying the fibre type. At elevated temperatures the stowed hinge can suffer from creep. The temperature at which this starts to be a problem is around 100 degrees Celsius. After deployment, the maximum allowable temperature depends on the matrix, and will be around 200-250 degrees Celsius. To prevent creep, it is beneficial to deploy quickly after launch.

During locking, only small shock loads are introduced to the system. The shocks are lower than during launch or due to spring loaded devices.

In the design, it is important to first find the required diameter of the booms. The diameter is increased until the system is stiff enough while having a wall thickness less than 0.5 mm. This thickness is about the limit with which still the folding of the boom is possible. To take the stiffness reduction due to the hinge into account, the stiffness of the boom should be 20% less than the stiffness of the boom without hinge. A summary of the phone call can be found in Appendix A.

7.1.3. Shape Memory Composite Hinges

The shape memory composite (SMC) hinges use the shape memory property of the material to actuate the hinge during deployment. The hinge is made from a composite with a shape memory polymer. The hinge is being produced in the deployed orientation. Before launch, the hinge is bend in the stowed position. This has to be done at a temperature higher than the glass temperature of the polymer. When the system has to deploy, the hinge is heated above the glass temperature of the polymer. At this temperature, the hinge will start to move to its original position. When the hinge is then cooled below the glass temperature of the polymer, the hinge is rigid again [9]. An example of a SMC hinge is given in Figure 7.4.

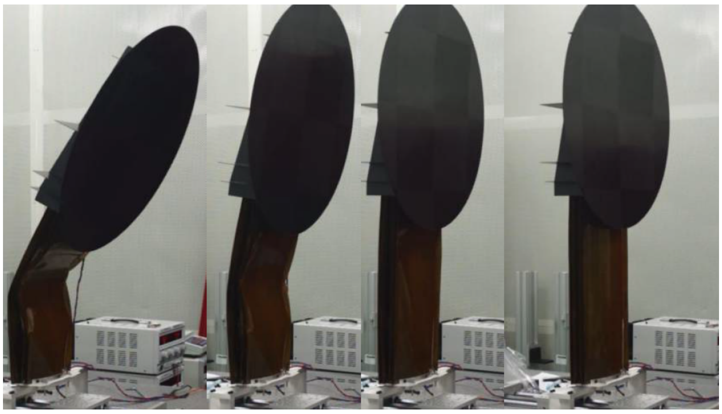

Figure 7.4: An example of a SMC hinge. In the figure, the deployment sequence of the hinge is presented. Image taken from [9]

This hinge mechanism has several advantages for the DST. First of all, the complexity of the system is low. There are no moving parts, and the hinge is formed by a small number of components. When the SMC is combined with a tape spring, the stiffness of the hinge in deployed condition is high. Just like with the strain energy hinges, the SMC hinges have a direct, continuous thermal path between the two halves of the boom. This reduces the thermal gradients in the booms, and thus thermal deformations.

The disadvantage of this hinge is the limited accuracy that can be reached. The hinge that is produced and tested by [9] reached a shape recovery of 99.994%. For a storage angle of 180 degrees, the deployment error is then 0.01 degree, or 38.9 arcsec. According to earlier defined tolerances in Chapter 5, this is not accurate enough for the application intended here.

7.2. Trade-off Criteria

From the three hinge type concepts listed in this section, one has to be chosen to be designed in more detail. However, since the SMC hinge cannot reach the required accuracy, only the ball bearing hinge and the strain energy hinge are considered. The type of trade-off was chosen to be a weighted average, just like the trade-off of the top hinge concept discussed in the previous chapter. The trade-off criteria for this trade-off are slightly different from the previous trade-off due to the different function of the hinges. The criteria are given below:

- **Deployment accuracy:** The mid hinges must be locked with high precision in order to reach the required micron level precision.
- **Complexity:** More complex systems have a higher chance on failure.
- **Mass:** The mass of the system is an important factor in the launch cost. Since the goal of the DST is to develop a relatively low cost high resolution telescope by decreasing the launch cost, mass is an important factor in the design. Furthermore, the subsystem has to stay within the given mass budget.
- **Thermal behaviour:** The mid hinges play an important role in the heat transport of the system. A poor thermal conductance can introduce thermal gradients in the system and with that deformations of the system.
- **Post deployment stiffness:** The stability of the optical system is important for the quality of the images, and thus important to the success of the mission. The stiffness of the structure is an important factor in the post deployment stability of the optical system.

The weights of each criterion is again determined by the use of the AHP method. The matrix used in this process is given below. The criteria appear in the order as presented earlier.

$$\begin{bmatrix} 1 & 2 & 3 & 1 & 1 \\ 1/2 & 1 & 2 & 1/2 & 1/2 \\ 1/3 & 1/2 & 1 & 1/3 & 1/3 \\ 1 & 2 & 3 & 1 & 1 \\ 1 & 2 & 3 & 1 & 1 \end{bmatrix} \tag{7.1}$$

From this matrix, the relative weights of the criteria can be obtained. The result is given in Table 7.1.

Table 7.1: The weight of the trade-off criteria relative to each other.

Criterion	Weight
Deployment accuracy	0.26
Complexity	0.14
Mass	0.08
Thermal behaviour	0.26
Post deployment stiffness	0.26

The trade-off criteria and their relative weights are now determined. In order to perform a good trade-off, first information on the performance on these criteria by the concepts have to be gathered. The first three criteria can be assessed by looking at comparable systems or at the design of the concepts itself. For the last two criteria , thermal behaviour and post deployment stiffness, more information is required. At this point, the thermal design and environment are not yet detailed enough to perform an analysis that provides useful data, the analysis would be accumulation of assumptions. It was considered that the results would not provide any extra value to a top level reasoning. For that reason it was decided to not perform a thermal analysis at this point. The other criterion is the post deployment stiffness. It was chosen to base the mid hinge concept trade-off on the results of the modal analysis of the concepts. The modal analysis will give an indication on the deployed stiffness of the concepts. Besides that, the analysis will give the modal shapes, which can be used as an indication of the weak points of the concepts. To prepare for the trade-off, the next section will present the modal analysis of the two concepts considered.

7.3. Modal Analysis

The stiffness of the concepts strongly influence the stability of the telescope. The modal response of the system depends on both the mass and the stiffness of the system. The modal analysis was performed with ANSYS, and checked by simplified hand calculations.

The difference between the CAD models will only be in the mid hinge, and thus the top and root hinges are modelled the same. This also applies to the mirror, the spider, and the flexures. The preliminary design of these components were discussed in the previous chapter.

After the full CAD models were build, the models were ready for preparation for the analysis, which is mainly preparing the models for the meshing. In order to get a good mesh, some parts require some smart slices and removal of split faces. The preparation is discussed after the subsections concerning the design of the models. When models were ready, the analysis was performed. The results are discussed at the end of this section.

In this analysis, three materials are used: titanium for the hinges, CFRP for the booms and spider, and silicon carbide for the mirror. The properties of the materials used are listed in Table 7.2.

Table 7.2: Material properties used in the modal analysis.

Property	Titanium	CFRP	Silicon Carbide
Density [kg/m^3]	4620	1420	3100
Young's modulus [GPa]	96	61.34 (x,y) 6.96 (z)	410
Poisson's ratio [-]	0.36	0.3 (xz, yz) 0.04(xy)	0.14
CTE [$10^{-6}m/m/K$]	9.4	2.2	4

7.3.1. Hand Calculations

In order to perform a simple hand calculation, the model is simplified. The booms will be the dominant feature in the stiffness of the system. The system can be modelled as a simple cantilevered beam with a tip mass. The mass of the tip is in this case the combined mass of the hinges, spider, and mirror. The total mass is 4.71 kg. This value was taken from the model used for the modal analysis, which is discussed later.

The natural frequency of a structure can be calculated with the following equation [34, 58]:

$$f_n = \frac{1}{2\pi}\sqrt{\frac{k}{m}} \tag{7.2}$$

Where k is the stiffness of the structure. For a cantilevered beam, the stiffness is [34]:

$$k = \frac{3EI}{l^3} \tag{7.3}$$

As stated before, the system has three booms. When all hinges would be locked, all three booms would act as cantilevered springs, and the system stiffness would be simply three times the stiffness of the boom. With this assumption, the eigenfrequency of the system with integral slotted hinges would be 6.9 Hz. Taking the 20% decrease in stiffness due to the integral slotted hinge into account, the first eigenfrequency decreases to 6.2 Hz. For the system with ball bearing hinges, the first eigenmode is assumed to be similar to the first mode of the integral slotted hinge concept, so a translation of the spider. It is assumed that the mass of the mid hinge will start playing a role in the second eigenmode of the booms, not in the first. With this assumption, the first eigenmode of the system with three root hinges locked is 13.4 Hz.

However, the root hinges are not all locked. If the structure starts to vibrate such that the second boom hinges will rotate, the second boom is not bending, and the stiffness of the system is provided by only two booms. The first eigenfrequency in this case then reduces for the integral slotted hinge to 5.6 Hz, or 5 Hz with a stiffness reduction of 20% due to the integral slotted hinge. For the ball bearing concept, the eigenfrequency is reduced to 10.9 Hz. It must be stated that this hand calculation only takes the stiffness of the booms into account. The flexures and the spider stiffness are not considered in this calculation. The hand calculations may thus be an overestimate of the results. the results of the hand calculation is summarised in Table 7.3.

Table 7.3: First eigenfrequencies as found by hand calculations

Concept	3 booms	2 booms
Concept 1	6.2	5
Concept 2	13.4	10.9

7.3.2. Models

In the previous sections, some of the components of the model were already explained. In this section, the models used for the first modal analysis are presented.

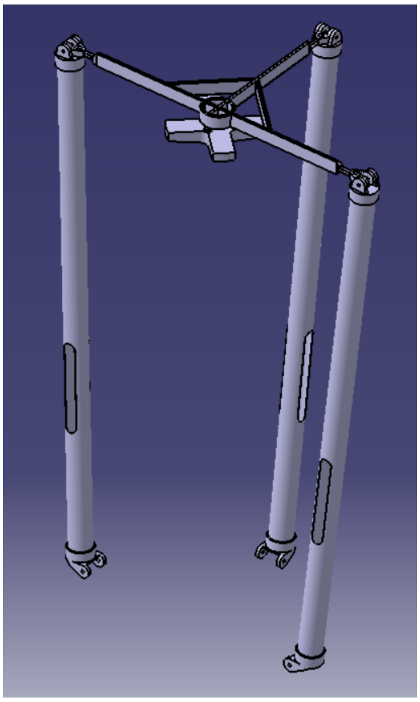

(a) Strain energy hinge

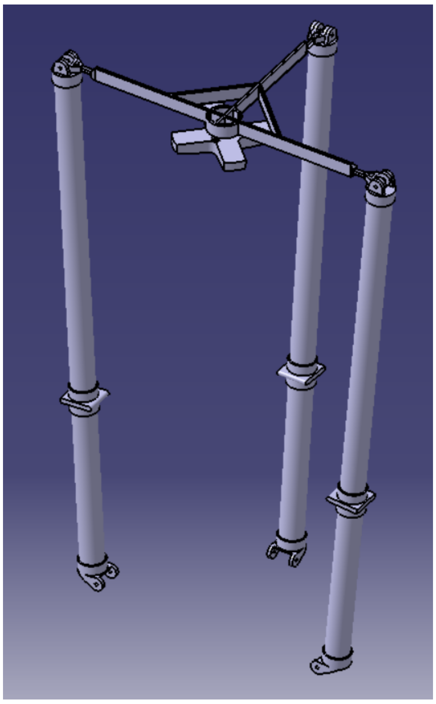

(b) Ball bearing hinge

Figure 7.5: The models used for the first modal analysis. In a), the model using strain energy hinges is given. In b), the model with the ball bearing hinges is given.

The main difference between the two models is in the booms. The model with the strain energy hinge (Figure 7.5a) has booms with a thickness of 0.5 mm. This thickness was based on the thickness limitations of the strain energy hinge explained by P. Greff of SpaceTech GmbH. The hinge is created by cutting out two slots in the boom. The radius of the slot is 17.5 mm, and the centres of the curvature are 250 mm apart. The lowest centre is 425 mm above the root of the boom.

The thickness of the boom for the ball bearing concept is not limited. It was chosen to take a thickness of 2 mm to make the difference between the two concepts large, since the larger thickness of the boom is an advantage of this concept. The hinge itself was modelled as a simple, solid part that could not rotate. The ball bearing and strain energy hinges are located at the same place in the boom.

After the models were created in CATIA, they were imported in ANSYS for the analysis. Before any analysis could be performed, the models first had to be prepared. The spider and the top hinges were sliced in several subparts in order to get sweepable bodies. The subparts still formed a single part in the model, so a continuous mesh was formed. Some surfaces were split in several faces due to conversion errors from one software to the next. Split surfaces were repaired, which will increase the number of hex elements in the model and increase the quality of the mesh.

The booms, the spider flexures, and part of the spider were made into midsurfaces. This was done because the thin shells would result in a very poor mesh. When transformed into midsurfaces, the mesh quality increased significantly, the skewness went to close to zero and orthogonal quality close to one. Only the central circle of the spider was not modelled as midsurfaces, since this gave problems during meshing. The circle was sliced in six subparts of which four were sweepable. This left only relatively small parts that could not be swept, and had a bad quality mesh. The meshes used for the analysis can be seen in Figure 7.6.

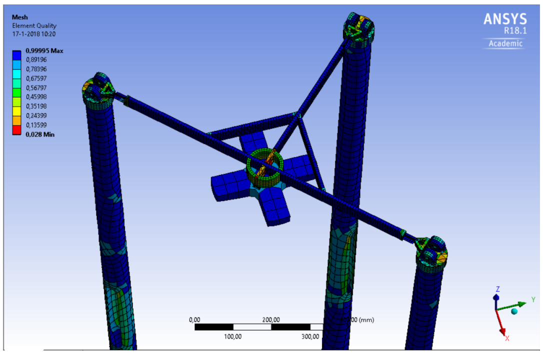

(a) Top part of the strain energy hinges concept mesh.

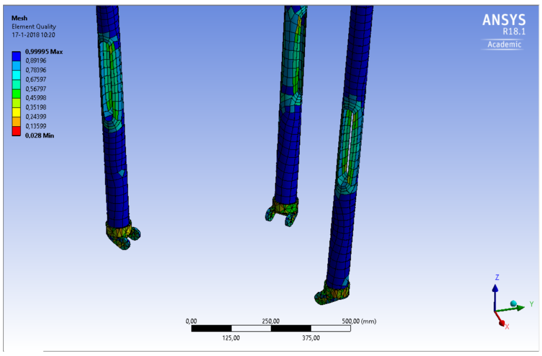

(b) Lower part of the strain energy concept mesh.

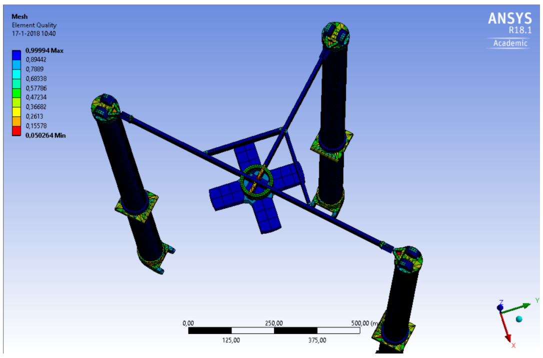

(c) Top view of the ball bearing midhinge concept mesh.

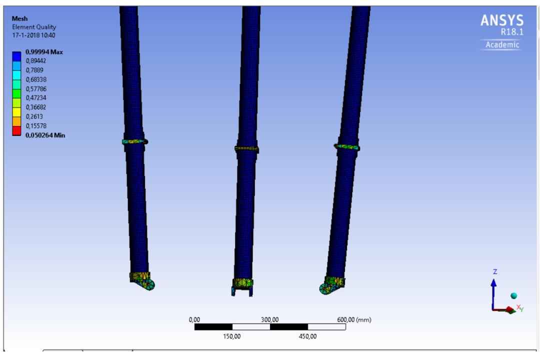

(d) Lower part of the ball bearing midhinge concept mesh.

Figure 7.6: Mesh quality of both concepts.

Both models were subjected to the same boundary conditions. The top hinges were not locked and modelled as revolute hinges. Two of the root hinges (the two most left in the figures) were modelled as revolute hinges with the ground as base. The last root hinge was modelled to be latched, and thus a fixed link was used. The contact between the remaining components were modelled as bonded contacts. The results of the modal analyses are the first six eigenfrequencies of the model, together with their modal shapes.

7.3.3. Results

The results of the first modal analysis are presented in this section. The eigenfrequencies of the two concepts are given in Table 7.4. In Figure 7.7a, it can indeed be seen that the second boom does not bend during the modal displacement, but rather it hinges over its top and root hinges. The two boom approximation in the hand calculation is thus valid.

Table 7.4: Results of the first modal analysis. The table gives the results of the first 6 modes of the concepts, given in Hertz. Concept 1 is the concept with the strain energy hinges, concept 2 is the concept with the ball bearing mid hinges.

Mode	Concept 1	Concept 2
1	4.16	7.66
2	4.30	8.32
3	10.30	20.94
4	22.62	23.82
5	23.06	27.81
6	31.61	36.81

Comparing these results with the hand calculations, it can be seen that the calculations using two booms are closer to the ANSYS results. For the integral slotted hinge concept, the difference is about 0.8 Hz. For the ball bearing hinge concept, the difference is larger. This difference can be explained using the modal shapes given in Figures 7.7 and 7.8. Especially for the ball bearing hinge concept, the flexures and spider seem to have a large influence on the modal shape of the system. The stiffness of these parts are not taken into account in the hand calculations. By comparing the simplified hand calculations and the ANSYS results, it can be concluded that both results are similar. It is important to note that even though the hand calculations seem to agree with the ANSYS results, it is important to perform tests on the system to validate the results. This means that the results of the analysis can be used for the trade-off, although a critical attitude towards the results must be kept.

In Table 7.4, it can be seen that the concept with the ball bearing hinges has higher eigenfrequencies. Especially in the first three modes the difference is in the order of 2. In the higher modes, the difference becomes relatively less. Although the eigenfrequencies are higher, the first eigenfrequency is low in both cases.

Next to the frequencies, ANSYS also gives the modal shapes of the concepts. The modal shapes are given in Figures 7.7 and 7.8. From these figures, it can be seen that the modes are similar in both concepts. However, some of the modes are swapped. Mode 1 and 2 are swapped, and modes 4 and 5 are swapped.

Furthermore, it can be seen that the flexures are allowing for the movement where they are designed for. However, in this analysis these movements become unwanted. This influence of the flexures to the modal response of the system has to be investigated.

In eigenmode 5 of the integral slotted hinge concept and mode 4 of the ball bearing mid hinge concept, it can be seen that the top hinges play a significant role in the movement. This can better be seen in Figure 7.9, where a front view of the 5^{th} eigenmode of the integral slotted hinge concept is given. Apart from the top hinges, it looks like the root hinges have also a role in the modal shapes of the concepts. Especially modes 1 and 2 of both concepts seem to be influenced by the degree of freedom of the hinges. Since it looks like the hinges have a significant role in the eigenmode, it is interesting to investigate what the response of the system is when all the hinges are locked after deployment, both root and top hinges.

These possible investigations is for a later stage in the design. First, the mid hinge concept has to be chosen. That will be done in the coming section.

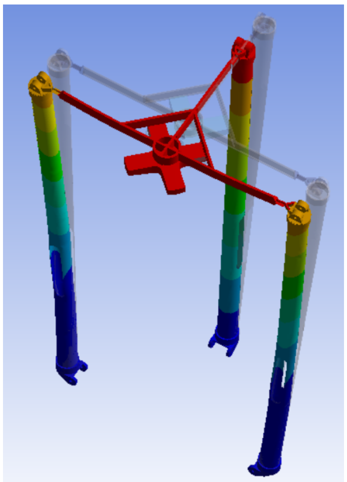

(a) Mode 1

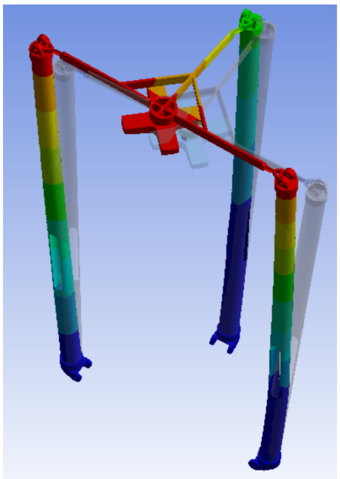

(b) Mode 2

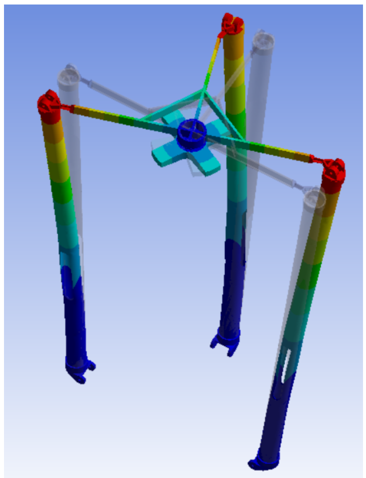

(c) Mode 3

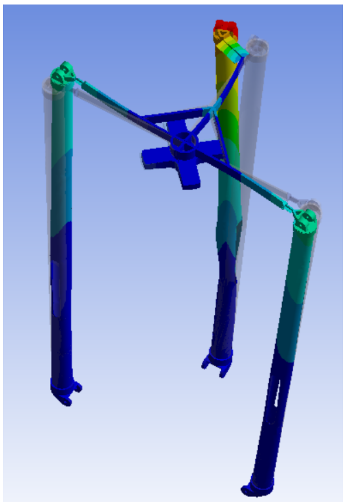

(d) Mode 4

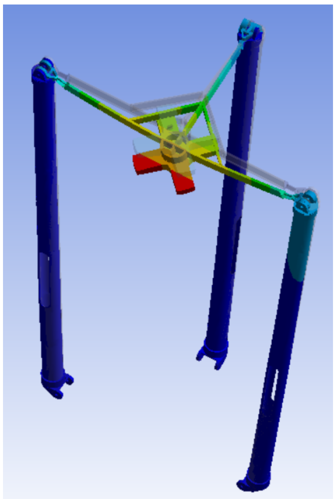

(e) Mode 5

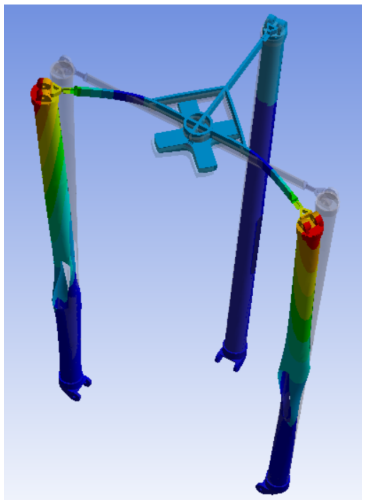

(f) Mode 6

Figure 7.7: Modal shapes of the strain energy concept. Each subfigure is one of the modes of the concept. The frequencies can be found in Table 7.4

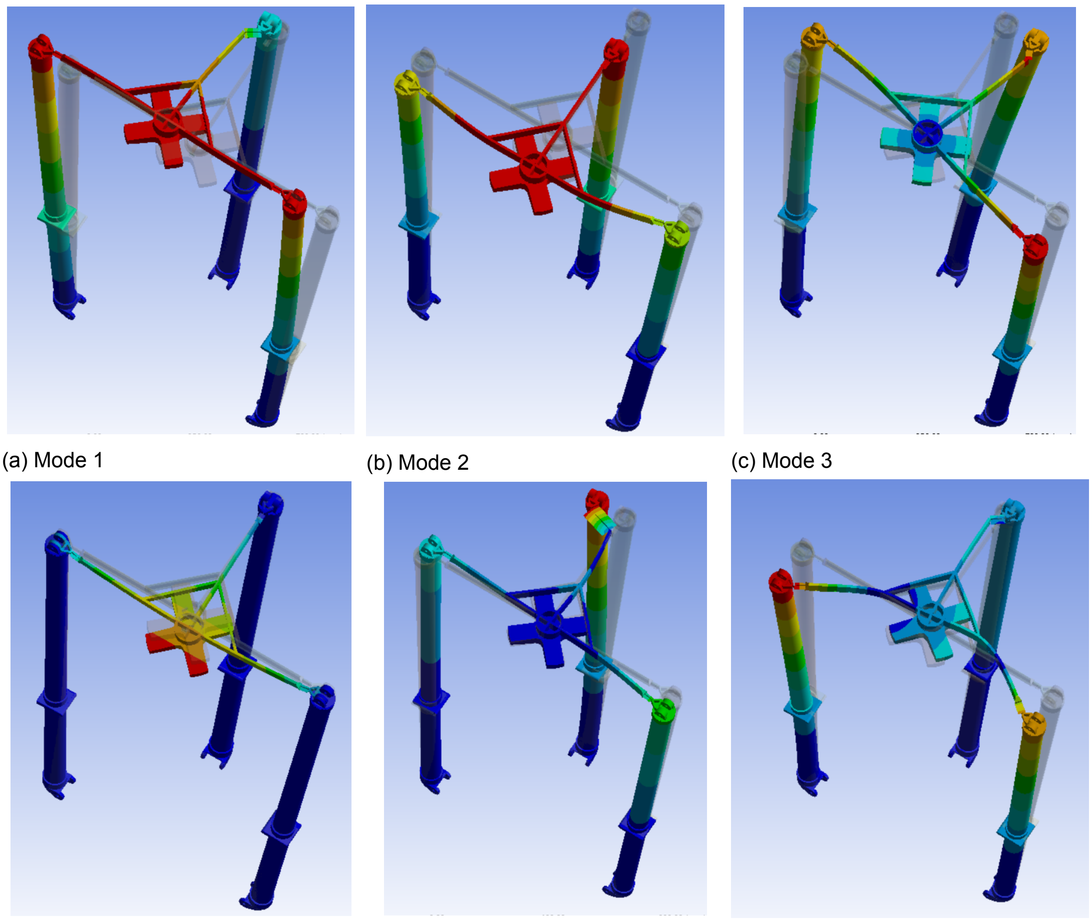

(a) Mode 1 (b) Mode 2 (c) Mode 3

(d) Mode 4 (e) Mode 5 (f) Mode 6

Figure 7.8: Modal shapes of the ball bearing midhinge concept. Each subfigure is one of the modes of the concept. The frequencies can be found in Table 7.4

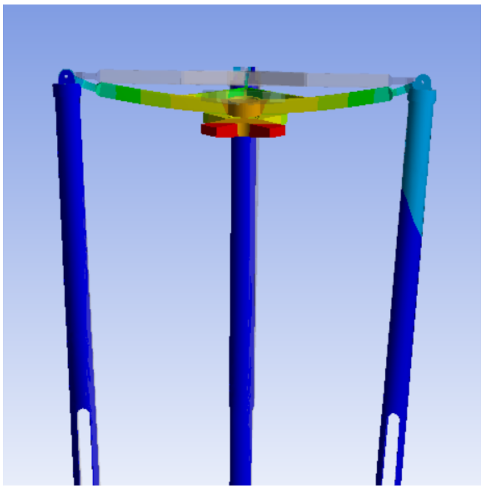

Figure 7.9: Front view of the modal deformations of the strain energy hinge concept for eigenmode 5.

7.4. Mid Hinge Trade-off

In Section 7.2, the trade-off criteria for the mid hinge were discussed. With these criteria, the actual trade-off could be made. The performance of the two concepts for each criteria will first be discussed, after which the trade-off table is given.

7.4.1. Deployment Accuracy

Industry experts in the field of integral slotted hinges believe that the deployment accuracy of 15 micron will not pose a problem, It is believed that it can become a problem when sub micron deployment accuracy is required.
The ball bearing hinges do not have a problem with this criterion, as the hinges of the JWST demonstrates, although the ball bearings can introduce hysteresis and backlash into the system when not designed properly. This means that both hinge types score good on this criterion.

7.4.2. Complexity

The complexity of the strain energy hinge is low during operations, since there are no moving parts involved. All the movement of the hinge is provided by the flexibility of the material. On top of that, the locking is provided by the shape of the boom itself.
The complexity of the ball bearing hinge however is high. It will involve multiple moving parts, together with a locking system for after deployment. This increases the risk of failure during deployment.

7.4.3. Mass

The strain energy hinge concept has has a low mass. The hinge is part of the boom itself, made out of CFRP, without any added parts. This keeps the mass of the system low. The ball bearing mid hinge concept has a higher mass. Since the hinge has to be locked after deployment, the mass increases more.

7.4.4. Thermal behaviour

Since the hinge is part of the boom, there is a continuous thermal connection between the top and bottom of the boom. On top of that, the fibres of the boom and hinge can be made such that the net CTE in the axial direction can be made close to zero. The ball bearing hinge concept does not have a continuous thermal path between the two ends of the boom. The contact area between the hinge halves has to be kept to a minimal for an accurate deployment result. This however increases the thermal resistance over the hinge, making gradients within the boom bigger. The CTE of the hinge depends on the material chosen. When a metal would be chosen, invar would have the lowest CTE with an expansion of about $1.6 \cdot 10^{-6}$ m/mK.

7.4.5. Post deployment stability

The strain energy hinge concept is simple, but due to the cutout in the boom the stiffness of the system is decreased. According to Mr. P. Greff, the stiffness is decrease by about 20%. On top of that, the concept limits the wall thickness of the boom. The ball bearing hinge concept has a stiff link connecting both sides of the boom after deployment. Besides that, the wall thickness of the segments is not limited, increasing the stiffness of the system. This result could also be seen in the results of the modal analysis presented earlier. The ball bearing hinge concept had especially in the first three modes an advantage over the integral slotted hinge concept.

7.4.6. Trade-off Results

From the trade-off in Table 7.5, it can be concluded that the hinge with the most potential is the strain energy hinge. Although the scores of the ball bearing hinge concept and the strain energy hinge concept on thermal behaviour and post deployment stiffness cancel each other, the strain energy hinge concept wins on the lower complexity and mass. The concept selected for the mid hinge is a strain energy hinge, to be more specific the integrated slot hinge.

Table 7.5: Trade-off table for the concept trade-off of the mid hinge concept.

	Weigth	Ball bearing	Strain energy
Accuracy	0.26	5	5
Complexity	0.14	2	4
Mass	0.08	2	5
Thermal behaviour	0.26	3	5
Post deployment stiffness	0.26	4	2
Total		3.56	4.08

7.5. Conclusion

In this chapter, the concept selection of the mid hinge was treated. Three hinge concepts were considered for the trade-off for the mid hinge: ball bearing hinges, integral slotted hinges, and shape memory composite hinges. The shape memory composite hinges deemed not accurate enough, and were discarded from the trade-off. In order to determine the effect of the integral slotted hinge on the boom stiffness, a modal analysis was performed on both remaining concepts. Apart from the mid hinges, the models were kept equal. The results from ANSYS were compared to simplified hand calculations. The results were comparable, but it was also noted that test are required to validate the results, and that a critical attitude towards the results have to be kept. The results of the modal analysis indicated that the ball bearing hinge concept had higher eigenfrequencies. The difference is especially clear in the first eigenmodes. These results were taken into consideration during the trade-off. The result of the trade-off was that the integral slotted hinge concept was selected. The main advantages of the integral slotted hinge over the ball bearing hinge were the thermal properties, the low complexity, and mass of the integral slotted hinge.

8

Effect of Design Parameters on the System Eigenmodes

In the previous chapter, a modal analysis was performed to compare the two concepts considered in the trade-off for the mid hinge. From this analysis, several observations were made. This chapter will elaborate on these observations by checking the effect of changing the dimensions of the system components on the modal response of the system.

8.1. Design Parameters

As stated before, several points of investigation were determined after the first modal analysis. In this section, the points that were considered in the second modal analysis are presented with a small description why it is a point of interest.

- **Four booms.** In Chapter 5 it was decided to decrease the number of booms of the system from four to three booms. One of the concerns of going to three booms was that the system would loose in stiffness, and that the modes would become more complex. With this analysis, the effect of going to three booms will be investigated.
- **Boom wall thickness.** The boom wall thickness has influence on the stiffness of the boom. However, the influence of the wall thickness on the stiffness of the total structure is unknown. This question is interesting, since the currently used concept is restricted in wall thickness.
- **Boom deployment angle.** In the current concept the deployed booms are not parallel. To test the hypothesis that the structure would be stiffer when the booms are not parallel, this case is investigated in this analysis.
- **Width spider.** In Figure 7.7f it can be seen that the spider has a role in the higher eigenmodes of the system. To investigate the effect of the width of the spider to the overall stiffness of the system, it was increased. The results from this analysis will be important in the trade-off between system stiffness and optical performance.
- **Boom diameter.** The boom diameter is an important factor in the design of the boom, as it determines the area moment of inertia of the boom. The diameter is limited due to practical reasons, since a larger diameter might not work with the selected mid hinge. To see the effect of increasing the boom diameter on the system behaviour, a larger boom diameter was used. The results could be helpful for the trade-off between increased boom stiffness and larger development risks of the boom.
- **Locked hinges.** As was explained in the section concerning the mid hinge trade-off, it seems that the top- and root hinges play an important role in the stiffness of the system. For that reason, an analysis is run with locked hinges. This would probably mainly influence the first two modes, together with mode 5 (Figures 7.7a, 7.7b, and 7.9).

- **Flexures.** In the previous analysis, it could be seen that the flexures participate actively in the vibrations. To investigate the effect of the flexures on the stiffness of the system, an analysis has to be performed without flexures build in the system. To be clear, these are the flexure between the spider and the boom. The flexures of the mounting of the secondary mirror are still in place.

The results of these analyses will be given in this chapter. But first, the solid models used will be explained in the next section.

8.2. CAD Models

In this section, the models used for the analysis will be briefly introduced. In order to get a good comparison of the results, each model is only changed on one of the aspects explained before. All the models will be based on the current design iteration, a structure having three booms with integral slotted hinges.

8.2.1. No Flexures

The role of the flexures has to be investigated in order to make a good trade-off between including flexures to make the system exactly constrained or to leave them out to increase the stiffness of the system. In the model, the flexures were removed and the spider was extended to keep the overall shape of the model constant. The interface between the hinge and the spider is not designed, for now it is assumed the components are bonded together. The CAD model is given in Figure 8.1a.

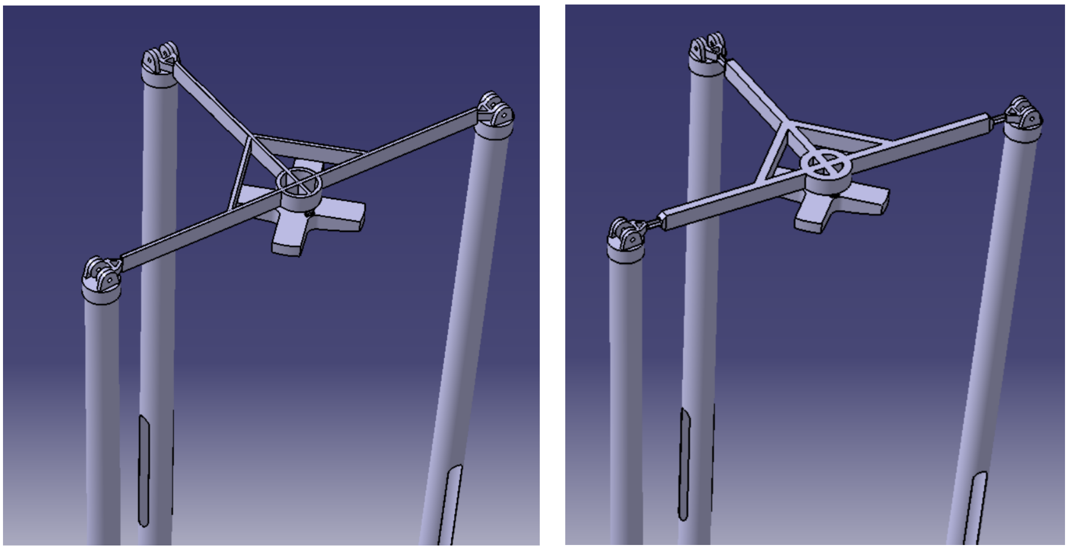

(a) Model without flexures (b) Thick spider model

Figure 8.1: CAD models as used for the modal analysis of the concept without flexures (a) and the thick spider model (b)

8.2.2. Width Spider

In the first modal analysis it was observed that the spider participates in certain modes. The hypothesis is that when increasing the width of the spider, the frequency of this mode will increase. However, the mass of the system will also increase, possibly decreasing the frequency of other modes. In order to test the hypothesis, the spider width was increased from 9 mm to 20 mm, with a wall thickness of 4 mm. This means that part of the spider will be above primary mirror segments. The results of this analysis can provide information useful for the trade-off between the stiffness of the system and the blocking of the primary mirror segments, and thus the optical performance.

8.2.3. Boom Wall Thickness

The model for the boom wall thickness has to be altered in two ways. First of all, thicker walls would not work for the integrated slotted hinge. For this, a model without hinges in the booms is made, while keeping the wall thickness unaltered (0.5 mm). Then, a second model is made with a larger wall thickness. This approach gives also insight in the effect of the hinges in the booms. The CAD model used in these analyses is given in Figure 8.2b. The difference between the two hingeless models is only in the wall thickness of the boom, and cannot be seen from the figure, thus only one of the models is presented here. The wall thickness of the second model was increased from 0.5 mm to 2 mm.

8.2.4. Parallel booms

One of the changes between the previous and current design iteration is that the booms are tilted with reference to each other in the current design iteration. To test the effect of the orientation of the booms, an analysis with parallel booms was performed. The model can be seen in Figure 8.2a.

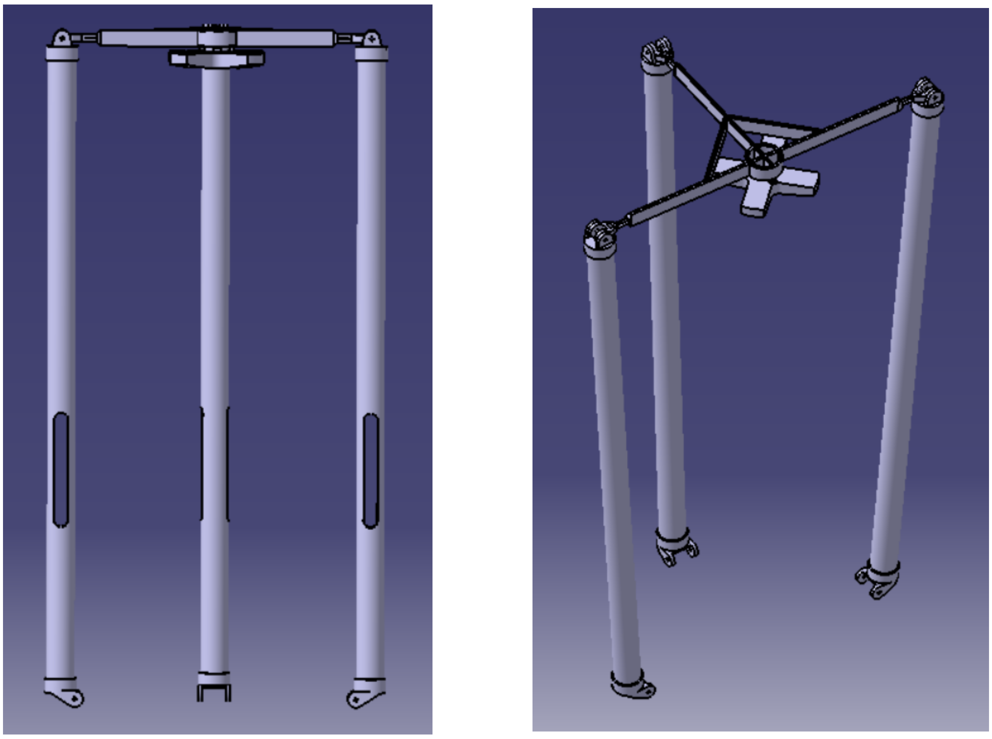

(a) Parallel booms model

(b) Hingeless boom CAD model

Figure 8.2: CAD models used for the case with parallel booms (a) and hingeless (thicker) booms (b).

8.2.5. Locked Hinges

When looking at the modal shapes in Figure 7.7, it can be noted that the hinges play an important role in the movement of the system. The hinges are required for the deployment of the system. After the system is deployed, the only function of the hinges is to keep the system exactly constrained. In ANSYS, all the revolute joints were changed to fixed joints. Since this change is made in the model in ANSYS, no changes had to be made in the solid model itself.

8.2.6. Four Booms

This analysis was performed to see the effect of removing one boom from the design. As stated in Chapter 5, the trade-off between three and four booms had to be revisited when more information was present. In order to be able to add an identical boom, the spider was extended. The CAD model used for this analysis is given in Figure 8.3a.

8.2.7. Larger Boom Radius

An important design parameter is the radius of the booms. The baseline design has a radius of 35 mm. This was based on the discussion with Mr. P. Greff. The hinge SpaceTech produced had a radius of 20 mm, but this could be increased to 30-35 mm without a problem. Since the diameter of the boom determines the inertia of the boom, a radius of 35 mm was chosen. It was said that bigger diameters could be possible, but from a diameter of 100 mm, problems could arise. To see the effect of the boom diameter, a model with a boom diameter of 90 mm was taken. The model was based on the parallel booms concept due to earlier found results. In the results that will explained later, it can be seen that the orientation of the booms is less important than the spider length. The model used is given in Figure 8.3b.

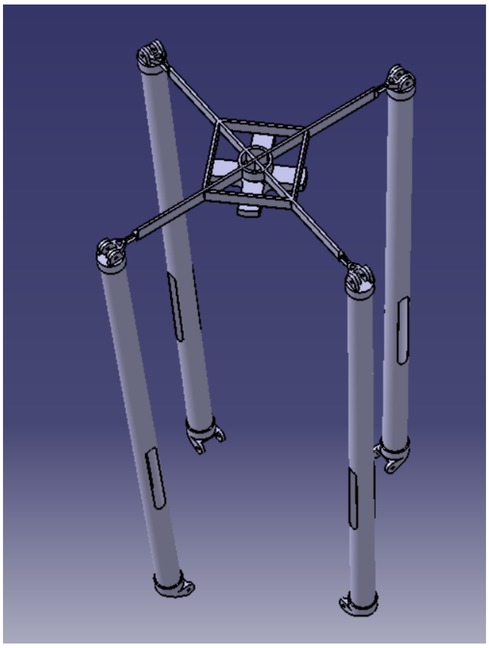

(a) Four booms model

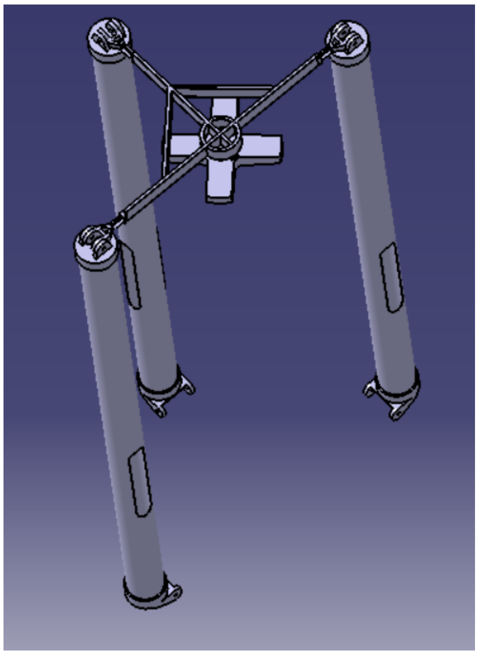

(b) Larger boom radius model

Figure 8.3: The models for the four boom concept and the larger boom radius concept used in the analyses.

8.3. Results

As in the previous analysis, it was performed in the Modal application of ANSYS. The meshes were created in the same manner as in the previous analysis. The root hinges were modelled as body-to-ground revolute joints for two of the hinges, and one body-to-ground fixed joint. The top hinges were modelled as body-to-body revolute joints. The exception is the base model with latched hinges. In this concept, all joints are fixed joints. The results of the analyses are given in Table 8.1.

Table 8.1: Results of the modal analysis for the different design concepts. All frequencies are in Hertz

Concept	Mode 1	Mode 2	Mode 3	Mode 4	Mode 5	Mode 6
Base	4.2	4.3	10.3	22.6	23.1	31.6
Parallel booms	4.3	4.3	10.1	25.2	30.7	47.5
Thick spider	4.0	4.1	9.8	25.6	30.1	52.3
Latched hinges	5.6	6.0	10.3	22.6	31.1	32.6
No flexures	4.5	4.6	14.4	26.2	36.9	37.91
Four booms	3.8	4.0	10.4	22.5	30.8	32.0
Larger boom radius	5.7	5.8	13.4	26.4	30.1	49.4
No boom hinges	4.8	5.1	13.0	23.1	25.2	34.9
No boom hinges, thick boom	7.8	8.1	21.1	23.2	28.4	34.7

From the results given in Table 8.1, several conclusions can be drawn. In the table, Base is the concept as it was after the hinge concepts selection and will form the reference to which each concept will be compared to. The comparison will be done in the sections below.

8.3.1. Parallel Booms

The modal shapes of the parallel system were the same as those of the baseline. Furthermore, in Table 8.1 it can be seen that the frequency of the first three eigenmodes are very close. The influence of the boom orientation is thus very limited to not present. This can be caused by the limited angle obtained due to the limited storing volume. In the higher modes, especially modes 5 and 6, the parallel booms concept has significant higher frequencies. These higher modes are linked to the movement of the spider. Since the legs of the spider are smaller on the parallel boom concept, the eigenfrequency for these modes are higher on the parallel booms concept. The results suggest that the orientation of the booms do not influence the eigenmodes of the system, but due to the change in spider size, the higher eigenmodes have significantly higher eigenfrequencies. It is thus beneficial to have a spider leg size as small as possible.

8.3.2. Thick Spider

The first observation made by looking at the results was that the modal shapes of the system are similar to those of the baseline. Then, comparing the frequencies of these eigenmodes in Table 8.1 it can be seen that the frequency of the thicker spider in the lower modes is lower than the baseline. This can be explained by the fact that these lower modes are dependent on the booms. Since increasing the spider dimensions do not increase the stiffness of the booms, but do increase the mass in the top of the system, the frequency of these modes is lower. In the table, it can also be seen that the frequencies of the higher modes are higher than the baseline, and close to those of the parallel booms concept. It can also be seen from the modal shapes that the modes dependent on the spider stiffness mainly have deflection in the outer parts of the spider, thus after the cross beams. Since the first modes are influenced by the mass of the spider rather than the stiffness, it is important to keep the mass down. When the frequencies of the higher modes need to be increased, this can be done by increasing the outer parts of the legs of the spider, but keep the cross beams and the spider between the cross beams unaltered.

8.3.3. Latched Hinges

The results of the system with latched hinges can be seen in Table 8.1. However, these results can be misleading, since modes 5 and 6 of the locked hinge model are not the same as mode 5 and 6 of the baseline model. It seems that mode 5 of the locked hinge model is similar to mode 6 of the baseline model, and mode 6 of the locked hinge model is similar to mode 5 of the baseline model. The modal shapes of mode 5 and 6 of the locked hinge model are given in Figure 8.4.

Looking at the frequencies of the modes in the table, it can indeed be seen that the locking of the hinges has an effect on modes 1, 2, and 5 of the baseline model. Both modes 1 and 2 have an increase of about 1.5 Hz, while for mode 5 the eigenfrequency was increased from 23.06 Hz to 32.57 Hz, almost 10 Hz higher. In the other modes, the effect of locking the hinges seem negligible.

Comparing the results for the latched hinges model with the hand calculations performed in the previous chapter, it can be concluded that the results are close to the hand calculation considering three booms (see Table 7.3). This means that the increase in eigenfrequency as calculated by ANSYS and by hand when latching the hinges agree with each other.

8.3.4. No Flexures

The modal shapes of the first three modes are very similar to those of the baseline model. There is a difference in the higher order modes though. Due to the increased stiffness in the joint between the spider and the boom, mode 4 of the baseline becomes mode 5 in this design. The higher order modes can be seen in Figure 8.5.

From the results, it can be seen that the effect of the flexures on the two lower order modes is present, but is in the order of 0.3 Hz. For the third mode, the influence is larger, about 4 Hz. The largest influence is in the higher order modes. Modes 4 and 5 are swapped, and the increase in frequency of mode 5 in the baseline is about 3 Hz, where mode 4 in the baseline is increased with about 14 Hz. The last mode investigated in this analysis is increased with about 6 Hz.

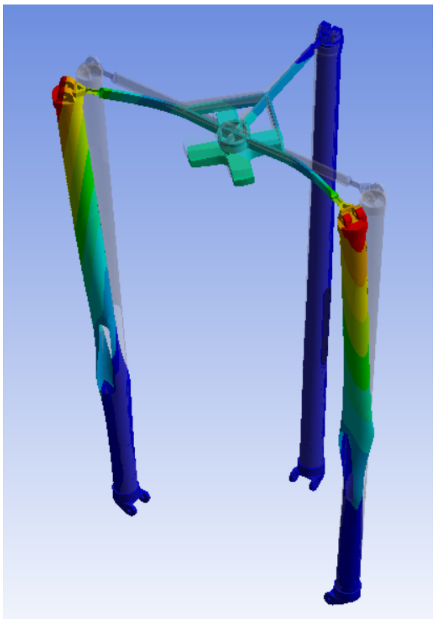

(a) Mode 5

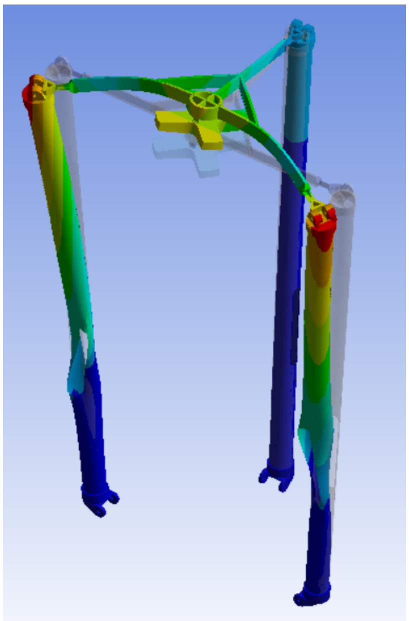

(b) Mode 6

Figure 8.4: The modal shapes of the locked hinge model, mode 5 and mode 6.

The presence of the flexures can thus partially explain the difference between the hand calculations and the ANSYS results, presented both in this chapter as in the previous chapter. Especially in the higher order modes, the effect is visible. Looking only at stiffness, it is better to discard the flexures in the design. However, when they are included, it is important to make them as stiff as possible. Since the flexures are based on the deflection of the spider and the booms, an increase in stiffness of the flexures can be realised by increasing the stiffness of the booms and spider, or by allowing more deformation in these components due to the forces needed to deform the flexures.

8.3.5. Four Booms

Looking at the results in Table 8.1, it can be seen that the four boom option has a lower eigenfrequency than the baseline for the first two modes. The shapes however, are similar. The increase in mass is thus more significant than the possible increase in stiffness of the system. It is also noticed that the first two eigenmodes are not equal, although the system looks symmetrical on first hand. However, the booms are attached to the spider with two different flexure types. One of the types is stiffer than the other type. The difference between the two types is that the first type allows rotation around two axes, while the other type allows the same rotations, but has an additional tranlation DOF. The flexures are given in Figure 6.4 in Chapter 6.

The result was checked with a simple hand calculation. It is noted that the added boom does not necessarily add stiffness to the system due to the fact that it is hinged. The mass of the system is increased to 5.067 kg. The hand calculation gave an eigenfrequency of 4.9 Hz, which is lower than the thee boom option.

The effect on modes 3 and 4 is very small. But due to the extra connection of the spider to the ground, the fifth mode in the base model does not show up in this analysis of the four boom option. It is replaced by a mode which is similar to mode 6 of both models. The three higher order modes of the four boom option is given in Figure 8.6. The results of this analysis suggest that the reduction in stiffness by removing the fourth boom in the previous design iteration is limited.

8.3.6. Larger Boom Radius

Since this model was based on the parallel booms model instead of the baseline model, the comparison should also be made with the parallel boom model results. In Table 8.1, it can be seen that in the three

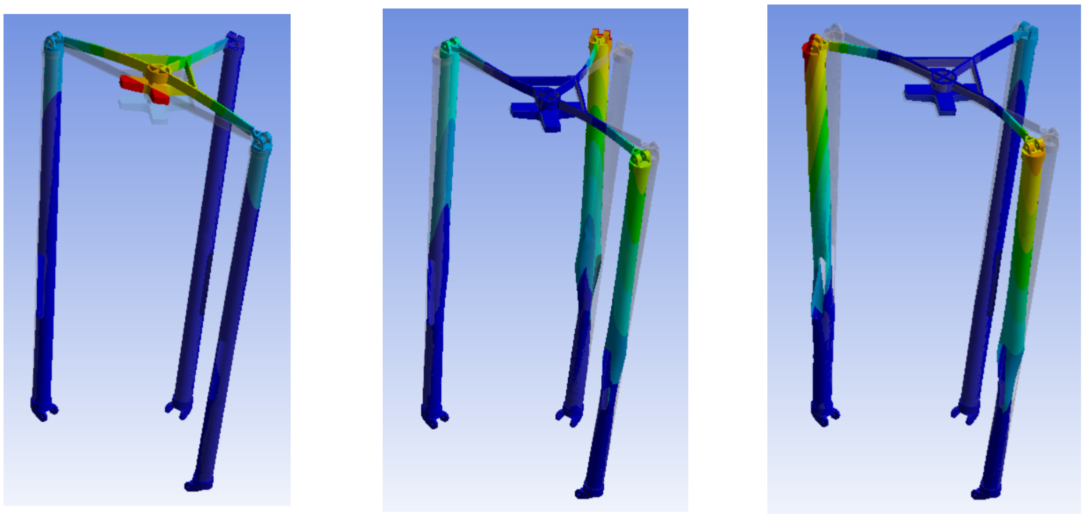

(a) Mode 4 (b) Mode 5 (c) Mode 6

Figure 8.5: The higher order modal shapes of the model without flexures between the spider and the hinges.

lower order modes the larger boom radius results in higher eigenfrequencies. The difference is about 1.5 to 3 Hz. In the higher order modes, the difference is present, but is less significant. The boom radius does influence the stiffness of the system, but due to the limited range of possible boom radii, the difference is limited as well. Since from a production and development point of view the boom with a diameter of 90 mm forms a higher risk, the current diameter of 70 mm is the better choice.

8.3.7. Hingeless Boom

This analysis has two goals. It sets a baseline for the thicker wall concept, since a thicker wall is not possible with the current hinge. The other goal is to verify the simulation for the hinge used. The reduction in stiffness of the boom by the hinge is about 20%. A reduction of about 20% will reduce the eigenfrequency by about 0.89 due to the square root in the equation for eigenfrequency.

From the results given in Table 8.1, it can be seen that indeed the hingeless concept has higher eigenfrequencies than the baseline. When looking at the modal shapes, it can be noted that modes 4 and 5 have swapped, thus mode 4 in the baseline is mode 5 in this analysis. The ratio between the eigenfrequencies for the first four eignenmodes range between 0.79 and 0.89, which indicate that the simulations might be a concervative estimation of the stiffness of the system, especially in the third eigenmode. The ratio at the fourth eigenmode is 0.89. The ratio at the two highest order modes range from 0.9 to 1. This can be explained by noting that these modes do not have only a contribution from the booms, but also from the spider.

8.3.8. Increased Wall Thickness

In order to investigate the effect of increasing the wall thickness of the booms, the thickness was increased to 2 mm. Since this is beyond the maximum thickness of the hinges, a hingeless boom was taken. The results are listed in Table 8.1. From the results, it can be concluded that the modes dominated by the boom properties show a significant increase in eigenfrequency. The effect on the modes 5 and 6 is very small. Although the eigenfrequency increased significantly, it is still below 10 Hz for the first two eigenmodes. The main driving factor for the low eigenfrequencies is a result from the shape of the system.

8.3.9. General Observations

After the previously discussed cases were analysed, a general trend was noted. Looking at all the modal shapes of all cases, it was observed that the difference between all the concepts were limited. The overall shape of the system determines to a great extend the first eigenmodes of the system. The design changes tested in this chapter do influence these first eigenmodes, but the effect is limited. It

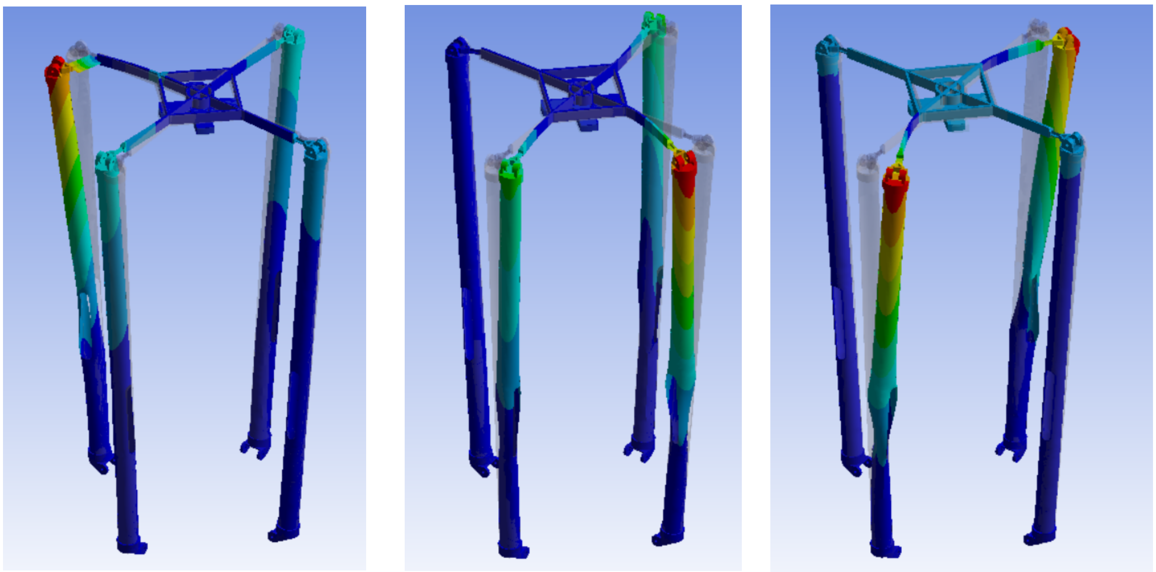

(a) Mode 4 (b) Mode 5 (c) Mode 6

Figure 8.6: Modal shapes of the three higher order modes of the four booms concept.

was also observed that the top of the system, thus the spider and mirror, have a large translation relative to the base. By restricting this motion the eigenfrequencies would increase, and with that the relative motion during vibrations would decrease. An additional solid link between the spider and the instrument bus would be optimal, but since the structure is deployable, this would increase the complexity of the system. Another option is to use cables in tension between the spider and the instrument bus. This will be discussed in more detail in the next Chapter and in Chapter 11.

8.4. Conclusion

In this chapter, the influence of several design parameters on the eigenmodes of the system was investigated. The first conclusion drawn was that the orientation of the booms do not contribute to the stiffness of the system. The length of the spider however does influence the eigenmodes. It is thus more beneficial to decrease the size of the spider. This will result in parallel booms in deployed configuration.

Next, it was seen that the introduction of integral slotted hinges do indeed reduce the stiffness of the booms with about 20%. This is in agreement with what was suggested by SpaceTech which has experience with these hinges, and this can be used as an argument for the verification of the models. However, a full test would give the final validation.

In this chapter, the spider width was also increased. A more stiff spider has mainly effect for the higher eigenmodes. Furthermore, the effect of increasing the boom diameter is present, but this effect is not worth the increase in development cost of the integral slotted hinge.

The main conclusion from this chapter is that the shape of the system determines the eigenmodes. Since the system requires long, small booms with a top mass attached to it, the eigenmodes of the system will be low. The effect of the parameters checked in his chapter is limited.

It was observed that the first eigenmodes of the system have a large translational motion of the spider. It was suggested that this movement could be limited by introducing a wire into the system. This option is discussed in the coming chapter.

9
Design Iteration based on Modal Results

The results of the modal analyses discussed in the previous chapter form the input for the redesign of the SMSS discussed in this chapter. It was concluded that some design parameters had a large influence on the eigenmodes of the system, while others have little effect. In this chapter, the designs of the cable configuration, the spider, the mirror interface, and the flexures will be discussed. In the last section, the conclusions drawn in this chapter are given.

9.1. SMSS Design with Cables

As stated before, the top of the SMSS tends to move relative to the base in the first eigenmodes. Limiting these movements will increase image quality. Adding additional deployable booms to link the spider and the instrument bus would increase the complexity of the system. Another option to reduce the movement of the M2 is to use cables. However, circular cables scatter light. After a discussion with the optical group, it was agreed that ribbons could be used. Ribbons have a square cross section, which is better for the scattering analysis.
For a first design, the ribbons were attached close to the centre of the spider. The ribbons are then attached to the instrument bus at the root hinge. This orientation will form a triangle shape with the spider and the boom. The preload device used to preload the ribbons should be mounted at the root of the system, close to or on the instrument bus. When the preload device would be mounted on the spider, the mass at the tip of the boom would increase, decreasing the eigenfrequencies of the system. In this layout, the ribbons are crossing the M1 segments. However, the M1 segments have a 9 mm gap between them. Thus with a ribbon width less than 9 mm, there will be no interference between the ribbons and the M1 segments. This system layout is given in Figure 9.1.

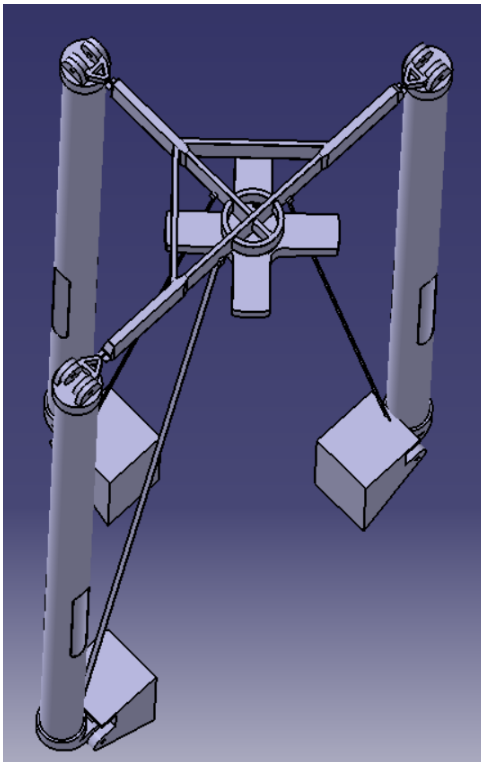

Figure 9.1: The CAD model of the redesign as performed after the results of the modal analyses presented in this chapter. Note that the ribbons intersect the root hinges. This is because the root hinges are not designed in detail yet.

This layout will improve the performance of the system in the first two modes. However, the ribbons will be in the same plane as the spider-boom assembly. This means that the torsional stiffness of the system is not affected. The design of the ribbon is discussed in more detail in Chapter 11.

9.2. Spider

The orientation of the deployed booms was changed to parallel in Chapter 8. This means that the length of the spider can be decreased, which is beneficial for the higher eigenmodes of the system. Apart from that, it was noted that the width of the spider has a large influence on the higher eigenmodes. Discussing this with D. Dolkens, the spider width was increased to 15 mm. This leaves a 2.5 mm margin with the area used for aligning the M1 segments. This increase in width is only applied on the outer parts of the spider. The width of the inner part, between the cross links, is kept at 9 mm. This was done since the cross links and the circle increase the stiffness of the inner part, and a larger width would increase the mass of the system. A further mass reduction was to reduce the wall thickness of the inner part of the spider to 1 mm. The height of the spider was also increased based on the modal results for the higher modes. The height was set to 60 mm in the inner part of the spider. Since the spider is connected to the booms with hinges, the outer parts of the spider do not take up any moments. This means that the height of the spider at the ends can be lower. It was decided to make the ends of the spider 15 mm high, which is increased linearly to 60 mm at the location the cross beams are attached. This tapered design represents the momentum line which is applied to the structure. A render of the new spider is given in Figure 9.2.

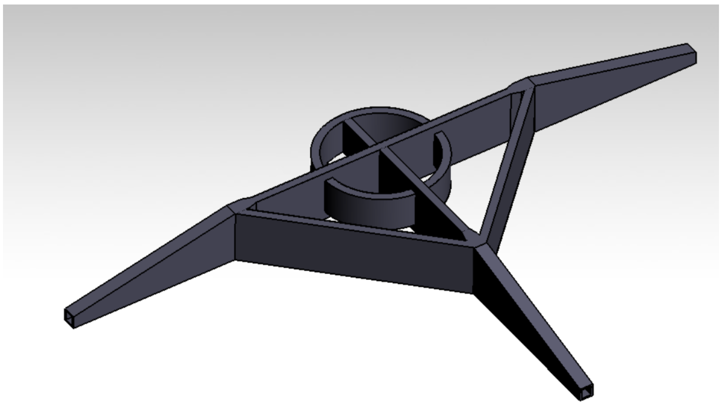

Figure 9.2: Render of the updated spider design.

9.3. Mirror Interface

The focus of the first design of the system was on the design of the mid hinges. For the other subsystems a quick first design was taken to make a first modal analysis possible for the mid hinge trade-off. This is also true for the mirror interface. In this initial design, three blade flexures were used to mount the mirror to the spider. In this section, the design of the mirror interface is discussed in more detail. First the concepts found in literature are discussed below. The concepts taken into account are the following:

- Hard mount
- Clips
- Elastomer
- Bonded
- Kinematic mount
- Flexure mount

9.3.1. Hard Mount

In this type of mount, the mirror is clamped between rigid parts of the mount. A preload is applied to ensure the mirror stays in contact with the mount. The retainer ring has often a loose fit within the inner thread such that it can align itself during tightening. The alignment of the mirror can be provided by precision milled pads within the mount that contact the back of the mirror and pads to provide radial alignment. Another option is to use temporary centering crews to align the mirror radially. After tightening the retainer ring, epoxy is applied through holes in the cell to fix the mirror, after which the centering screws can be removed [68]. Care must be taken that no moment is applied to the mirror, and thus that the preload forces are in line. These two forms are given in Figure 9.3.

The advantage of these mounts is the simplicity. On top of that, the production and assembly of the system do not require special techniques. The disadvantage is that the mount can introduce stress to the mirror during temperature changes [68].

9.3.2. Clips

Another form of mounting the mirror is to use clips that provide a preload force on the mirror. The mirror is pressed against the mounting cell. The axial position of the mirror can be controlled by the back of the mirror mount, at which the mirror is pressed. The radial alignment is done in a similar matter as with the hard mount. This still introduces problems with stress during temperature changes [67]. An example of a mount using clips to provide preload is given in Figure 9.4.

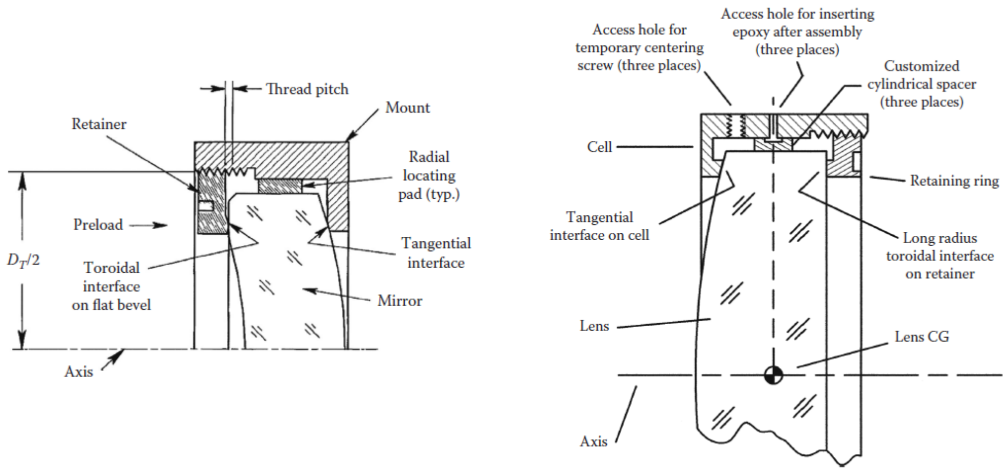

(a)

(b)

Figure 9.3: Two examples of hard mounts used to mount a small mirror. On the left, an example using a tangential mount at the back of the mirror and pads for radial alignment is given. On the right, a mount using radial temporary alignment screws is given. After the mirror is aligned, the mirror is fixed with epoxy, after which the temporary screws are removed. Both images are taken from [68]

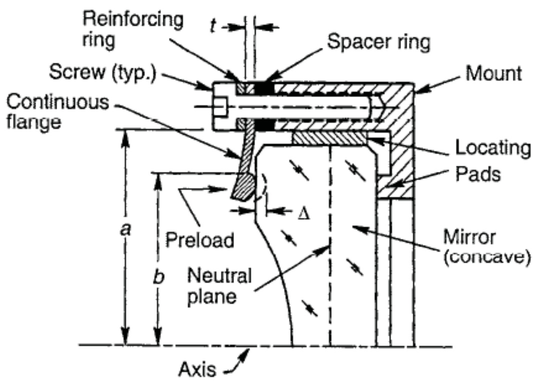

Figure 9.4: Mirror mount using clips to provide preload to the mirror. Image taken from [67].

In order to mount the clips, the mounting cell has to be large and may start to interfere with the light path of the M1 segments. Another option is to extend the mirror back side, which makes the mirror design more complex and may increase the mass of the system.

9.3.3. Elastomer

Both the hard mount and the mount using clips have the problem of thermal stress. A method to decrease the stress in the mirror is by bonding the mirror to the cell with an elastomer. The elastomer fills the gap between the cell and the mirror. The gap can be adjusted such that the overall CTE of the mount equals that of the mirror [67]. An example of an elastomer mount can be seen in Figure 9.5.

Elastomer mounts require a cell larger than the mirror, since the mirror has to fit within the cell. In the current design of the mirror, this might prove a problem due to the non-standard shape of the mirror. Apart from that, the cell might start to interfere with the light path of the M1 segments. Besides that, system athermalisation is more difficult with such a design.

9.3.4. Bonded

The simplest method is to bond the mirror directly to the SMSS. Not the entire back side of the mirror has to be bonded, a small section may suffice. The thermal stress due to difference in CTE of the mir-

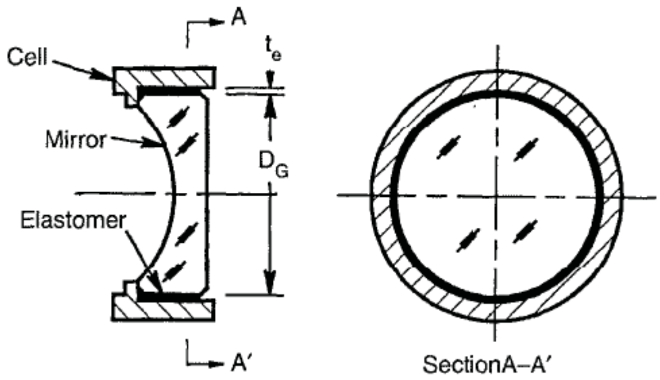

Figure 9.5: Example of an elastomer mount. Image taken from [67].

ror and the SMSS depends on the size of the bonded area [3, 67]. Due to the direct contact between the mirror and the SMSS, athermalisation of the entire system will be more difficult to implement. An example of a bonded mirror is given in Figure 9.6.

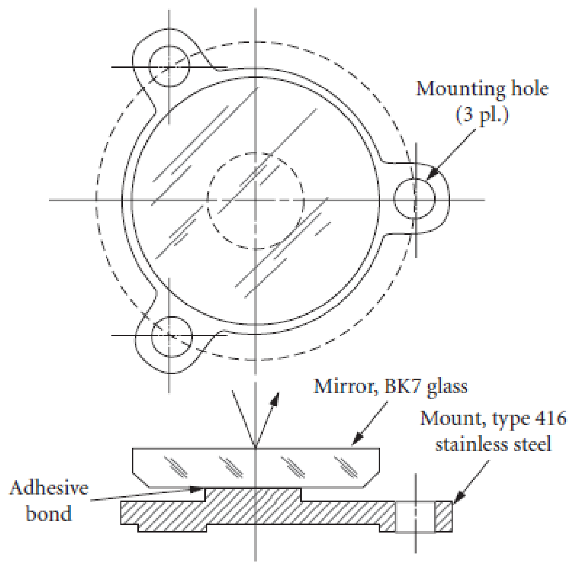

Figure 9.6: Example of a mirror mounted to its support structure by an adhesive. Image taken from [3].

9.3.5. Kinematic Mount

A common method of mounting an optical element without introducing thermal stress into it, is mounting the mirror with a kinematic interface to the support structure. An example of a kinematic mount for an optical element is given in Figure 9.7.

On Earth, normally the gravity is providing the preload. In space this is not possible, and another mechanism has to be used to provide preload. One way is by connecting a spring in the centre of the mirror. Although the mirror mount is made athermal, it is hard to athermalise the entire system with this type of mount. This is due to the fact that the mirror is mounted close to the SMSS.

9.3.6. Flexure Mount

A flexure mount is based on the same principles as the kinematic mount, but now the relative motion is provided by flexing the material instead of letting the components slide over one another. There are

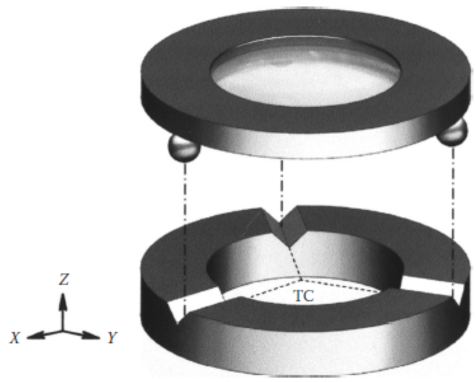

Figure 9.7: Kinematic mount of an optical element. Image taken from [68]

many different forms of flexure mounts, as can be seen in Figure 9.8.

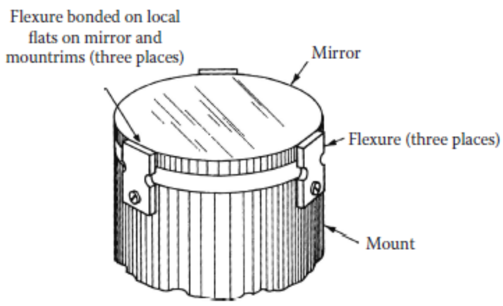

(a) Axial placed flexures. Image taken from [68].

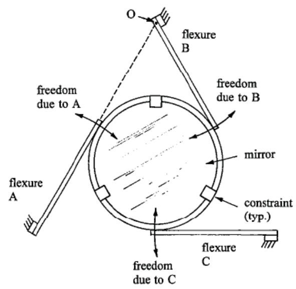

(b) Radially placed flexures. Image taken from [67].

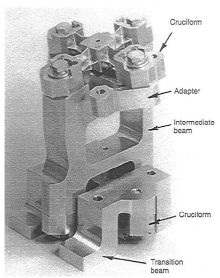

(c) Cascaded flexures. Image taken from [67].

(d) Hexapod configurations. Image taken from [67].

Figure 9.8: Four examples of flexure mounts that can be used in mounting optical elements.

Flexure mounts can be used in different configurations. Besides that, they do not suffer from hysteresis, since the motion is provided by elastic deformation. The flexures can also be mounted on the back side of the mirror, and thus do not interfere with the light path of the M1 segments. Furthermore, due to their length, athermalisation on system level is possible with this option.

9.3.7. Concept Selection

In the previous section, different mounting options were presented. In this section, one is selected for the mounting of the M2 mirror to the SMSS. In Table 9.1 the strengths and weaknesses of the different concepts are summarised. From this table, it becomes clear that if the entire SMSS would be made athermal, the best option for the mirror mount would be the flexure based mirror mount, in particular the hexapod mount. The athermalisation of the system is an important part of the thermal design of the

SMSS. Making the system performance independent of the bulk temperature is given priority. For this reason, the hexapod mount was selected.

Table 9.1: Summary of the strength and weaknesses of the selected mirror mounts

Concept	Strengths	Weaknesses
Hard mount	• Simple design	• Thermal stress • Stress concentration • Large mount diameter • System athermalisation difficult
Clips	• Constant, controllable preload • Accurate placement	• Thermal stress • Large mount diameter • System athermalisation difficult
Elastomer	• Low thermal stress	• Large mount diameter • System athermalisation difficult
Bonded	• Simple method • (low thermal stress) • Compact • low mass	• System athemalisation difficult
Kinematic mount	• accurate mirror placement • No thermal stress	• Stress concentrations • System athermalisation difficult
Flexure mount	• Low thermal stress • System athermalisation possible	• Higher complexity

9.3.8. Interface Design

The length of the interface is an important feature in making the system athermal. The working principle of the athermalisation method used is given in Figure 9.9. All the added length in the interface also has to be added to the booms, since the mirror has to be placed 1600 mm from the primary mirror segments. It is thus beneficial to use a high CTE material. It was chosen to use Aluminium 7075-T6. The reasoning behind this is that aluminium has a high CTE (23.6 micron/m/K), but this alloy also has a high reduced tensile strength, which makes it a usable material for flexures.

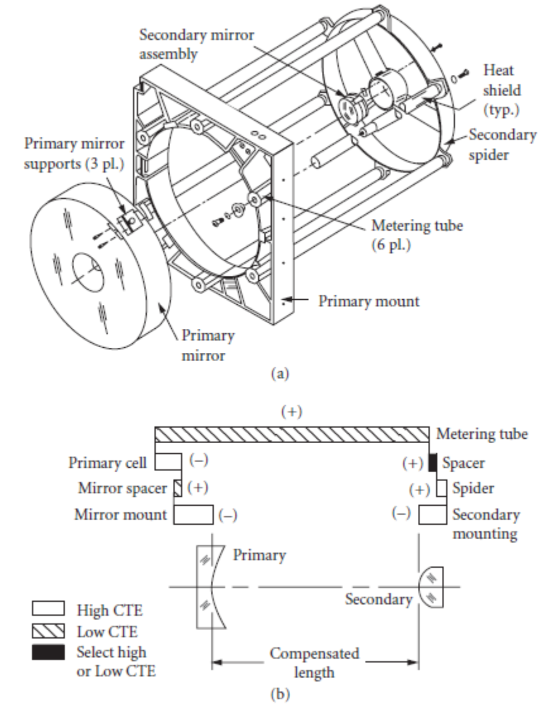

Figure 9.9: Example of the athermalisation method used to make the SMSS an athermal design. Image taken from [3].

The interface thus has to compensate the thermal expansion of the boom. However, the CTE of the boom together with the size of the hinges are still unknown. For a first estimate, the size of the hinges were taken to be 100 mm, and a boom CTE of 0.8. This resulted in a length of 96 mm. This is the design start point.

After the detailed design given in Chapter 10, the length of the titanium parts was known. It was chosen to use the centre line of the root CORE hinge as the point from which the athermalisation is measured. This means that the distance between the centre line and the vertex of the primary mirror segments must be constant over temperature. In Figure 9.10 the system is schematically given. The total length of titanium in the thermal path is 78.15 mm, based on the design of the top and root hinges. The CTE of titanium is 8.6 micron/m/K. The thickness of the mirror is 40 mm, and has a CTE of 4 micron/m/K. It must be noted that in the design, the vertical distance between the attachment points of the interface to the spider and the titanium of the top hinge is about 3 mm, which has the CTE of the CFRP. Y is the length of the mirror interface, while X is the total length of the CFRP. When the system is athermal, the CTE times the length of the components of the boom and titanium parts equals that of the CTE times the length of the mirror interface and the mirror itself:

$$0.8 \cdot X + 8.6 \cdot 78.15 = 23.6 \cdot Y + 4 \cdot 40 \tag{9.1}$$

$$X + 78.15 - Y - 40 = 1725.25 \tag{9.2}$$

With these relations, the required CFRP length and mirror interface length can be determined. The boom length (taken the height of the spider into account) is 1765.7 mm, and the interface length is 81.7 mm.

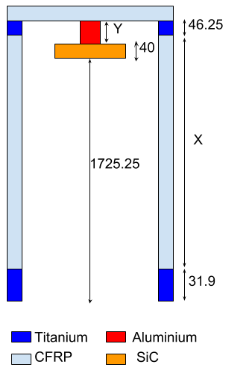

Figure 9.10: Schematic representation of the SMSS with the dimensions used for the athermalisation of the system.

The struts of the hexapod have to constrain one DOF each. If a simple rod would be taken, it means that the diameter of the rod must be small to ensure that the bending stiffness of the rod is not too high. This will limit the buckling load the rod can take. One option is to increase the diameter of the rod, and create cutouts in this rod to ensure the overall bending stiffness of the rods are not too high. The effect of the flexures in the rods is then a bit similar to a universal joint in shafts.

A design was made using a blade thickness of 0.8 mm. The design has to be tested for launch conditions and thermal deflection. The design is given in Figure 9.11.

Figure 9.11: Render of the mirror interface

The next step is to check if the interface can withstand the load cases it will be subjected to. First thermal deflection is considered. Silicon carbide has a CTE of 4. During LEOP, the SMSS will be exposed to the most extreme thermal environment, since the baffle will still be stowed, and thus cannot shield the SMSS. As explained in Chapter 4 the SMSS will be exposed to temperatures of around 180 to 411 K. This is a maximum difference of 123 K, or 148 K with the applied margin (see Chapter 4). The thermal stress induced in the interface is determined by the difference between the CTE of the spider (CFRP) and the mirror (SiC). CFRP has a different CTE in different directions, depending on the layup of the material. The CTE of CFRP can go up to 25 micron/m/K in the direction perpendicular to the fibres [19]. This would result in a difference of 20 micron/m/K. With a temperature difference of 148 K and a mount radius of 69 mm, this results in a difference in expansion of about 200 micron. ANSYS was used to check if this deformation would impose high stresses on the rods. The result can be found in Figure 9.12.

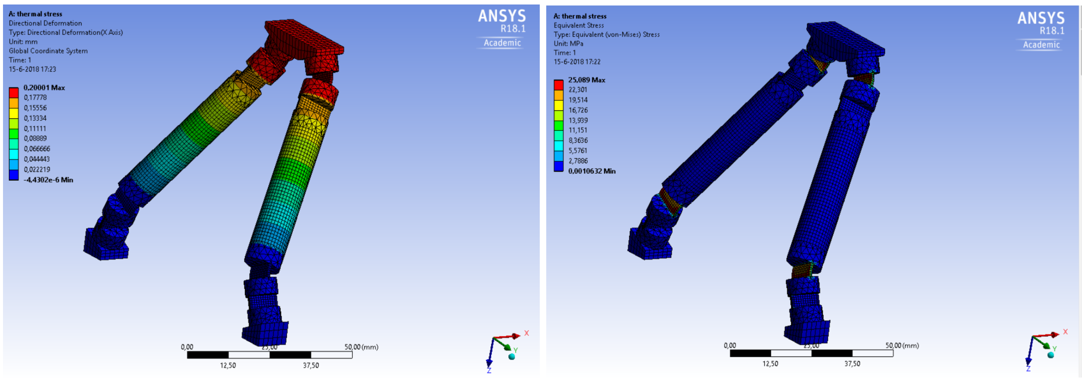

(a) Deformation (b) Von Mises stress

Figure 9.12: Deformations and the von Mises stress on the mirror interface resulting from differential thermal expansion of the mirror and the spider

From Figure 9.12a, it can be seen that the design of the hexapod deformed as expected. From Figure 9.12b, it can be seen that the maximum stress within the rods is around 25 MPa, which is far below the yield stress of the material. The reaction force of the fixed support was about 1.8 N.

During launch, the mirror interface has to hold the mirror in place. ANSYS was used to simulate the effect of the launch on the mirror interface. The loads used were 30 G in the (x+y), (y+z), (x+z) directions. The deformations under these loads can be seen in Figure 9.13.

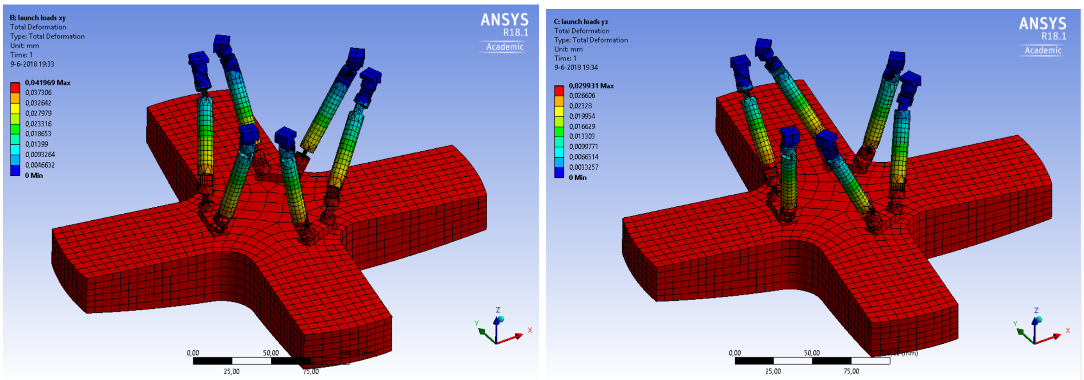

(a) X+Y (b) Y+Z

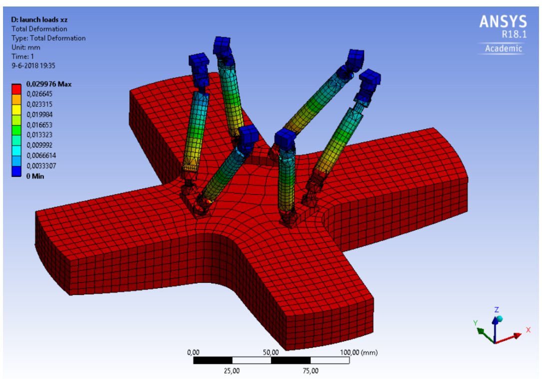

(c) X+Z

Figure 9.13: Deformations of the mirror interface under the applied launch load of 30 G in the (X+Y),(Y+Z), and (X+Z) direction.

The stress due to the applied load during launch is given in Figure 9.14. From the figures, it can be concluded that the maximum stress within the rods is 61 MPa, again well below the yield strength of the used material. It can thus be concluded that the mirror interface can withstand both the launch and LEOP while making the SMSS athermal.

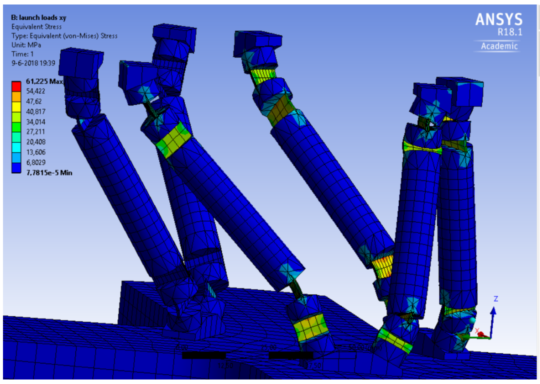

(a) X+Y

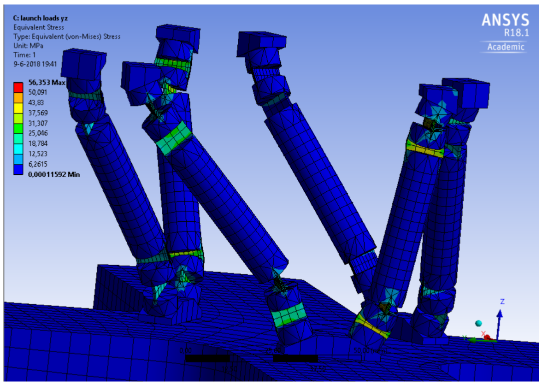

(b) Y+Z

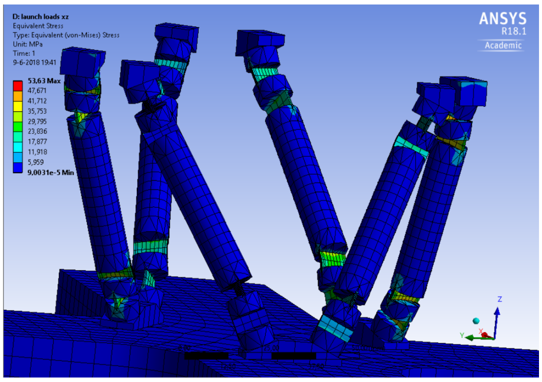

(c) X+Z

Figure 9.14: Von Mises stress in the mirror interface under the applied launch load of 30 G in the (X+Y),(Y+Z), and (X+Z) direction.

9.4. Flexures

The flexures between the top hinges and the spider are added to release degrees of freedom. By doing that, the system is prevented from being overconstrained. This statement is true when treating the booms as stiff members. However, as is visible from the modal analyses presented in Chapter 8 the booms are not stiff members.

The flexure dimensions were based on the deflection of the spider, and with that, the dimensions of the spider. The bending stiffness of the spider is around 8000 N/m, while the boom bending stiffness is around 296 N/m. As can be seen, there is a difference of one order of magnitude between the bending stiffness of the boom and the spider. The booms itself are thus acting as flexures, introducing compliance in the system. It is thus not necessary to include extra flexures to the system. In the new design the flexures will be excluded.

9.5. Conclusion

In this chapter, the redesign of the system was presented. The redesign was performed based on the results obtained in the modal analysis performed in Chapter 8. The legs of the spider were shortened based on the results obtained in the modal analyses. This will both decrease the mass of the system, but also increases the stiffness of the spider itself. Furthermore, the width of the outer parts of the legs of the spider was increased to 15 mm. Another modification was to increase the height of the spider, while making the outer parts of the legs of the spider tapered.
In the previous chapter, it was suggested to include cables in the system. After a discussion with D. Dolkens it was decided that ribbons would be a better option. By taking a ribbon width of 9 mm, the ribbon will fit in the gap between the primary mirror segments, and the ribbon can be connected to

the centre of the spider. This concept can reduce the translational motion of the spider, but not the rotational motion. This is due to the fact that the ribbon, boom, and spider are in the same plane.
The mirror interface was designed in more detail in this chapter. A hexapod structure with flexured rods was selected after different options were considered. This configuration allowed the SMSS to be made athermal. The flexures were introduced in the rods to ensure the rods can only provide one constraint, while still being able to take the required launch loads.
The newly designed interface was simulated in ANSYS, where it was proven that the structure will not fail during launch and LEOP.
In the last section, the flexures between the top hinges and spider were discussed. Based on the renewed design and the results from the modal analyses in the previous chapters, the flexures were removed from the design.

After this design iteration, the root and top hinges can be designed in detail. This will be presented in the next chapter.

10

Top & Root Hinge Detailed Design

In Chapter 6, the preliminary top hinge concept was selected. This first conceptual design was used in the trade-off for the mid hinge. In this chapter, both the top and the root hinges will be designed in detail. First, the hinge concepts will be discussed. These concepts are one step more detailed than what was performed in Chapter 6. After the type of hinges for the top and root hinges are selected, the detailed design of both hinges is discussed. The last section will conclude on this chapter.

10.1. Hinge Concepts

During the first design iteration in Chapter 6 it was chosen for the top hinges to use a single DOF revolute joint in combination with small rotation flexures. in the previous Chapter however, it was concluded that the booms would provide the required degrees of freedom themselves, rendering the flexures useless. This only leaves the revolute joints to be designed. In Chapter 7, the integral slotted hinge concept was selected. This hinge will provide the required deployment torque to the system, and thus the top and root hinges do not have to deliver a deployment torque. The exact concept for this revolute joint was not decided upon yet. This will be done in this section, where four types of hinges are considered:

- Ball bearing hinges
- Integral slotted hinges
- Large deflection flexures
- CORE hinges

In the following sections the concepts will be briefly discussed. It must be stated that the same concepts are considered for the top and root hinges, but different concepts can be selected for the top and root hinges.

10.1.1. Ball Bearing Hinges

Ball bearings are very often used in systems where relative rotation between parts is required. Since they are so often used, a lot of knowledge about ball bearing hinges is available, and a lot of variants are readily available. However, in precision applications, only two variants are suitable. These variants are angular contact bearings and single row radial bearings [64]. The two types of bearings are given in Figure 10.1. As can be seen in the figure, the single row radial ball bearings have shoulders on both sides of the balls, making it possible for this type of bearings to take up load in both radial as axial direction. Angular contact ball bearings on the other hand have shoulders on only one side of the race, which limits the ability of the bearing to take up axial loads in only one direction [64]. Due to the production methods of single-row radial and angular contact ball bearings, there is a difference in the radial load the bearings can take. The number of balls in a radial bearing is less than that of an angular contact bearing [64]. The number of balls in the bearing determines both the maximum load the bearing can take, and the stiffness of the assembly. Since the system has to survive the launch loads, and stiffness of the system is important, angular contact ball bearings are seen as most suited

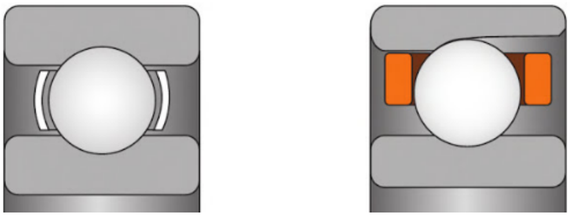

Figure 10.1: Schematic drawing of a single row radial ball bearing (left) and an angular contact ball bearing (right). Image taken from [64]

for this application.

The stiffness of an assembly with angular contact ball bearings depends on the way the bearings are installed. There are two ways to install angular contact ball bearings, see Figure 10.2. The point at which the line of contact between the balls and the races cross the bearing axis is the effective location of the bearing. In the face-to-face configuration, the effective locations of the bearings are closer to each other, resulting in lower stiffness. In the back-to-back configuration this is the opposite, the two effective locations of the bearings are further apart, and thus the static stiffness is higher [64]. Apart from the installation, also the ball size determine the performance of the bearings. By using smaller balls, more balls can be installed, which is beneficial for the stiffness of the system. Smaller balls also result in a less conforming contact with the race, reducing hysteresis, although hysteresis will remain a problem with this type of hinges [64].

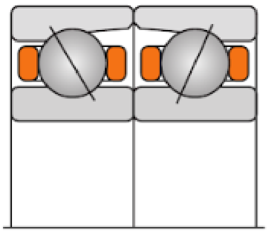

(a) Face-to-face configuration

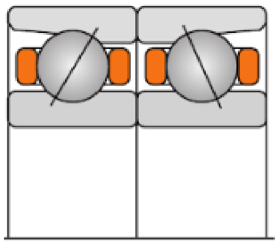

(b) Back-to-back configuration

Figure 10.2: Two configurations for mounting angular contact bearings. The images are taken from [64].

For this concept, a first CAD model was made. It has two angular contact ball bearings in the back-to-back configuration. The preload is applied with a standard locking hinge from SKF. Figure 10.3 gives a view of the CAD model of the top hinge with ball bearings. The bearings in the design are deep groove ball bearings of the type 61900, downloaded from the SKF website [57]. The locking nut in the model is based on the dimensions of the KM 0 lock nut from SKF [57]. The lock washer in the design was downloaded from the SKF website [57]. The lock washer is of the type MB 0.

10.1.2. Integral Slotted Hinges

The integral slotted hinges are already used in the mid hinges. It is also an option to use this type of hinge in the other hinges. The benefit of using this hinge is that the hinge type has a very low hysteresis. However, by using this type of hinge, the system will become overconstrained, and the booms might deform when deployed.

The top hinge has the same orientation in stowed configuration as in deployed configuration. This means that during deployment, the hinge will rotate over roughly 30 degrees and back to its starting position. Since the integral slotted hinge is a self locking hinge, it means that the hinge starts in locked position, then has to rotate, and return in the locked position. This would require a high torque during deployment, more than the mid hinges can deliver. It was tried to change the orientation such, that the

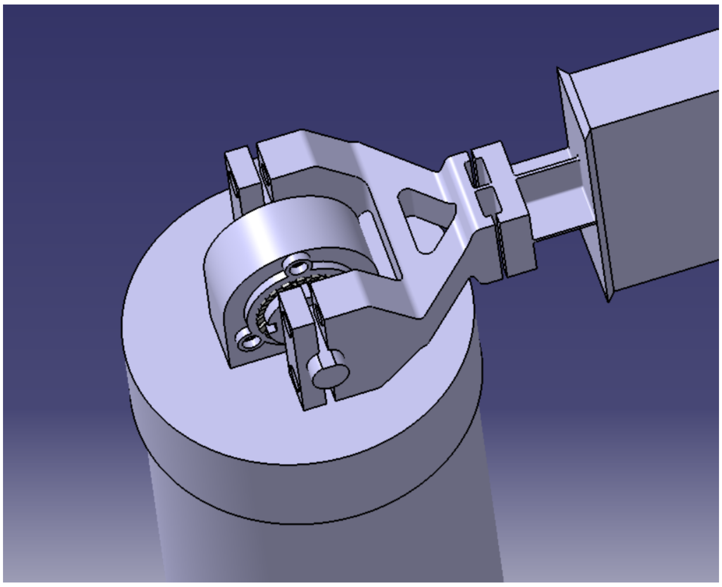

Figure 10.3: CAD model of the top hinge concept using ball bearing hinges. The bearings (61900) and lock washer (MB 0) models were downloaded from the SKF website, while the lock nut was based on the design of the KM 0 lock nut from SKF [57].

starting and final position are not the same, but this was unsuccessful. This means that the integral slotted hinge is not an option for the top hinge. For the root hinge however, it is still an option.

10.1.3. Large Deflection Flexures

Flexures are commonly used to allow for small rotations. The top hinges have to rotate over an angle of around 30 degrees during deployment. There are flexures optimised for high deflection angles, as presented in [32, 66]. One of the examples is the butterfly flexure, given in Figure 10.4.

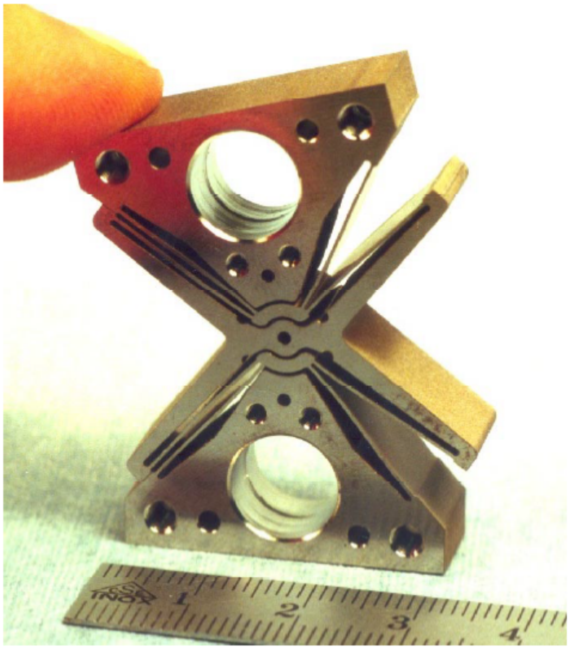

Figure 10.4: Butterfly flexure optimised to allow rotations over a large angle. Image taken from [31].

This flexure has a deflection range of ± 20 degrees [32, 66]. Although the range is in the same order of magnitude as the required range of the top hinge, the flexure hinge concept has a large disadvantage. The flexure hinge requires a moment to bend the material elastically. The required torque for deployment of several concept flexure hinges with a deployment range of ± 20 degrees is for all concepts around 1.5 Nm [66]. However, the deployment torque of the integral slotted hinges used in the booms is an order of magnitude lower, around 0.1 Nm [44, 49]. Thus if the flexure hinges are used, additional deployment actuators are required. This is added to the need of a flexure design that can rotate over 30 degrees while supporting the spider during launch conditions. The launch conditions could pose a possible problem. According to [31], the butterfly flexure with a range tested for ± 20 degrees rotation failed during a vibration test with lower accelerations than those encountered during launch. This would mean that the structure has to be supported during launch to ensure the survival of the flexure hinges. For the root hinges, this concept is not a real option. The root hinge has to rotate over 180 degrees, which is not feasible for this concept.

10.1.4. CORE Hinges

One of the disadvantages of flexures is that they are limited in the load they can take in other directions than pure tension. The CORE hinges were developed to take the advantages of flexures, without the disadvantages of the limited load carrying capabilities in other directions. CORE stands for COmplient Rolling-contact Element . The concept is basically two cylinders rolling over each other, kept in place by thin strips. This way, the minimal bend radius of the strips is always the radius of the cylinders and the cylinders take up the load in compression. With the correct amount of preload, the cylinders cannot slip, and the motion is a pure rolling motion. This mean that the hysteresis is low, no lubrication is needed, and when designed correctly, there is no holding torque present that needs to be overcome. An example of a CORE hinge is given in Figure 10.5.

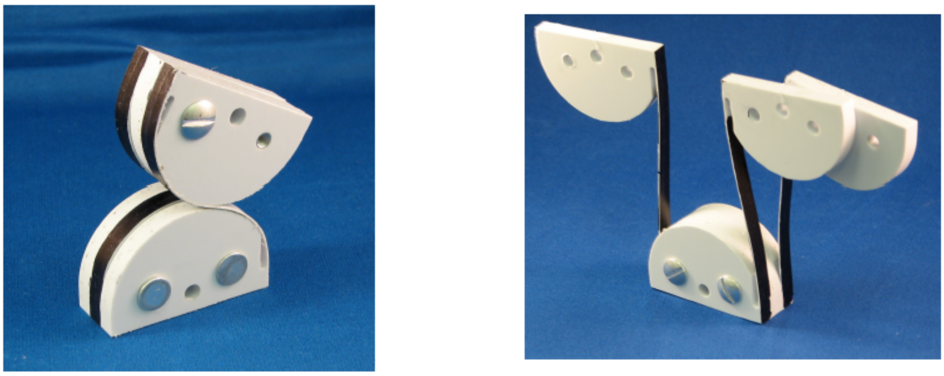

(a) Assembled

(b) Before assembling

Figure 10.5: Example of a CORE hinge. In figure a), the CORE hinge is assembled, while at b) the hinge is not assembled yet. Both images are taken from [28].

10.1.5. Trade-off

Table 10.1 gives an overview of the strength and weaknesses of the different hinge concepts. With this overview in mind, a trade-off for each hinge can be made using a graphical trade-off table. The trade-off table for the top hinges is given in Table 10.2. As can be seen, the integral slotted hinge cannot be used for the top hinge due to the high deployment torque needed to get the hinge out of the latched position. It can be seen that the two best concepts are the ball bearing hinge and the CORE hinge. The CORE hinge scores much better on the hysteresis, while the ball bearing hinge development time is lower. From the trade-off it can be concluded that the CORE hinge concept is the best option for the top hinge.

In Table 10.3 the trade-off table for the root hinge is given. Due to the common requirements on the top and root hinges, the trade-off tables given in Tables 10.2 and 10.3 look similar. There are some differences however. Since the required deployment angle of the root hinge is larger, 180 degrees, this criterion was added to the trade-off. The large deflection flexure hinge scores bad on this criterion, since the largest deflection angle found in literature was only 20 degrees [31]. Unlike the top hinge, the integral slotted root hinge is in stowed configuration not in latched position, and thus the hinge does not need an external deployment torque to deploy. From the trade-off table, it can be concluded that the

Table 10.1: Strengths and weaknesses of the different concepts for the top hinge.

Concept	Strengths	Weaknesses
Ball bearing hinge	• Widely used • No holding torque • High stiffness	• Hysteresis • Requires lubrication
Integral slotted hinge	• Low/no hysteresis • lightweight • Already used • No lubrication needed	• High holding torque
Large deflection flexures	• Low/no hysteresis • No lubrication needed	• Low stiffness • Long development time • High holding torque
CORE hinge	• Low/no hysteresis • No holding torque • High stiffness • no lubrication needed	• Larger dimensions

CORE concept is the best option for the root hinge. Just like with the top hinge, the good hysteresis behaviour of the CORE hinge proves to be decisive in the trade-off between the ball bearing hinge and the CORE hinge. Due to the larger stiffness of the hinge in the other DOF than the rotation over the rotation axis of the CORE hinge compared to the integral slotted hinge in stowed configuration, the CORE hinge was seen as the better option for the root hinge.

Table 10.2: Trade-off table for the top hinge concept.

Concept	Hysteresis	Development time	Hinge stiffness	Holding torque
Ball bearing hinge	Yellow: Sliding contacts within bearings	Green: Widely used	Green: Stiff link	Green: Neutrally stable
Integral slotted hinge	Green: Elastic deformation	Blue: Already used in system	Blue: Reduced stiffness boom	Red: Latched before deployment
Large deflection flexures	Green: Elastic deformation	Yellow: Problem specific design	Yellow: Low stiffness other than tension	Yellow: Single stable point
CORE hinge	Green: Elastic deformation, pure rolling	Blue: Low complexity concept	Green: High stiffness	Green: Neutrally stable

Green: Excellent; Yellow: Sufficient; Blue: Good; Red: Unacceptable

Table 10.3: Trade-off table for the root hinge.

Concept	Hysteresis	Development time	Hinge stiffness	Holding torque	Rotation angle
Ball bearing hinge	Yellow: Sliding contacts within bearings	Green: Widely used	Green: Stiff link	Green: Neutrally stable	Green: No limitation
Integral slotted hinge	Green: Elastic deformation	Blue: Already used in system	Blue: Reduced stiffness boom	Green: Deployment torque	Green: No limitation
Large deflection flexures	Green: Elastic deformation	Yellow: Problem specific design	Yellow: Low stiffness other than tension	Yellow: Single stable point	Red: Limited range
CORE hinge	Green: Elastic deformation, pure rolling	Blue: Low complexity concept	Green: High stiffness	Green: Neutrally stable	Green: No limitation

Green: Excellent; Yellow: Sufficient; Blue: Good; Red: Unacceptable

10.2. Detailed Design

In the previous section, the trade-off was performed for both the top and the root hinges of the system. In this section, the detailed design of these hinges will be discussed. Since the top and root hinges will use the same concepts and are subjected to the same loads, it was decided to design the hinges the same time. Only where the design will start to differ, the two hinges are designed separately. The design procedure is as follows. First, the CORE concept is selected. After that, the material of the strips connecting the two cams to each other will be selected. With these inputs, the components of the hinges (strips and the cams) will be designed using a grid optimisation. When the general design parameters are known, the preload device of the strips will be selected and the compressive stress within the cams are calculated. In the last section, the found design parameters are translated into a 3D design for both the top and the root hinge.

10.2.1. CORE concepts

Within the concept of the CORE hinge, two subcatagories are present. The difference lies in the way the rolling surfaces are contacting. In the first option, the cams are simple cylinders. The strips are wrapped around the cylinders, and the cylinders are rolling over the strips without contacting the other cylinder [33, 35, 37, 50, 51]. In the second option the cams are contacting each other, held together by the strips that are rolling over smaller diameter parts of the cams. The preload pulls the two cams onto each other [28, 29]. In Figure 10.6a the two concepts are presented schematically. In Figure10.6b the Free Body Diagrams (FBD) are given. From this figure, it can be concluded that the two cams in the first concept are not pressed against each other, there is no preload between the two cams. This means that when the two cams are pulled apart, the strips will deform to counteract the pulling force. This means that a small gap between the two cams is created. In the second concept, the strips leave the cams under an angle. Due to the symmetry of the CORE design, the three strips cancel each others side force, but not their axial force. When the strips are preloaded, there will be a normal contact force between the two cams. When a pulling force is applied to the cams smaller than the normal force, the cams remain in contact.

During launch, the cams in the first concept can start to separate. When the load is removed, or the direction of the load is changed, the two cams can collide with each other, damaging the hinge. The second concept, if proper preload is applied, this will not be the case. Due to this, the second concept is selected. The downside of the second option is though that components of the same material are touching each other, which might lead to cold welding.

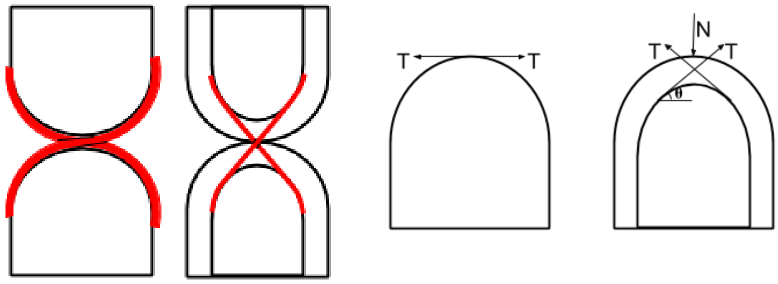

(b)

(a)

Figure 10.6: Schematic representation of the two versions of the CORE hinge. on the left, the CORE with a constant radius. On the right, the CORE with different radii for the flexures and the contacting surfaces. The free body diagrams of the lower halves of both types are given on the bottom of the figure.

10.2.2. Strip Material

The materials considered are listed in Table 10.4. Aluminium 7075-T6 was the chosen aluminium alloy for its high yield strength compared to other aluminium alloys. The choice for stainless steel 301 CR was based on [50], where this alloy was used as flexures for a CORE hinge. Ti-6Al-4V is a used material for flexures [22, 31]. Invar was added due to its low CTE. The last material listed is Kevlar. This fibre material was used in [28] and is also often used in space. One example is the debris shield in the Columbus module [12].

According to [63] the reduced tensile modulus is an important material property for flexures. The reduced tensile modulus is the ratio of the yield strength over the tensile (Young's) modulus. This can

Table 10.4: Material properties of selected materials

Material	**Young's modulus [GPa]**	**Yield strength [MPa]**	**Young's modulus / yield strength [-]**	**Density [kg/m^3]**	**CTE [10^{-6} m/m/K]**
Aluminium 7075-T6 [8]	71	505	0.0071	2800	23.4
Stainless steel 301 CR [50]	197	1138	0.0057	7800	17
Titanium Ti-Al-4V (solution heat treated and aged) [8]	114	1103	0.0097	4430	8.6
Invar [8]	141	276	0.0019	8050	1.6
Kevlar®[12, 20]	70-175	2300 - 4200[1]	N/A	1439	-4 - -4.9

[1] For Kevlar® ultimate strength is used instead of yield strength.

also be seen in the equation for the bending stress developed within the strips of a CORE hinge[50]:

$$\sigma_{bend} = \frac{E_{strip} \cdot t}{2R} \tag{10.1}$$

Where E_{flex} is the Young's modulus of the material of the strip, t is the thickness of the strip, and R is the radius of curvature of the cylindrical parts of the hinge, and thus the bending radius of the strips. Rearranging this equation and taking the yield stress of the material as bending stress leads to:

$$\frac{\sigma_{yield}}{E_{strip}} = \frac{t}{2R} \tag{10.2}$$

Thus for a high reduced tensile modulus, the thickness of the strips can be bigger, or a smaller radius can be used for the cams. By increasing the thickness of the strips, the stress in the strips due to the loads other than the bending load will be lower, since the cross sectional area of the strips is increased. For this reason it is beneficial to choose a material with a high reduced tensile modulus for the flexures. Looking at Table 10.4, it can be seen that Titanium Ti-6Al-4V has the highest reduced tensile modulus of the metals. Titanium would thus be the best choice considering only the metals. For Kevlar®, the reduced tensile modulus is less important since it is a fabric. Another noteworthy property is the CTE, which is negative. This can introduce problems under thermal loading, since the cams will have a positve CTE. More about the effect of the temperature will follow in the following sections. For now, it is chosen to use titanium as material for the strips.

10.2.3. Component Sizing

Now the concept and the strip material are known, the components can be designed in detail. The approach to this is as follows. Three selected design parameters are optimised using a simple grid search based on the stress equations given in this section. With these design parameters the cams are designed, after which the contact stress and surface treatments are discussed.

Design Parameters

The design will be based on several parameters. These parameters are selected based on the stress state within the strips. The stress state within the strips will be given first.

It was seen that forces perpendicular to the rotation axis are all transferred to tensile forces in the flexures. Only the forces parallel to the rotation axis will develop a shear force. The total tensile stress within the strips is given below:

$$\sigma_{t,tot} = \sigma_{bend} + \sigma_{thermal} + \sigma_{launch} + \sigma_{preload} \tag{10.3}$$

The different forms will be discussed in the paragraphs below.

Thermal stress The thermal stress depends on the difference in CTE of the core and strips, the temperature difference, and the strip material:

$$\sigma_{thermal} = \left(CTE_{cam} - CTE_{strip}\right) \cdot \Delta T \cdot E_{strip} \tag{10.4}$$

As can be seen, the thermal stress in the equation can become negative. When this happens, it means that the two cams can separate since no normal force is present to keep them in place. By applying a preload, it can be prevented that there will be play between the components within a certain temperature range. Another observation is that the thermal stress is zero when the cam material is the same as the strip material, thus titanium. Since the thermal stress is also included in the preload, the case where the cam is made out of titanium will have the lowest stress in the strips.

Preload stress The required preload can be calculated with the help of the free body diagram of the lower cam, given in the illustration in Figure 10.6b. The two cams will always be in contact when the normal force between the two cams in rest is as large as, or larger than the maximum vertical load applied. In this case, the maximum load is the load in z-direction during launch. The required preload is then:

$$F_{pre,launch} = \frac{N}{2 \cdot sin(\theta)} \tag{10.5}$$

Where N is the required normal force. The angle θ is dependent on the inner and outer radii of the cam, as can be seen in Figure 10.7. The relation between the angle θ and the inner and outer radii of the cam is:

$$\theta = cos^{-1}\left(\frac{R_{inner}}{R_{outer}}\right) \tag{10.6}$$

Inserting this expression for $theta$ into Equation 10.6 gives:

$$F_{pre,launch} = \frac{N}{2 \cdot sin\left(cos^{-1}\left(\frac{R_{inner}}{R_{outer}}\right)\right)} = \frac{N \cdot R_{outer}}{2 \cdot \sqrt{R_{outer}^2 - R_{inner}^2}} \tag{10.7}$$

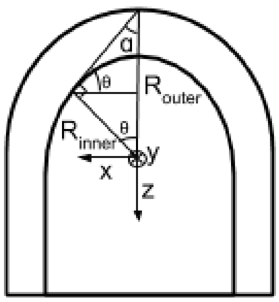

Figure 10.7: Schematic illustration of the relation between the angle θ and the inner and outer radii of the cam.

Then, the total stress due to preload is:

$$\sigma_{preload} = \frac{F_z \cdot R_{outer}}{t_{strip} \cdot w_{strip} \cdot \sqrt{R_{outer}^2 - R_{inner}^2}} + \sigma_{pre,thermal} \tag{10.8}$$

Note that the factor 2 in Equation 10.7 is not present in Equation 10.8. This is due to the definition of w_{strip}, which is the combined width of the strips, but preload is applied on the mid strip, and applied to the outer strips combined. This means that in the stress calculations due to the preload, only halve the width of the strips has to be taken, which cancels the factor 2 in Equation 10.7.

Launch stress The stress in the strips during launch depends on the load case on the system. From the requirements, three load cases are considered. The mass of the system, based on CAD models to this point, is estimated to be 12 kg. Figure 10.7 gives the coordinate system used. In load case 1, there is a 30 G acceleration in the Z and X direction. In case 2, there is an acceleration in the Z and Y direction, and in case 3 there is an acceleration in the Y and X direction (see Chapter 4). Due to the preload in the strips, the acceleration in the Z direction does not introduce any additional stress in the flexures. In the X direction, there is an additional stress in tension. The amount can be determined using the FBD in Figure 10.6b. It is noted that there is no normal force acting in the X direction. Thus, when a load is applied, the strip will deform to balance the applied load. When one strip is put in more tension, the other, opposite strip will be reduced in tension in exactly the same amount, since the deformation of both strip is equal, but opposite in sign. The increase in tension in the one flexure will increase the sideways force in one way. However, the decrease in tension in the opposite strip will decrease the sideways force in the other way with the same amount. The resultant sideways force is thus $2 \cdot \Delta F cos(\theta)$ The required change in tension in the strip is thus:

$$\Delta F = \frac{F_x}{2 \cdot cos(\theta)} \tag{10.9}$$

Thus the stress due to a force in the X direction is:

$$\sigma_{launch,x} = \frac{\Delta F}{t_{strip} \cdot 0.5 \cdot w_{strip}} \tag{10.10}$$

The launch load in the Y direction will impose a shear stress within the strips. This shear force is taken up by all strips in parallel. Thus the force acts over the entire w_{strip}, which results in an area twice as high compared to the area affected by the preload.

$$\tau_{launch,y} = \frac{F_{launch,y}}{t_{strip} \cdot w_{strip}} \tag{10.11}$$

Full stress equation Inserting Equations 10.1, 10.4, 10.8, 10.10 into Equation 10.3 gives the following expression for the total stress state in the strips:

$$\begin{aligned} \sigma_{total} =& \frac{E_{strip} \cdot t}{2 \cdot R_{inner}} + \left(CTE_{cam} - CTE_{strip}\right) \cdot \Delta T \cdot E_{strip} \\ &+ \frac{F_z \cdot R_{outer}}{t_{strip} \cdot w_{strip} \cdot \sqrt{R_{outer}^2 - R_{inner}^2}} + \frac{F_x \cdot R_{outer}}{R_{inner} \cdot t_{strip} \cdot w_{strip}} \end{aligned} \tag{10.12}$$

From Equation 10.12 it can be seen that five parameters determine the stress within the strip under an applied load case. The first parameter is the CTE difference between the strip and the cams. It can be seen that it is beneficial to use the same material for the strip and the cams, especially since the hinges are subjected to a large thermal load during LEOP (see Chapter 4). When selecting Kevlar®, which has a negative CTE, the problem is increased further. For that reason, titanium cams are considered.

The next parameter is the outer radius of the cams. Due to design limitations, this was set to 35 mm. This means that the diameter of the cams is the same as the diameter of the booms. Decreasing the radius would give higher stresses in the strips, since then the inner radius should also be decreased. Increasing the outer radius beyond 35 mm would give problems for the design of the hinges and booms.

The two listed parameters above are thus constants. The next parameter, the inner radius of the cams, is not a constant. it can be seen in Equation 10.12 that increasing the inner radius is beneficial for the bending stress, but would increase both the preload and launch stresses. This same but opposite behaviour can be seen in the thickness of the strips. Increasing the thickness of the strips will increase the bending stress, but will decrease the launch and preload stresses. Thus there is an optimal point for the strip thickness and cam inner radius, where the stress is minimal.

The last parameter is the total width of the strips. From Equation 10.12 it can be seen that increasing the width of the strip will decrease all forms of stress.

Optimal design point From the above observations, the optimisation approach can be determined. Since two out of five parameters are constant, the optimisation only considers three parameters. First the optimal point between the strip thickness and the cam inner radius is determined. After that, the total width of the strips is determined by setting the total von Mises stress in the flexure equal to the yield stress of the strip material. The optimisation was performed in Matlab. Figure 10.8 gives the von Mises stress within the strip at a given width as function of inner radius and strip thickness. It can clearly be seen that there is a single design point for the thickness and inner radius that result in the lowest stress within the strips for a given strip width.

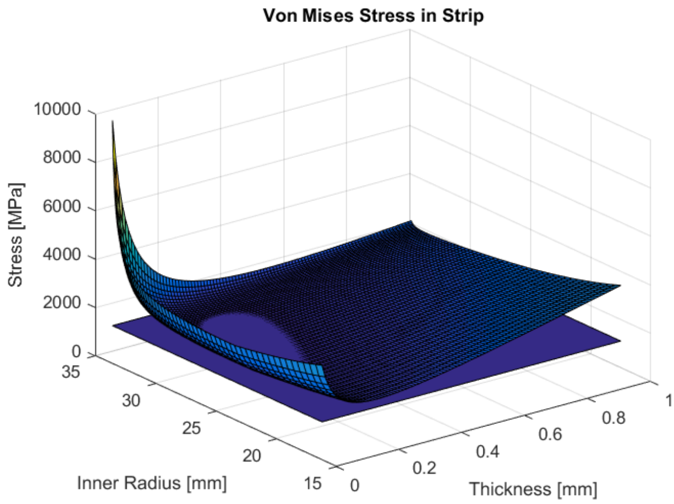

Figure 10.8: Stress within the CORE strip at a given width as function of CORE inner radius and strip thickness. The flat surface is the yield strength of the used titanium alloy. It can be seen that there is an optimal point with minimal strip stress.

There are three load cases, and for each load case the optimal design point is found. After that, each optimal design point is checked for the other load cases. From these three optimal design points, the point with the lowest required total strip width is selected. This criteria was used since the increase in width has the highest influence on the total weight of the hinge design. The optimal design point is given in Table 10.5.

Table 10.5: Design values for the metal strips and cams resulting from the optimisation

Parameter	Value [mm]
Strip thickness	0.3
Inner radius	29.7
Outer radius	35
Total strip width	31

Cam Design

The next step in the design was to find the final dimensions required for the cams. The inner and outer radii are already determined, together with the metal strip width. This width is not yet the total width of the cams, since it does not take the width of the cam rolling surfaces into account. These surfaces will be under compression, and it has to be checked if this stress does not result in failure of the hinge.

The contacting bodies are two cylinders. From [54], the stress within the material can be determined as a function of depth. The situation is given in Figure 10.9.

In [54], it is stated that the maximum principle stresses in a Herzian contact occur on the z axis (see Figure 10.9 for the orientation of the reference frame). In a Herzian contact, the interface between the

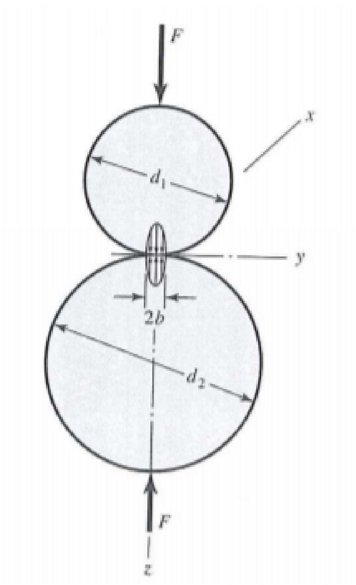

Figure 10.9: Contact stress within two contacting cylinders. Image taken from [54].

bodies is assumed to be frictionless. The principal stresses are determined with the following equations [54]:

$$\sigma_x = -2\nu p_{max}\left(\sqrt{1+\left(\frac{z}{b}\right)^2} - \frac{z}{b}\right) \tag{10.13}$$

$$\sigma_y = -p_{max}\left[\left(2 - \frac{1}{1+\left(\frac{z}{b}\right)^2}\right)\sqrt{1+\left(\frac{z}{b}\right)^2} - 2\frac{z}{b}\right] \tag{10.14}$$

$$\sigma_z = \frac{-p_{max}}{\sqrt{1+\left(\frac{z}{b}\right)^2}} \tag{10.15}$$

In these equations, z is the distance from the contact point along the z axis. b and p_{max} can be calculated using the following equations [54]:

$$b = \sqrt{\frac{2F\left(\frac{(1-\nu_1^2)}{E_1} + \frac{(1-\nu_2^2)}{E_2}\right)}{\pi l\left(\frac{1}{d_1} + \frac{1}{d_2}\right)}} \tag{10.16}$$

$$p_{max} = \frac{2F}{\pi b l} \tag{10.17}$$

Where F is the applied force and l the length of the contact line in x direction. Subscripts 1 and 2 refer to cylinder 1 and 2 in Figure 10.9.

A width of 5 mm per contact surface was taken for the cams, resulting in a total contact length l of 20 mm. The applied load was taken to be the required normal force, calculated in the previous section. The resulting contact stress as function of z is given in Figure 10.10. The maximum von Mises stress is 319 MPa, which is lower than the yield and ultimate material stresses.

In the above calculation, the four contacting surfaces are grouped together into a single contact area. This was done because the load case is undetermined. Due to the symmetry of the cams, the load at each contact point cannot be calculated using stiff members. In the real world, the cams will

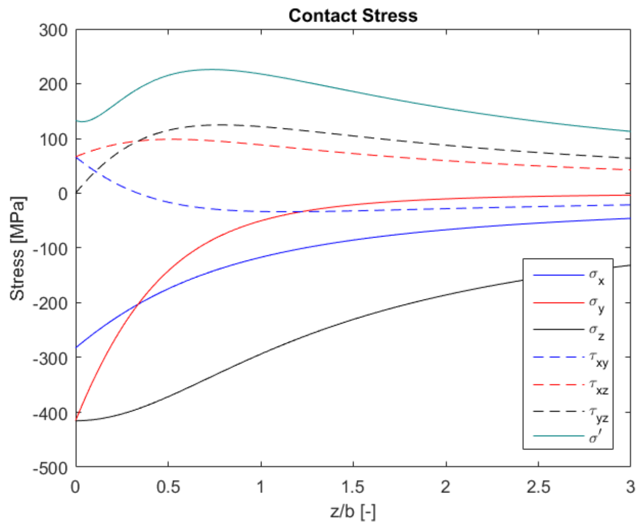

Figure 10.10: Contact stress in the cams as function of the z position as calculated by hand calculations.

deform, changing the load cases. To check this effect, ANSYS was used. It is noted that ANSYS is not particular good at solving contact stresses due to the high non-linearity of the system.

In the modelling, the symmetry of the cams were used to reduce the number of nodes, or in this case, decrease the size of the elements due to the element number limitations of the license used. The contact areas are refined, since it was seen in the hand calculations that the area affected by contact stress is very limited. The contact area was modelled as frictionless. This is in agreement with the assumption of Herzian contact made for the hand calculations. The behaviour was set to symmetric, since both bodies are flexible. Since the analysis is highly non-linear, in the analysis settings the number of steps was increased to ensure the solver would converge. Evaluating the first results showed that the penetration between the bodies was high, and the stiffness was altered to ensure acceptable penetration levels. The maximum penetration was 0.17 micron in the final analysis. The result of the analysis is shown in Figure 10.11.

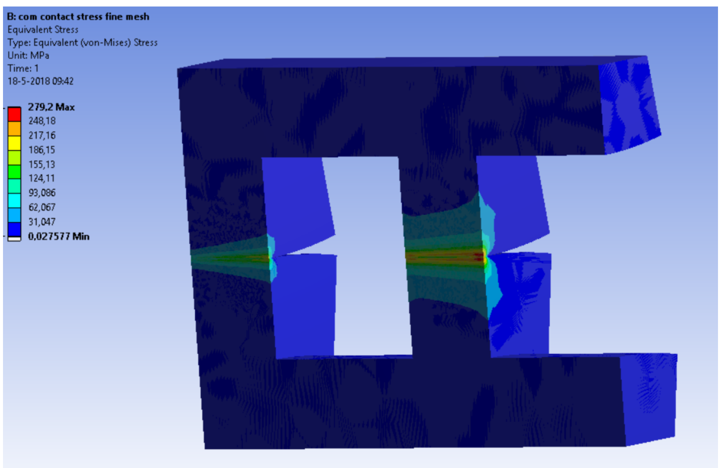

Figure 10.11: Contact stress within the cams. Only a quarter of the cams is shown.

From this result, it can be seen that the inner cam surfaces take more load than the outer cams. It can thus be concluded that the hand calculation is the average of the maximum contact stresses. Even though the contact stress is not constant, the value calculated with ANSYS is still well below the yield stress of titanium.

10.2.4. Preload Device

As stated before, the design of the hinge requires a preload. How this preload is applied was not discussed yet. This will be the subject of this section. However, before the preload device is discussed, first the bonding of the strips to the cams is briefly discussed.

10.2.5. Strip Bonding

The strips have to be connected to the cams. It was chosen to bond the strips to the cams. This was because bonding will generate a more even load distribution over the strip compared to clamping, and requires less volume. The bonding stress was taken to be 30 MPa, which was based on space proven adhesives in [21]. The maximum force acting on the bond was taken from the maximum load case on the metal strips. Based on the selected strip width, the required bonding length was about 12 mm.

10.2.6. Preload Concepts

The metal strips have to be preloaded to ensure the hinge will work. The required preload was determined during the metal strip design and has a value of 1388 N. This number was based on the preload calculated for the design point in Section 10.2.3. Five different concepts were considered to set this preload. All concepts have the interface with the metal strip in common. The metal strip is bonded to a sled that slides over two rods, see Figure 10.12. The concepts considered are listed below.

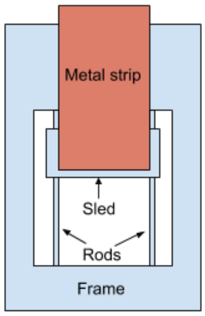

Figure 10.12: Sketch of the preload device for the metal strips in the CORE hinges. The sketch illustrates the connection between the metal strip and the preload device. This interface is used for all preload concepts.

- Bolt tension
- Belleville washers
- Bolt + belleville washers
- Tension/compression springs
- Leaf spring.

Bolt tension

In this concept, the preload is introduced by tightening a bolt, pulling the sled towards the frame. The benefits from this concepts are the rigid connection between the sled and the frame, and the low volume required for this concept. However, the tension depends on the elongation of the bolt, which is small. A small change in dimensions within the structure can influence the preload significantly.

Belleville washers

These conically shaped washers are often used to preload bolts. In this concept, they are placed between the frame and the sled. During assembly, the sled is pushed back, loading the washers. When the adhesive is cured, the sled is released, putting the preload on the metal strip. The benefit of this concept is the small volume. However, the deflection of the washers is limited. When released, the elastic deformation in the metal strip will reduce the preload on the metal strips. This decreases the accuracy of the preload in the system.

Bolt with belleville washers
This concept combines the two previous concepts. The bolt is tightened to create the preload. By doing this, the belleville washer which is located between the bolt and the frame is also preloaded. There is a stiff connection between the sled and the frame, but a small change in dimensions does not influence the preload as much as in the bolt concept. Furthermore, the elastic deformation in the metal strips do not influence the amount of deformation in the belleville washer(s), which increases the accuracy of the preload.

Tension/compression springs
The preload can also be generated by standard springs. During the assembly, the sled is pushed back. After the adhesive has cured, the sled is released, putting the metal strip under preload. Due to the lower stiffness of springs, the change in dimensions in the system does not influence the preload as much. However, this reduction in stiffness can result in more deformation during launch. Furthermore, the volume required is high, which can be a problem for the top hinge.

Leaf spring
This concept is similar to the previous concept, only now the springs are replaced by a leaf spring. This was done to reduce the required volume. However, the lack of stiffness is still present.

10.2.7. Concept Selection Preload Device

The different concepts are compared to each other in Table 10.6. From this trade-off, it can be concluded that the concept using a bolt in combination with belleville washers is the best option.

Table 10.6: Trade-off table of the preload device concepts.

Concept	Volume	Stiffness	Sensitivity	Precision
Bolt	Green Micron level deflection needed	Green Direct connection	Red High spring stiffness	Yellow Bolt friction
Belleville washers	Green Small deflection needed	Green High spring stiffness	Yellow High spring stiffness	Yellow Unknown spring back
Bolt + belleville washers	Green Small deflection needed	Green High spring stiffness	Yellow High spring stiffness	Blue Precise spring deflection
Tension/ compression springs	Red Large deflection needed	Yellow Low stiffness	Green Low spring stiffness	Blue Precise spring deflection
Leaf spring	Yellow Large deflection needed	Yellow Low stiffness	Green Low spring stiffness	Blue Precise spring deflection

Green	Excellent	Yellow	Sufficient
Blue	Good	Red	Unacceptable

This concept is worked out in more detail. The tension in the bolt is a pure tension load. Since the two clamped materials (the frame and the sled) are not touching, all the preload is carried by the bolt. Instead of the yield stress, the proof stress is used. For steel bolts, the proof stress is given in [54]. For non-steel bolts, the proof stress can be taken as 85% of the yield strength [54]. The effective areas of the bolts are also taken from [54]. To limit the thermal effects on the system, the bolt is made from titanium. The yield stress was taken to be 830 MPa [36]. From the analysis, it was concluded that an M4 bolt can take the stress. The belleville washers were based on a Inconel 718 belleville washer from Solon Manufactoring Co.. Inconel 718 was selected since it is corrosion resistant, without being magnetic. The washer can deliver 1646 N, with a deflection of 0.2 mm [11]. To increase the deflection, three washers were placed in series. It must be stated that the design of these washers can be changed such that they deliver a constant load over a specified deflection region [54]. This can be very useful for this application, however a constant force from a spring means a zero stiffness spring. The effect of this on the functionality of the concept has to be investigated. The effect of changing the dimensions in the belleville spring on the force as function of deflection can be seen in Figure 10.13.

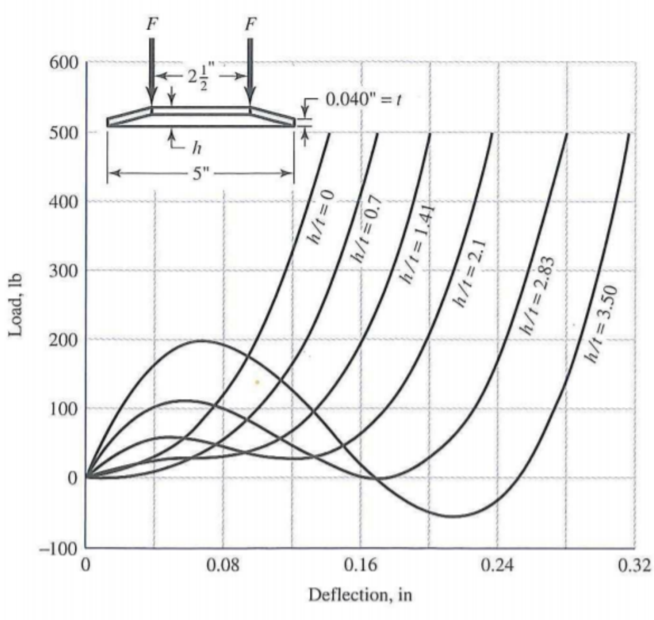

Figure 10.13: Effect of the shape of the belleville spring on the force as function of deflection. Image taken from [54].

10.2.8. Surface Treatments

Titanium is known for being affected by fretting and cold welding [47]. Since the cams are pressed against each other, this system is at risk of cold welding. During launch, the protective layer around the titanium may be removed due to fretting, after which cold welding may take place, locking the system in the stowed configuration. Since this is unwanted behaviour, ways to prevent cold welding were investigated. The use of surface treatments or coatings may prevent cold welding. The difference between a coating and a surface treatment is that a coating is a separate material applied on the material, resulting in a layer of this material around the component. In a surface treatment, the surface material of the component itself reacts with the applied chemical, forming a surface layer with a strong bond to the unaffected material beneath the layer.

In the database in Appendix C of [47], it was found that for Ti-6Al-4V alloy five tested surface coatings and treatments were effective in preventing cold welding. These surface treatments were Balinite A, Balinite B, Dicromite +, Ni + PTFE, and Keronite. For cold welding due to fretting, only two surface coatings/treatments were effective, Ni + PTFE and Keronite. In the text however, it was stated that each surface treatment suffered from fretting. In the titanium tests, the Keronite surface treatment was only applied to one of the specimens, the other was untreated titanium. Further, the thickness of the keronite layer was 6 microns thick. Test results of different treatments and coatings can be seen in Figure 10.14.

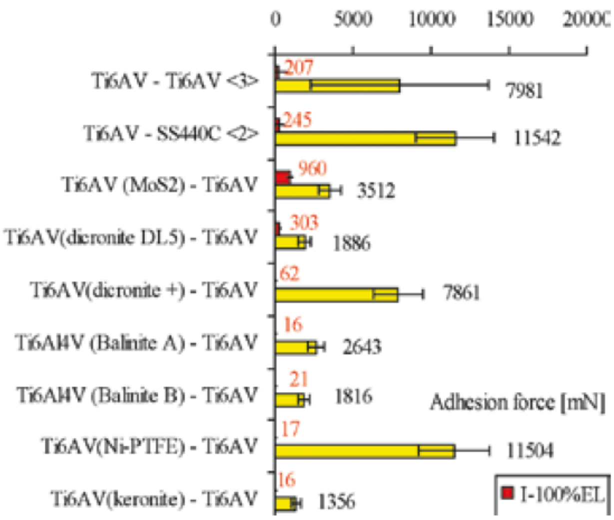

Figure 10.14: Results of cold welding tests on Ti-6Al-4V after impact and fretting for different surface treatments. Image taken from [47].

To test the effect of surface treatment thickness, [47] increased the thickness of the Keronite layer for aluminium and ball bearing steel. It was concluded that increasing the Keronite layer above 17 microns greatly improves the resistance against fretting and cold welding. The surface treatment was also applied on both specimens in contact, and it was concluded that the coating broke and cold welding occurred. However, by applying a film of MoS_2 (physical vapour deposition) this problem was solved [47]. Apart from the fretting and impact tests, [47] also performed a thermal test. The result was that the surface treatment does not suffer from thermal loading.

Based on the results given in [47], it was decided to add a Keronite surface treatments of at least 17 micron on both cams, with a MoS_2 layer in between. The UK based company Keronite International Ltd. has developed several versions of the treatment. For now the Keronite Endure is chosen, since it is developed for wear resistance [43].

10.2.9. Final Design

Up to now, the general dimensions of the hinges are determined. However, these dimensions still have to be translated to producible designs for the hinges. This last step is performed here. First, an overview of the general dimensions are given in Table 10.7.

Table 10.7: Overview of the general dimensions of the CORE hinges.

Parameter	**Dimensions [mm]**
Strip thickness	0.3
Strips total width	31
Outer radius cams	35
Inner radius cams	29.7
Fillet radius	0.5
Cam contact surface width (total)	20
Total width	54
Bolt size	M4 (4)

The root hinge was designed first. The hinge has to provide a deployment angle of 180 degrees to the boom. Due to the concept of the hinge, each halve will only use 90 degrees of the total 360 degrees of a cylinder, measured at the centre of the cylinder. However, the strips require more space than that. Thus, the contacting parts of the cams with a radius of 35 mm only have to span 90 degrees, where the inner radius of 29.7 mm has to span more than this. This design requirement makes it very hard to design producible, single component hinge halves. It was thus decided to split the hinge halves in several easier to produce components.

At the hinge part connected to the instrument bus a small flange was added on the sides of the cams. Its purpose is to protect the strips from yielding when the applied force parallel to the rotation axis would be too high. The preload device was added to the hinge halve connected to the instrument bus. It is added to this halve, simply because there is more room available. For the top and root hinges, the surfaces of both cams will be treated with Keronite Endure of at least 17 microns thick, with a layer of MoS_2 in between to prevent cold welding. The final design of the root hinge, including the strips is presented in Figure 10.15.

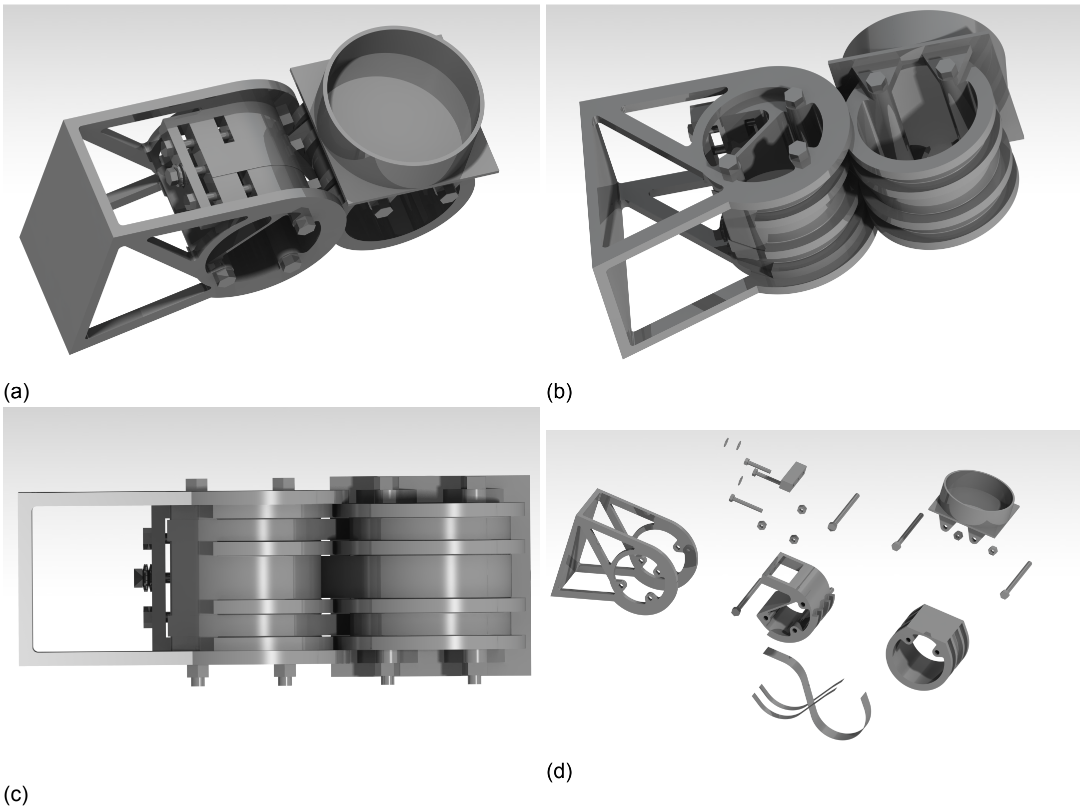

(a) (b) (c) (d)

Figure 10.15: Renders of the root hinge

For the top hinge the required deployment angle is small, only about 30 degrees. Due to the hinge concept, the cams only have to span over 15 degrees of the cylinder, measured at the centre. This means that the cylindrical surfaces can be made smaller compared to the root hinge. This reduces volume, and thus also mass. The preload device was added to the spider halve of the hinge. This location was chosen again because the available space at this point. The structure of the preload device can also be used to attach the ribbons. Renders and exploded view of the hinge are presented in Figure 10.16.

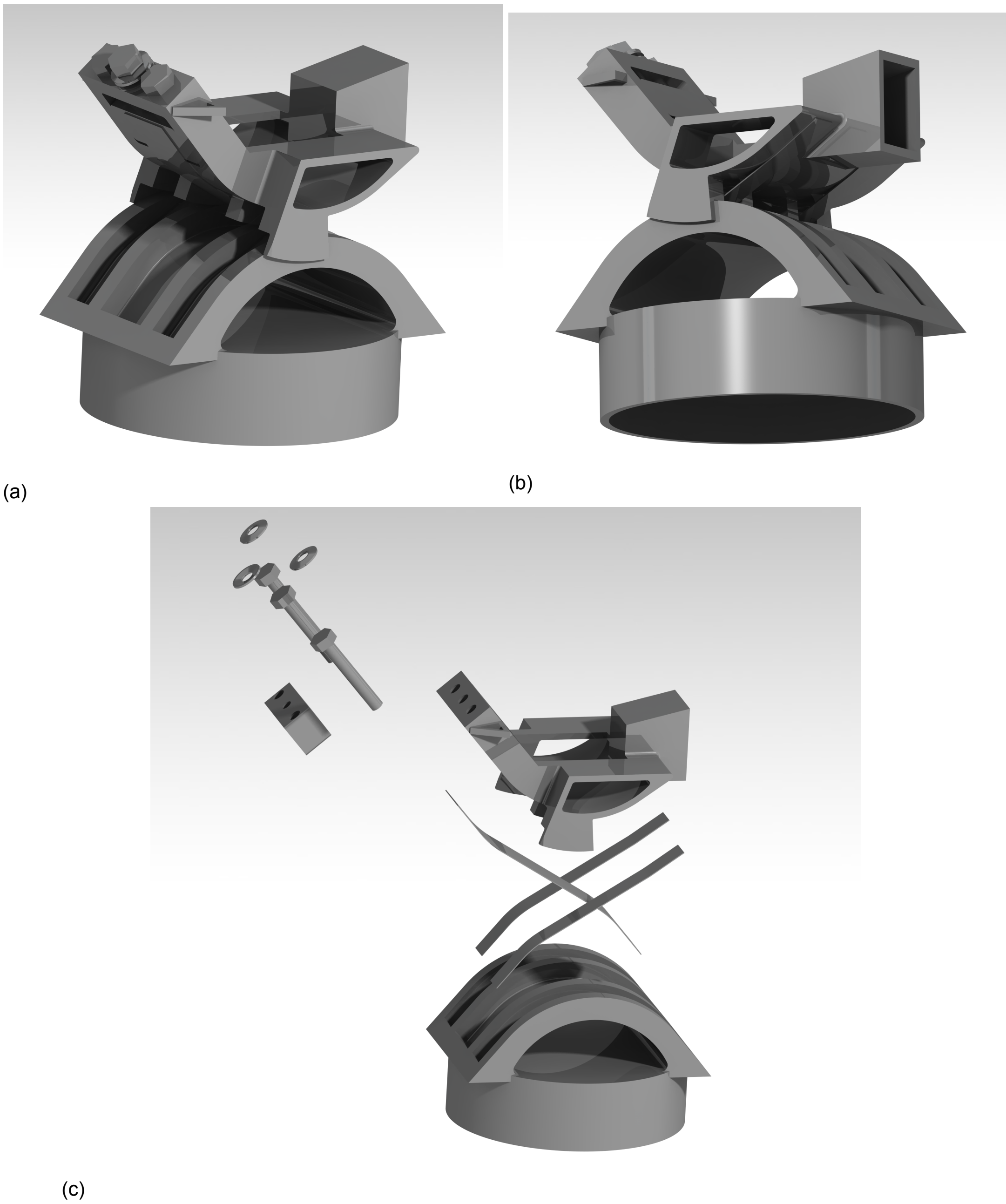

(a) (b)

(c)

Figure 10.16: Renders of the top hinge.

10.3. Conclusion

In this chapter the detailed design of the top and root hinges were discussed. The chapters started with a trade-off between different concepts. It was concluded that for both the top and the root hinge the CORE hinge concept was the best option. Due to the high similarity between the two hinges, the hinges were first designed in parallel.
It was beneficial to make sections in the cams with different radii. This way the radius over which the strip rolled was different than the radius of the cylinders in contact. With this configuration, it is possible to press the cams against each other, preventing separation during launch.
Three optimisation parameters were identified: the cam inner radius, strip thickness, and the total strip width. It was concluded that there exists an optimal point for the inner radius and strip thickness, where independently from the total width the lowest stress level within the strip is reached. The width of the strips was then changed until the stress levels within the strips under loading was acceptable.
The contact length of the cams was set to four times 5 mm. The resulting contact stress was calculated, and checked if it was below the yield stress of the material.
The strips have to be preloaded. With the help of a trade-off, a preload device was chosen. The preload is applied by a combination of bolt tension and belleville washers.
The cams are in contact. Since both the cams and the strips are made out of the same titanium alloy, there is a risk of cold welding. It was suggested to treat the surface of the components with a Keronite Endure surface treatment, in combination with a layer of MoS_2 solid lubricant.
The designs for the top and root hinges were worked out in detail and weight saving was applied where possible.

11 Vibration Analysis & Ribbon Design

In Chapter 8 it was decided to investigate the use of ribbons to decrease the motion of the spider, and with that the secondary mirror. In the previous chapter the root and top hinges were designed in detail. This chapter continues the design by incorporating the ribbons in the design. This is done in several steps. In the first section, the ribbon concept will be discussed, followed by a modal analysis with varying ribbon stiffness to see the effect of the ribbons on the eigenmodes of the system. In the third section, a harmonic analysis is performed on five different models. The chapter is ended with a short conclusion.

11.1. Ribbon Concept

In the first concept of the ribbons the ribbons were attached to the centre of the of the spider and the root hinge, see Figure 9.1. This provides stiffness in the translational modes of the system, but does not improve the stiffness of the rotational eigenmode. During a discussion with Dr. Just Herder another option was found. Two ribbons per boom are spanned between the top hinge and the primary mirror support structure (PMSS). Two triangles are then created, both out of the plane made by the boom and the spider. This way, not only the translative motion of the spider is limited, also the rotational motion is limited. A render of this concept is given in Figure 11.1.

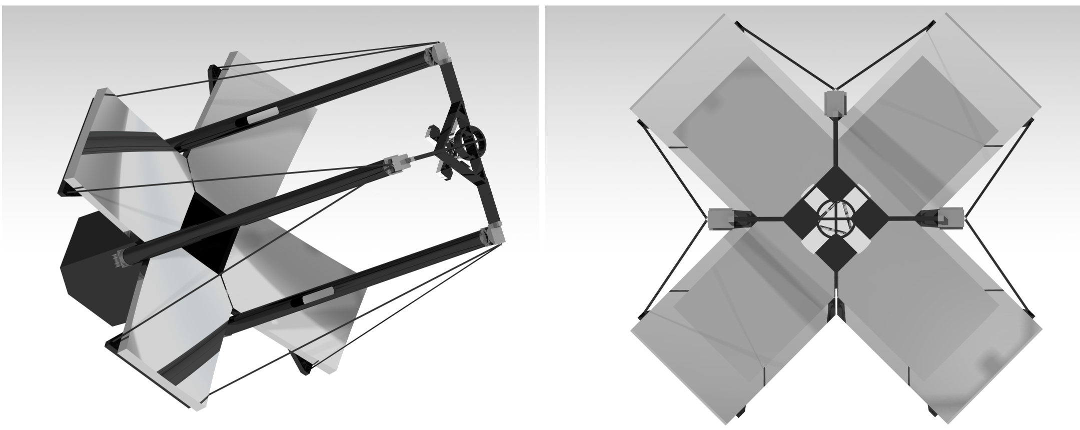

(a) Front view (b) Top view

Figure 11.1: Renders of the three boom with ribbons concept.

The connection to the primary mirror segments will influence not only the SMSS, but also the PMSS. Before the concept could be considered, first a discussion with M. Corvers, working on the PMSS, was needed. The result of this discussion was the integration of the two systems. In this concept, the ribbons spanning between the PMSS and the top hinges of the SMSS are used to preload the kinematic interface between the PMSS and the instrument bus, and increase the stiffness of the SMSS. Before that, the PMSS was deployed using a deployable boom below the mirror segment. In the new design, the PMSS falls into a kinematic mount on the instrument bus.

This however, introduces another design choice. The current design has three booms and is thus asymmetrical. There are four primary mirror segments. This means that two of the segments are attached with two ribbons to the SMSS, one on each side of the segment. The other two segments will only be attached at one corner to the SMSS. This will introduce a twist in the structure and an uneven loading on the kinematic interface. This behaviour is unacceptable for the primary mirror segments. If ribbons are to be used and connected to the PMSS, then the number of booms have to be four. This will reintroduce symmetry in the concept. If this concept is chosen, structural stiffness and symmetry are thus favoured over an exactly constrained design. A render of the concept is given in Figure 11.2. In the next section, the effect of the ribbons to the eigenmodes of the system is investigated.

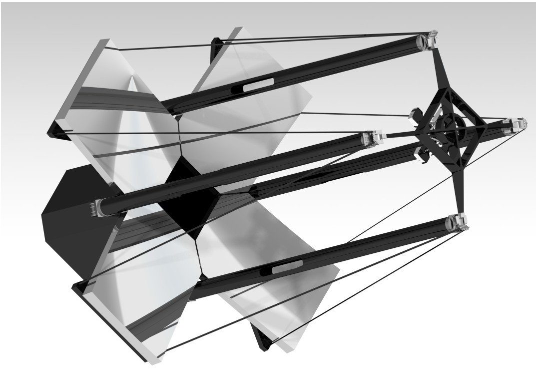

(a) Front view

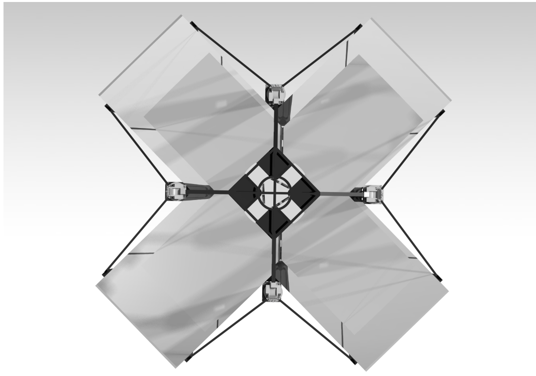

(b) Top view

Figure 11.2: Renders of the four booms with ribbons concept.

11.2. Modal analysis

The first assessment of the ribbon concept was in the form of a modal analysis. It was chosen to use a modal analysis for the reason that it is a good indication of the effect of the ribbons on the structure stiffness. By varying the ribbon stiffness, the sensitivity of the design to a change in ribbon stiffness can also be observed. In this section, the results of the modal analysis is given.

11.2.1. Model

For this analysis, only one single model is needed. Since the PMSS demands that if ribbons are attached to the PMSS, the number of booms needs to be increased to 4, the current model is modified.

In the previous chapter, the top and root hinges were designed in detail. However, this level of detail is not needed for this analysis, since the focus lies on the ribbons and not on the hinges. The hinges were simplified in order to make the meshing easier. Since the vibrations will only span small deflections, the hinges were again modelled as revolute joints. The densities of the material of the hinges, titanium, was changed in order to give the hinge parts the correct mass. A screenshot of the two hinge models can be found in Figure 11.3.

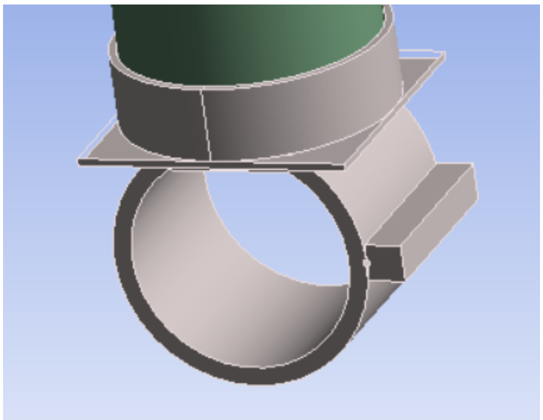

(a) Simplified root hinge

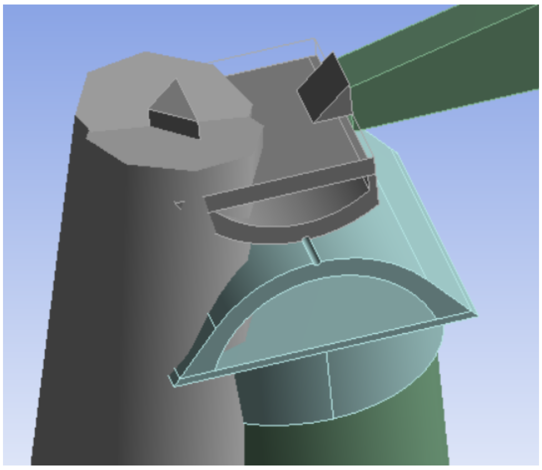

(b) Simplified top hinge

Figure 11.3: The simplified top and root hinges used in the analysis.

The secondary mirror was previously modelled as a solid piece of silicon carbide. However, this will be a too conservative estimation, since the topology of the mirror substrate will be optimised later in the DST project. From literature it was found that mirrors are often lightened to 20 to 30% of their original weight, but can be as low as 10% of their original weight [4, 67]. since the shape of the M2 mirror is not a standard shape and there was no optimisation done on its topology so far, a saving of 70% was taken. Since introducing pockets in the M2 substrate would make meshing more difficult, it was chosen to change the density of the material. This can be done since only the mass will depend on the density in this analysis. The mirror and mirror interface used in the vibration analyses are given in Figure 11.4.

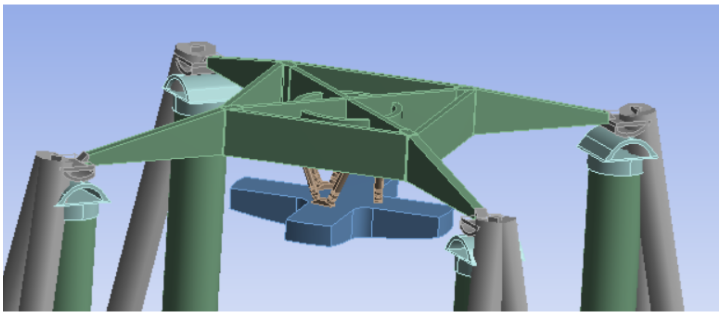

Figure 11.4: Screenshot of the simplified mirror and mirror interface used in the modal and harmonic analyses.

The ribbons will be represented by linear springs. This can be done as long as the ribbons will be under tension. This stresses again the importance of proper preload. For preload, a value of 18 N was taken. This value was based on an analysis M. Corvers did for his system. To test the influence of the preload to the system, also the preload was varied with a constant ribbon stiffness of 1000N/mm from 1 to 100 N. The stiffness of the ribbons was varied from 1 N/mm to 10,000 N/mm. The values do not necessarily represent the real values of the ribbons, but the values were taken to investigate what the effect of the ribbon stiffness is on the behaviour of the system. The full ANSYS model used for the vibration analyses is given in Figure 11.5.

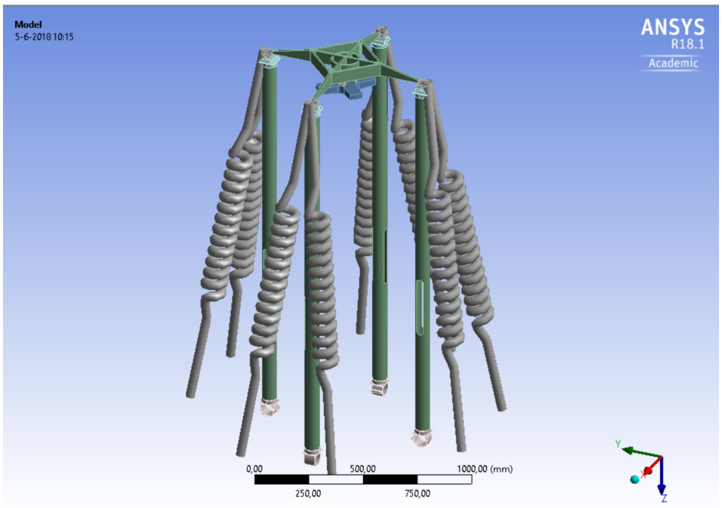

Figure 11.5: The ANSYS model used in the vibration analyses.

11.2.2. Analysis Setup

It was decided to perform a modal analysis nested on the results of a static structural analysis. The static structural analysis calculates the deformations within the structure due to the preload. These results are then fed into the modal analysis. Setting both the spring stiffness, the preload, and the frequency results as parameters, all the design points could easily be calculated without the need to change anything within the settings of the analysis. The frequencies are then extracted from the table and plotted within Matlab.;

11.2.3. Results

The results of the analysis are given in Figure 11.6. The figure shows the first six eigenfrequencies as a function of ribbon stiffness.

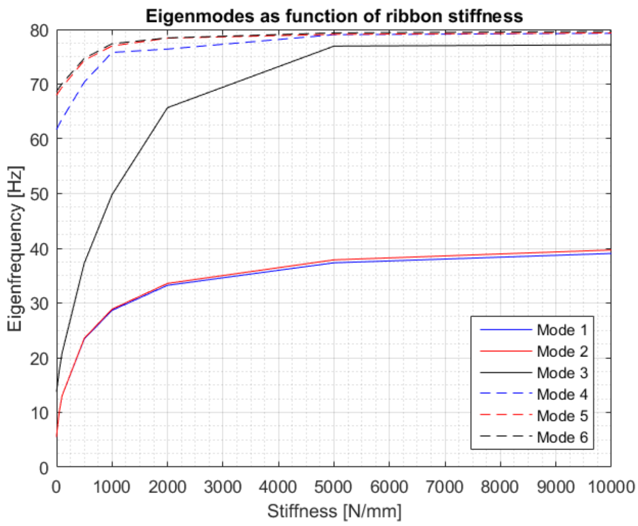

Figure 11.6: The first six eigenfrequencies of the SMSS with four booms as function of ribbon stiffness.

As can be seen from the figure, the ribbons have a large effect on the first eigenmodes, but in the higher eigenmodes the influence is less. This is according to the expectations, since the ribbons mainly limit the translation and rotation of the spider, which are the first three modal shapes. Another observation is that the increase in eigenfrequency is not linear with ribbon stiffness. it seems to approach a limit at around 40 Hz for the first two eigenmodes. This behaviour can be explained by the modal shape of the system with high stiffness ribbons. The system starts to vibrate in modes which are not affected by the ribbons.

Besides the effect of the ribbon stiffness on the system, also the effect of the preload was investigated. In the data obtained from the modal analysis, no effect of the preload on the modal response could be found. The difference in frequency for the first eigenmode was 0.02 Hz between model with 1 N preload and the model with 100 N preload.

11.3. Ribbon Sizing

In the previous section the effect of the ribbons on the system was investigated. This analysis did not use stiffness based on an actual ribbon designs. The results were used to judge the effect of particular ribbon designs on the stiffness of the SMSS. M. Corvers did a preliminary design of the ribbons, since the preload device would be mounted on his subsystem. He concluded that the maximum ribbon stiffness he could provide was 750 N/mm. This was based on a Kevlar® ribbon with a width of 8 mm and a thickness of 1 mm. The preload he needed was calculated by him to be 18 N. These values are used in the coming analyses.

11.4. Harmonic Analysis

In Section 11.2, a modal analysis was performed. In order to get an insight in the actual deflections of the system under an applied load, another form of analysis is needed. In this section, the harmonic analysis will be discussed. Five different models are used to test the influence of the ribbons and damping to the system. First the different models will be discussed. After that the used material properties will be discussed. In the next section the used spectrum for this analysis will be introduced, followed by hand calculations and the analysis setup. In the last section the results will be discussed.

11.4.1. Excitation Spectrum

Within the satellite, the reaction wheels are often the largest source of vibrations. In order to test the response of the system to these vibrations, a proper spectrum has to be selected. In his thesis, Van Putten used the first engine mode as spectrum for his analysis. He based his spectrum on the Vectronic VRW-1 which produces a maximum of 25 mNm. The static unbalance of this reaction wheel is 1 gmm. He did not take the entire spectrum into account [62].

In order to get a full spectrum, four different companies were contacted. These companies were Vectronic Aerospace GmbH (Berlin, Germany), Astro- und Feinwerktechnik Adlerhof GmbH (Astrofein) (Berlin, Germany), Sinclair Interplanetary (Berlin, Germany), and Airbus Defence and Space Netherlands (Leiden, The Netherlands). Unfortunately, only one of the companies reacted, but the communications took too long, and no data was obtained. Since no data was obtained from the companies, another way of getting a useful spectrum had to be found. Two useful papers were found that describe the vibrations of reaction wheels. The first paper is a master thesis, describing the model developed for the Ithaco B wheel. This wheel has a torque of around 32 mNm and was used on amongst others the Kepler spacecraft [46]. The other paper was a PhD thesis and describes the vibrations of the W45E wheel from Bradford [48].

For the Ithaco wheel, plots of the wheel speed versus disturbance force was given for selected engine modes. Based on this data, the waterfall plot could be reconstructed [46]. For the RW45E wheel, the waterfall plot was presented, but no data was given in the form of disturbance force versus wheel speed. The engine modes were given however, and with that, the given static unbalance, and the waterfall plot, the waterfall plot could be reconstructed in Matlab [48]. The results can be seen in Figures 11.7 and 11.8.

The Ithaco wheel is smaller compared to the W45E wheel. This means that the slew rate will be limited using the Ithaco wheel. It is used on the Kepler spacecraft which is heavier than the DST, but the slew rate of Kepler is probably lower than that of the DST. It was chosen to use the waterfall plot of the RW45E wheel from Bradford for this analysis.

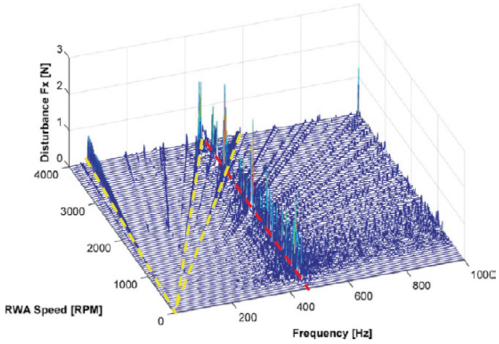

(a) RW45E data [48]

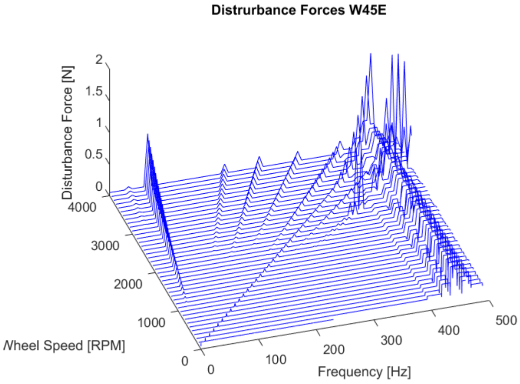

(b) Recreated data

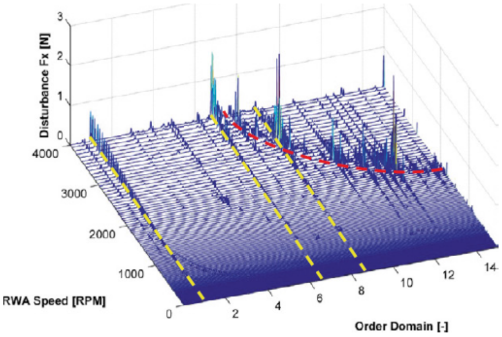

(c) RW45E data [48]

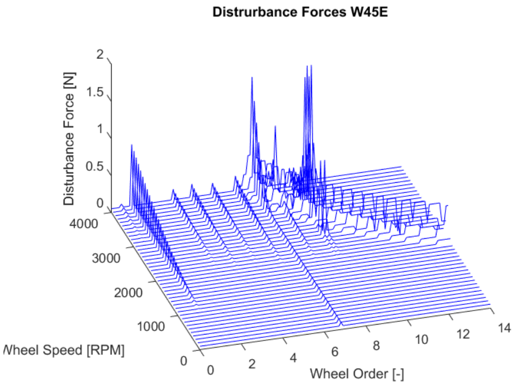

(d) Recreated data

Figure 11.7: Comparison between the original data from the Bradford RW45E reaction wheel and the recreated data. In the top row, the disturbance is given as function of wheel speed and frequency. In the bottom row, the same data is given but now as function of wheel speed and wheel order. The reaction wheel test data plots are taken from [48].

In the analysis, nine different wheel speeds are taken. The wheel speeds were 900, 1600, 2600, 3000, 3200, 3400, 3700, and 40000 RPM. The speeds are chosen such, that the most important eigenfrequencies of the system are covered. The excitation spectrum is applied to the model as a base excitation, without any additional structural damping. This assumption is a pessimistic assumption. However, since the structural properties of the instrument bus is still unknown, it was chosen to use a worst case scenario.

11.4.2. Material Properties

The material properties used in this analysis were the same as used for the design of the top and root hinges, with the addition of the material damping. There are two ways to include the damping in ANSYS. The first one is the Rayleigh damping coefficients, where constant factors are given to be multiplied by the mass and stiffness matrices. The other option is to specify a constant damping ratio. These two approaches then can be introduced as a material property, or as an assembly property. Since there are multiple materials present in the models, it was chosen to apply them as material property. The way ANSYS calculates the damping matrix is given in Equation 11.1 [7].

$$[C] = \alpha\,[M] + \beta\,[K] + \sum_{j=1}^{N_{mat}} \beta_j\,[K] + \beta_c\,[K] + \left[C_\xi\right] + \sum_{k=1}^{N_{ele}} [C_k] \tag{11.1}$$

where:

- α is the Rayleigh constant mass multiplier
- β is the Rayleigh constant stiffness multiplier

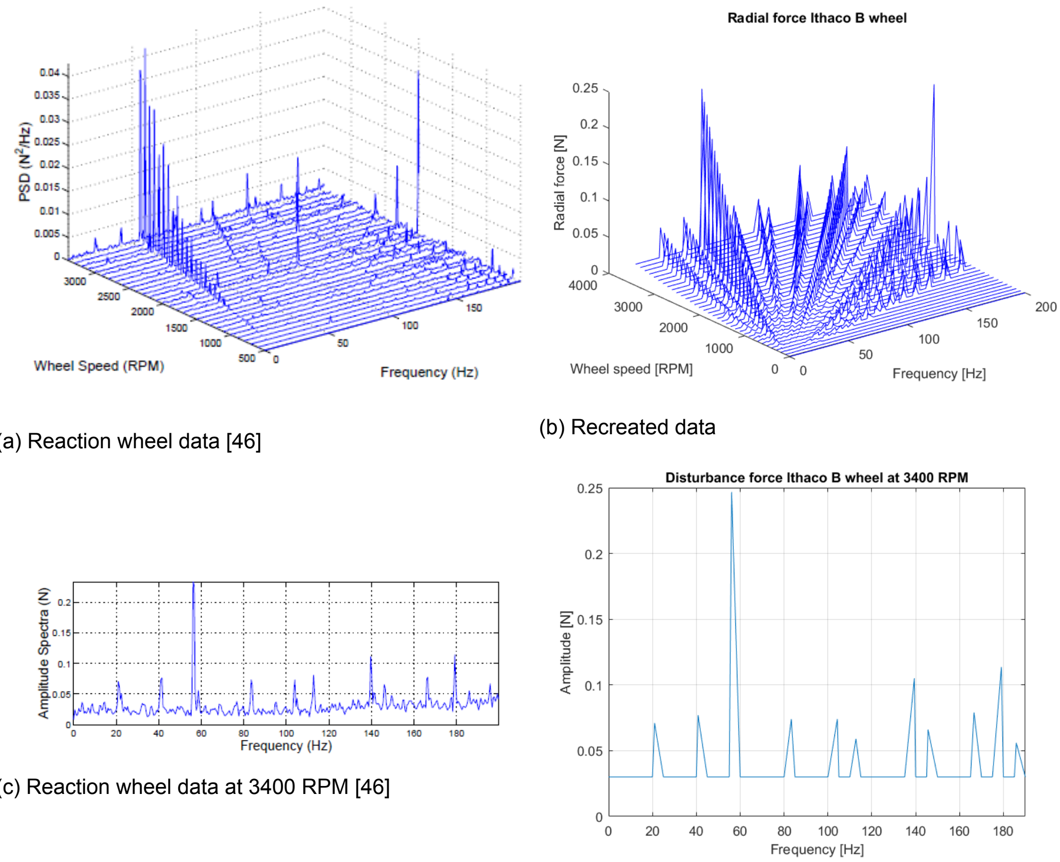

(a) Reaction wheel data [46]

(b) Recreated data

(c) Reaction wheel data at 3400 RPM [46]

(d) Recreated data at 3400 RPM

Figure 11.8: Comparison between the data of the Ithaco B wheel and the recreated data. The data and plots were taken from [46].

- $[M]$ is the mass matrix
- $[K]$ is the stiffness matrix
- β_j is the material depended constant stiffness multiplier
- β_c is the variable stiffness multiplied
- $[C_\xi]$ is the frequency dependent damping matrix
- $[C_k]$ is the element damping matrix.

In this equation, β_c is defined as follows:

$$\beta_c = \frac{2\xi}{\omega} = \frac{\eta}{\omega} \tag{11.2}$$

In [34], it is stated that the energy loss due to hysteresis within the material is:

$$\Delta E = \pi k \beta X^2 \tag{11.3}$$

Where k is the stiffness, β is the hysteretic damping constant, and X is the maximum amplitude of the vibration. The energy loss is thus dependent on the amplitude, but not on frequency. This energy loss can be modelled with an equivalent viscous damping coefficient [34]:

$$\Delta E = \pi c_{eq} \omega X^2 \tag{11.4}$$

Equating Equations 11.3 and 11.4 results in an expression of the equivalent damping coefficient for hysteresis damping [34]:

$$c_{eq} = \frac{k\beta}{\omega} \tag{11.5}$$

Furthermore, the loss factor of a material is defined as follows [34]:

$$\eta = \frac{\Delta E}{2\pi U_{max}} = \frac{\Delta E}{2\pi(\frac{1}{2}kX^2} \tag{11.6}$$

At resonance, this becomes [34]:

$$\eta = \frac{c}{\sqrt{km}} = 2\xi \tag{11.7}$$

Equating Equations 11.3 and 11.6, it is found that the loss factor equals the hysteretic damping constant. And thus:

$$c_{eq} = \frac{k\eta}{\omega} \tag{11.8}$$

comparing Equations 11.1, 11.2 and 11.8, it can be seen that if for the constant damping ratio ξ in ansys the value of $\frac{\eta}{2}$ is filled in, the damping matrix in ANSYS equals that of the equivalent damping ratio of Equation 11.8. This is also suggested by [7].

The loss factor is a material property. In the analysis, three materials are used. For titanium, a loss factor of 0.00298 was found [41]. For Aluminium, a loss factor of 0.005 was found [69]. For normal CFRP, a loss factor of 0.008 was found [10, 30]. However, there are methods to increase the loss factor of CFRP. This is done by including particles in the layer between the plies. This increases the hysteresis of the material. There are different particles with different effects. One class is the piezo particles. Coated with carbon black for better electrical conductance, these particles prove to be effective. An increase to 0.018 seems possible [30, 39, 59, 60]. In the following table, the used loss factors are used during the vibration analyses.

Material	**Loss Factor**
CFRP [10, 30]	0.008
Ti-69Al-4V [41]	0.00298
Al 7075-T6 [69]	0.005
CFRP enhanced damping [30, 39, 59, 60]	0.018

Table 11.1: Loss factors for different materials

11.4.3. Models

For the harmonic analysis, five different models were used. The models were used to test certain design features of the system. The following models were used:

- Three boom system
- Four boom system
- Four boom system with ribbons
- Four boom system with ribbons and enhanced boom damping
- Single boom test model

These models were selected to investigate both the effect of increasing the number of booms to four, the effect of the ribbons on the system, and the effect of the enhanced damping of the CFRP on the behaviour of the system. The single boom test model was added in order to provide data to validate the analyses with a test that has to be performed later in the DST project. The data obtained from the single boom model is not presented in this thesis, since it does not add directly to the design of the system, but rather will be a tool to validate the simulations later in the project. The models are given in Figure 11.9. Note that the three boom model also has ribbons. These ribbons were given a very low stiffness and preload. The reason they were included was to compare the results with the other models.

Without the ribbons, no preload could be applied to the system, which makes it impossible to perform a static structural analysis, and another analysis layout would have been needed. Furthermore, the four booms models (with and without ribbons and enhanced damping) all use the same solid model. The difference between the models is in the assigned ribbon stiffness, preload, and material damping.

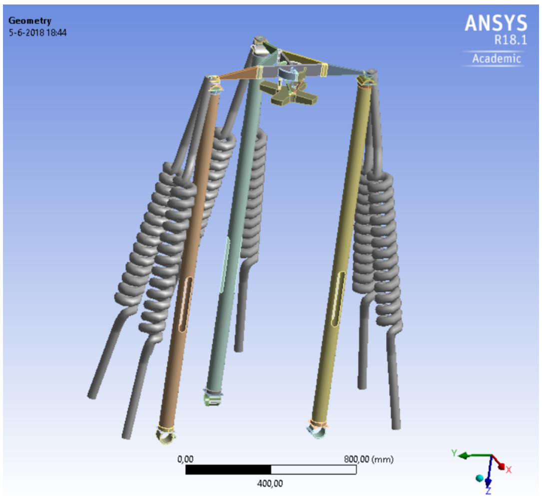

(a) Thee booms

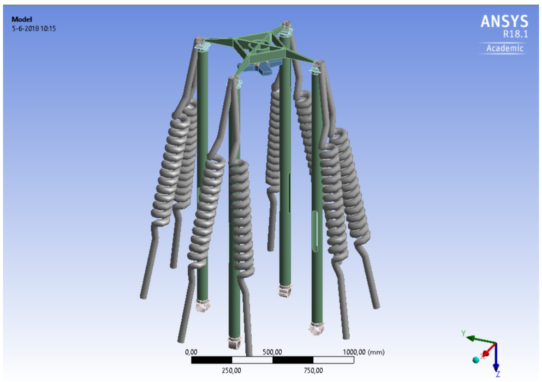

(b) Four booms

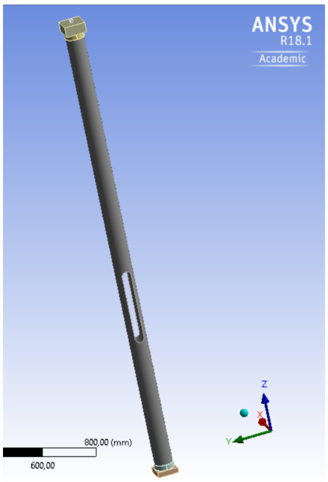

(c) Single boom

Figure 11.9: The models used in the harmonic analysis.

11.4.4. Hand Calculations

The system is modelled using a base excitation based on the spectrum of a reaction wheel. The hand calculations discussed in this section are based on a single acceleration, taken at a specific wheel speed and excitation frequency from the same excitation spectrum. For a damped system, the reaction of the system to a base excitation can be calculated using the following equation [34, 58]:

$$\frac{X}{Y} = \sqrt{\frac{1 + (2\xi r)^2}{(1 - r^2)^2 + (2\xi r)^2}} \tag{11.9}$$

In this equation, X is the amplitude of the response of the system, Y is the base excitation amplitude, ξ is the damping ratio, and r is the frequency ratio, ω_b/ω_n.

The amplitude of the response of the system in meters is required, However, the base excitation is given in acceleration:

$$y_{acc} = a \cdot cos(\omega_b t) \tag{11.10}$$

To get the base excitation in meters, the acceleration is integrated two times. The amplitude of the base displacement excitation is then:

$$Y = \frac{a}{\omega_b^2} \tag{11.11}$$

The three boom model has eigenfrequencies at 3.8 and 5.8 Hz. At these frequencies, the maximum base excitation is 0.2 mm/s^2. This results in a base displacement amplitude of 0.35 micron at 3.8 Hz and 0.15 micron at 5.8 Hz. Using for r = 1, and a damping ratio of 0.004 (CFRP, see previous sections) in Equation 11.9, a response X of 44 micron at 3.8 Hz and 19 micron at 5.8 micron.

The four boom system without ribbons has an eigenfrequency of around 5.4 Hz. The maximum base excitation is again 0.2 mm/s^2, resulting in a system response of around 21.7 micron.

One of the effects of the ribbons is that the eigenfrequency is increased to around 26 Hz. Calculating the response of the system in the same manner as the concepts without ribbons, it was determined that the response of the system would be around 1.9 micron. This calculation only takes the effect of the ribbons to the eigenfrequency into account, the additional effects are ignored. When the damping ratio is increased to 0.009 (see previous sections), the response of the system was calculated to be 0.8 micron. Again, this does not take any other effects of the ribbons into account besides the increase in eigenfrequency.

11.4.5. Analysis Setup

In order to include the effects of preload on the system, first a static structural analysis is performed. Based on these results, a modal analysis is performed. This modal analysis is required for the harmonic analysis used. The results from the modal analysis is fed into three separate harmonic analyses. Each harmonic analysis block represents an orientation of the reaction wheel. This way, the effect of placing the reaction wheel in a specific orientation can be investigated.

The setup for the single boom model is slightly different from the other models. Since it will be a ground based test, the Earth gravity is added. Furthermore, the ribbons are removed. Apart from that, the setup is the same as for the other models.

11.4.6. ANSYS Harmonic Analysis Results

In this section, the results of the harmonic analysis will be discussed. First, each model is discussed separately, after which a comparison between the models is given.

Three Booms

The first model that is discussed is the three booms option. This represents the design before the introduction of the ribbons. The responses of the system to the RW45E spectrum is given in Figure 11.10.

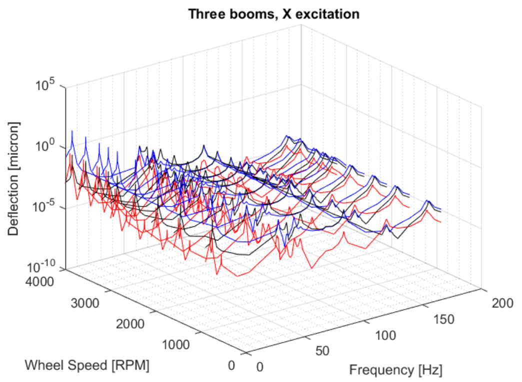

(a) X displacement of the three boom design due to disturbances in X direction as function of wheel speed and frequency.

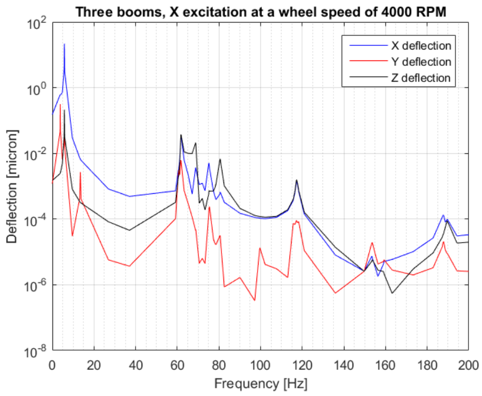

(b) Deformations of the three boom design due to disturbances in X direction as function of frequency at 4000 RPM

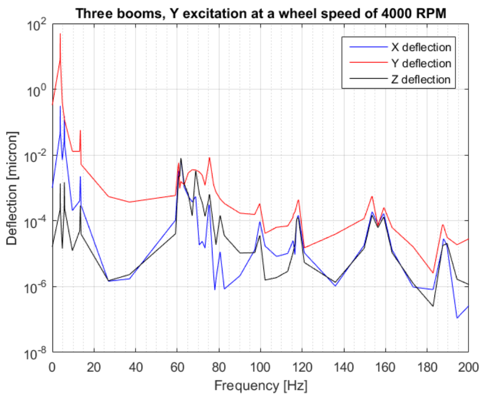

(c) Deformations of the three boom design due to disturbances in Y direction as function of frequency at 4000 RPM

(d) Deformations of the three boom design due to disturbances in Z direction as function of frequency at 4000 RPM

Figure 11.10: Response of the three boom design to the RW45E reaction wheel.

In Figure 11.10a, it can be seen that at the high wheel speeds, the response increase in the range of 50 to 60 Hz. This can be explained by the fact that at these wheel speeds, the first wheel order has a frequency in this range. The wheel order is the excitation frequency divided by the wheel speed.The first wheel order has the highest disturbance forces. Further, it can be seen that the maximum displacement in this figure is equal at each wheel speed. This can be explained by the fact that the first eigenmode of the system has a low frequency. The corresponding wheel speed is so low, that the first wheel order disturbances is still low. In Figure 11.10b, the system's response to a disturbance force in X direction is given. The maximum amplitude is at 5.8 Hz and has a magnitude of 21.7 micron. In the hand calculations, it was calculated that the maximum amplitude at the first eigenfrequency would be around 19 microns. This lies in the same order of magnitude. The difference might be explained by the fact that the hand calculations only considered a single material, CFRP. However, the ANSYS model contains also titanium and aluminium, which have a lower damping ratio. This might result in a slightly higher response. It is safe to say that the ANSYS results and the hand calculations agree. However, tests are still required to validate the simulations. This has to be kept in mind. The next largest peak, at around 60 Hz is two orders of magnitude lower. This next peak is in the range of the higher eigenmodes of the system.

In Figure 11.10c, the response of the system to a disturbance force in the Y direction is given. On first sight, it looks similar as the response given in Figure 11.10b, only now the Y response is the largest. However, the maximum amplitude is now 50 micron. This peak occurs at a frequency of 3.8 Hz. With the hand calculations the calculated maximum response amplitude was calculated to be 44 microns. Again the results are close and the difference can be explained by including other materials in the ANSYS calculations. And again, test are required to validate the results.

In the third figure, Figure 11.10d, the system's response to a disturbance in z direction is given. The first thing to note is that the maximum amplitude is about one order of magnitude smaller than the responses to disturbances in the other directions. Second of all, the maximum amplitude occurs in the X direction. Thus, for this system there is a strong coupling between the X displacement and Z disturbance forces. Both the stronger response to an Y excitation than an X excitation and the coupling between the X excitation and Z excitation can be explained by the asymmetry of the three boom design.

Four Booms

In this section, the four boom design without ribbons is discussed. The responses of the design to the disturbance forces of the RW45E wheel is given in Figure 11.11.

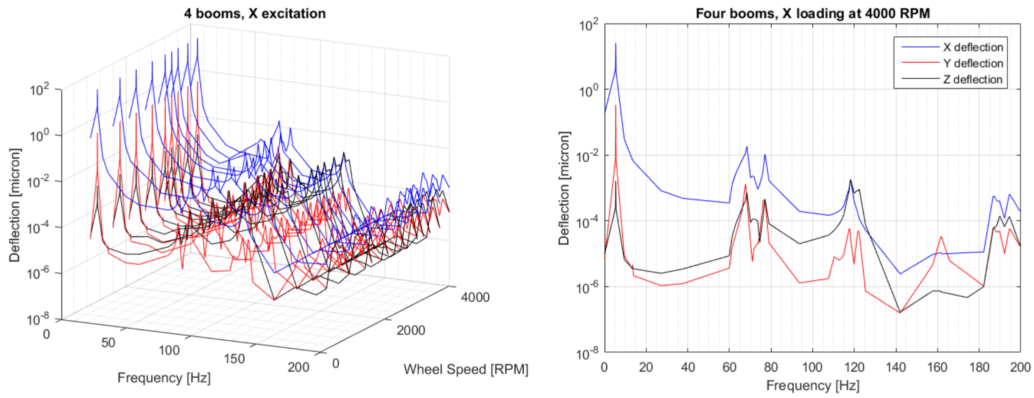

(a) X displacement of the four boom design without ribbons due to disturbances in X direction as function of wheel speed and frequency.

(b) Deformations of the four boom design without ribbons due to disturbances in X direction as function of frequency at 4000 RPM

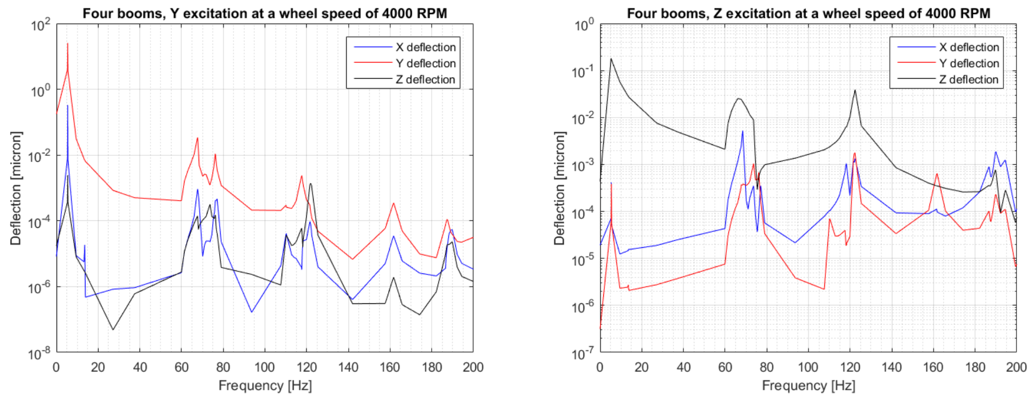

(c) Deformations of the four boom design without due to disturbances in Y direction as function of frequency at 4000 RPM

(d) Deformations of the four boom design without ribbons due to disturbances in Z direction as function of frequency at 4000 RPM

Figure 11.11: Response of the four boom design without ribbons to the RW45E reaction wheel.

In Figures 11.11b and 11.11c, it can be seen that the response of the system to an excitation in X and Y direction are similar. Only at the higher frequencies, there is a difference between the two excitation responses. Both responses have a maximum at 5.4 Hz with an amplitude of 25.4 micron. In the hand calculations it was calculated that the response would be 21.7 micron. The same argumentation for the difference between the two calculation methods can be given as for the three boom system, and again, tests are important to validate the results obtained in the simulations.

Unlike the response of the three boom system, the maximum deflection due to an excitation in the Z direction is in the Z direction. At this point, the deflections in the X and Y directions are negligible. The second peak is again between 60 and 80 Hz, in the range of the higher eigenmodes.

Four Booms With Ribbons

In this section, the responses of the four booms with ribbons design to the RW45E reaction wheel disturbances is presented. The responses are given in Figure 11.12.

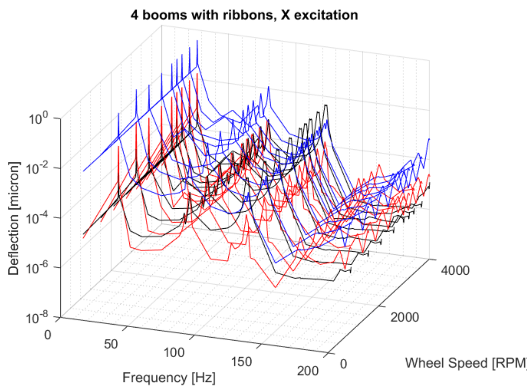

(a) X displacement of the four boom design with ribbons due to disturbances in X direction as function of wheel speed and frequency.

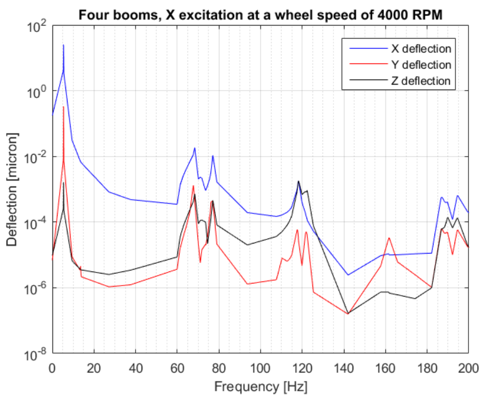

(b) Deformations of the four boom design with ribbons due to disturbances in X direction as function of frequency at 4000 RPM

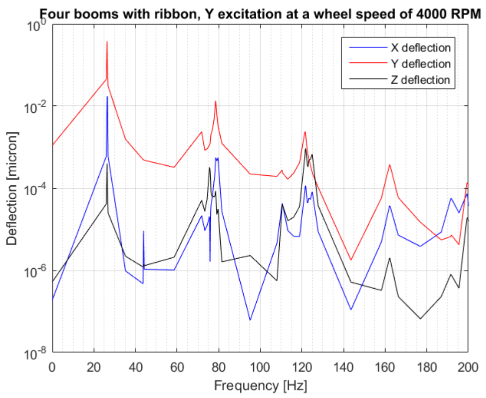

(c) Deformations of the four boom design with ribbons due to disturbances in Y direction as function of frequency at 4000 RPM

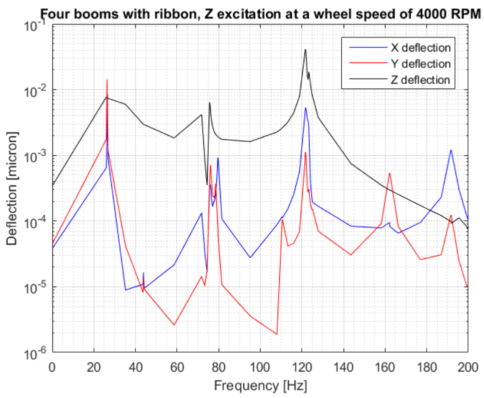

(d) Deformations of the four boom design with ribbons due to disturbances in Z direction as function of frequency at 4000 RPM

Figure 11.12: Response of the four boom design with ribbons to the RW45E reaction wheel.

Again, the responses to an X and Y excitation are comparable. Both Figure 11.12b and 11.12c have a peak at around 26.4 Hz with an amplitude of 0.377 microns at 4000 RPM. However, since the eigenfrequency is higher than the first eigenmodes of the designs without ribbons, the influence of the disturbance of the first engine mode is higher. In Figure 11.12a it can be seen that at 1600 RPM the maximum amplitude of the response of the system is 0.73 micron. In the hand calculations, it was determined that at that engine speed, the excitation would be around 1.9 micron. There is thus a difference between the results. However, the hand calculations only take the increase in eigenfrequency into account. The results are in the same order of magnitude. To truly validate the results, test have to be performed, but for now the results from ANSYS are considered verified by the hand calculations.

Four Booms with Ribbons, Enhanced Damping

The damping ratio of the CFRP was increased to investigate the effect of increasing the damping of the material on the system response to disturbances. The results are given in this section.

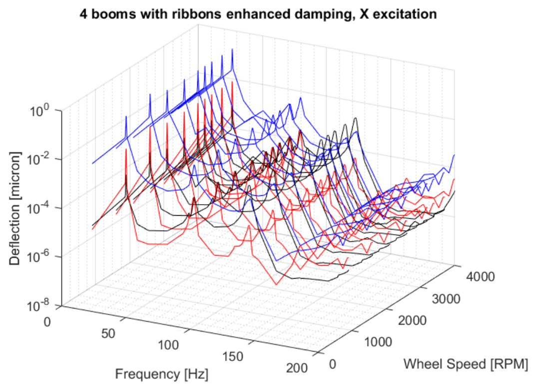

(a) X displacement of the four boom design with ribbons and enhanced damping due to disturbances in X direction as function of wheel speed and frequency.

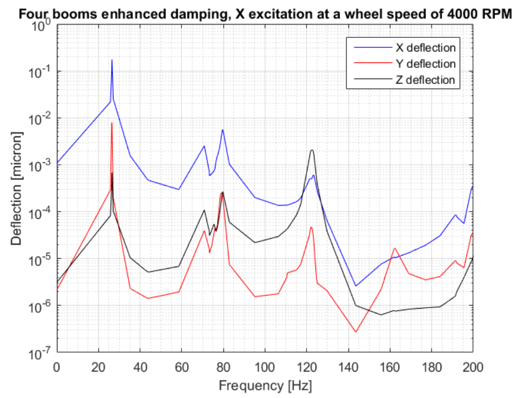

(b) Deformations of the four boom design with ribbons and enhanced damping due to disturbances in X direction as function of frequency at 4000 RPM

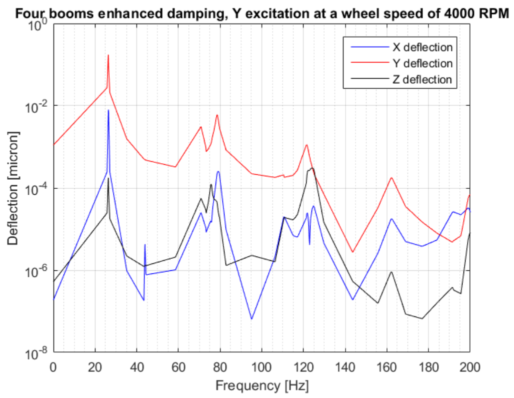

(c) Deformations of the four boom design with ribbons and enhanced damping due to disturbances in Y direction as function of frequency at 4000 RPM

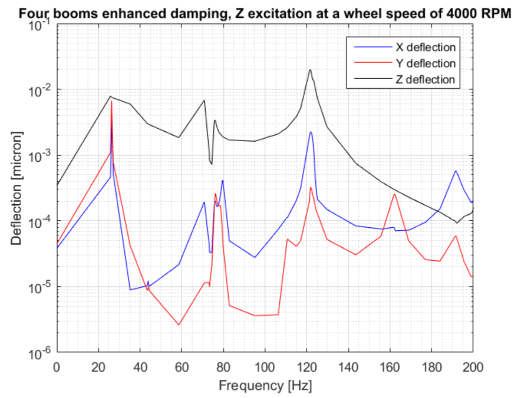

(d) Deformations of the four boom design with ribbons and enhanced damping due to disturbances in Z direction as function of frequency at 4000 RPM

Figure 11.13: Response of the four boom design with ribbons and enhanced damping to the RW45E reaction wheel.

As can be seen in Figure 11.13, the response of the system to an excitation in X and Y direction are similar. The maximum occurs at around 26.4 Hz, with an amplitude of 0.174 micron at a wheel speed of 4000 Hz. However, at a wheel speed of 1600 RPM, the first wheel order disturbance frequency equals that of the first eigenmode of the system, and the amplitude of the response is 0.337 micron. In the hand calculations this response was 0.8 microns. The same reasoning for explaining the difference between the results is used as in the normally damped model discussed before.

The ratio between the enhanced damped response and normally damped result in ANSYS is 0.337/0.73 = 0.46, while for the hand calculations it is 0.8/1.9 = 0.42. The difference between the normally damped and the enhanced damped model as calculated by ANSYS and hand calculations are close. This verifies the ANSYS results further. It cannot be stated too much that test have to be performed to validate the simulation results.

Design Comparison

In order to compare the different designs better, the responses are plotted in one figure. This is done for the X response due to an X excitation, the Y response due to a Y excitation, and Z displacement due to a Z excitation, see Figure 11.14.

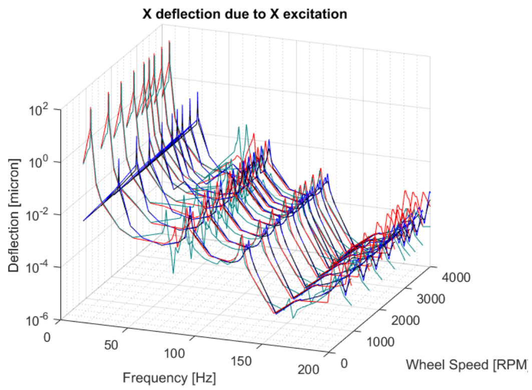

(a) X excitation

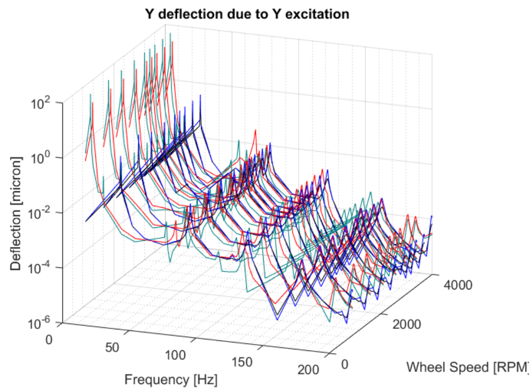

(b) Y excitation

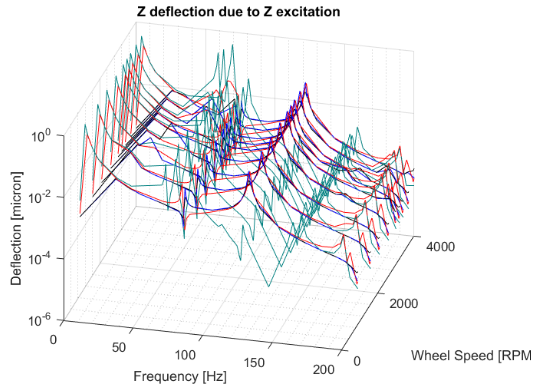

(c) Y excitation

Figure 11.14: Responses of the models to the disturbances of the RW45E reaction wheel

In order to compare the systems properly, also a figure was created of the disturbances at a wheel speed of 4000 RPM, see Figure 11.15.

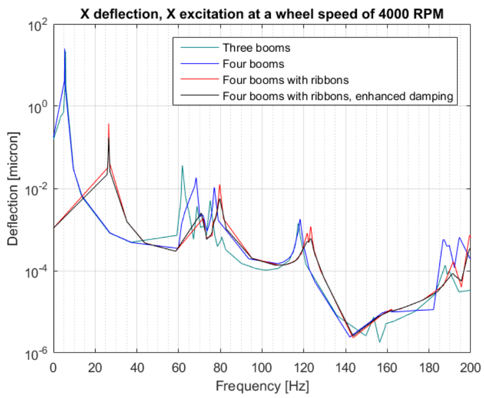

(a) X excitation

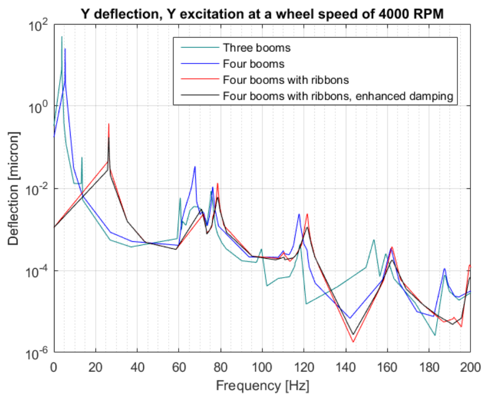

(b) Y excitation

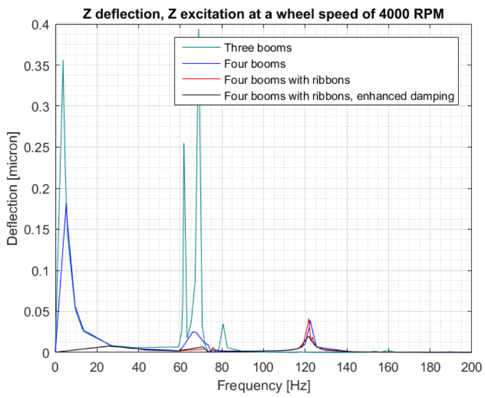

(c) Z excitation

Figure 11.15: Responses of the models to the disturbances of the RW45E reaction wheel at a wheel speed of 4000 RPM

From Figure 11.15, several conclusions can be drawn. First of all, the designs without ribbons show similar behaviour. Both have a low eigenfrequency and a high response at around 5 Hz. When excited in the X direction, the systems have a comparable response with an amplitude in the order of 20 micron. When excited in the Y direction however, the maximum response amplitude of the three boom system is about twice as large as the four boom design response. Another observation is that the response of the three boom design to a Z excitation is larger compared to the other designs. This is especially true for the range of 60-80 Hz. This can be explained by the lack of symmetry in the three boom system.

Comparing the systems with and without ribbons, it can be concluded that the ribbons have two effects. The first effect is that the first eigenfrequencies are increased to around 26 Hz. The second effect is the reduction in amplitude of the maximum response. The maximum response of the four boom system is decreased from 25.4 to 0.73 micron by adding the ribbons. This is further decreased to 0.337 micron by enhancing the damping of the CFRP.

11.4.7. Harmonic Analysis Conclusion

In this section, the harmonic analysis of the system was discussed. Several conclusions were drawn. The most important conclusion is that the first eigenmode determines the maximum deformation of the system. The amplitudes at higher frequencies, even if these frequencies are also eigenmodes, is less than the amplitude at the first eigenmode. The second conclusion that can be drawn is that the three boom design responds in a asymmetric way. Due to the asymmetry in the design, the responses to an excitation in X and Y direction are not equal, and the difference between the maximum is about a factor of two. The third conclusion is that the ribbons are reducing the maximum deflection of the system from 25.4 to 0.73 micron. From this it can also be concluded that the maximum deflection in the three boom design is about 50 times over budget. The maximum deflection of the four boom system without ribbons is about 25 times larger than the given optical budgets. Both the four booms with ribbons and the four booms with ribbons and enhanced damping do fulfil the optical budgets.

It can thus be concluded that adding the ribbons to the design, and thus increasing the number of booms to four, is beneficial for the stability of the DST. With the ribbons in place, the system can fulfil the given optical requirements under the used disturbance levels, where the designs without the ribbons cannot fulfil these requirements.

11.5. Conclusion

In this chapter, the effect of ribbons to the design was investigated. First, the layout of the ribbons was determined. In previous chapters, the ribbons were connected to the centre of the spider and were thus in plane with the boom and the spider. In order to also include rotational stiffness it was decided to span the ribbons between the top hinge and the M1 support structure. The ribbons would then fulfil a double role since they will also provide the required preload to the kinematic interface of the primary mirror segments.

The effect of the stiffness of the ribbons on the system was investigated using a modal analysis, while varying the ribbon stiffness. It was concluded that increasing the ribbon stiffness does increase the eigenfrequencies of the system. The increase is especially large at low ribbon stiffness. The effect of added ribbon stiffness is less prominent at a higher ribbon stiffness. This was explained by the fact that the structure starts to resonate in a way which is not affected by the ribbons.

During the modal analysis, the ribbon stiffness did not necessary represent a real ribbon. M. Corvers, which designed the primary mirror support structure, determined that the maximum stiffness that still works with his design was 750 N/mm. This value was used for the harmonic analyses.

The spectrum used for the harmonic analysis was based on a spectrum found in a paper, coming from the Bradford RW445E reaction wheel. The spectrum was applied to five models. It was concluded that both the three and four booms without ribbons concepts reacted similarly, although did the three boom concept have higher amplitudes when excited in the y direction. The maximum amplitude of the four boom concept was 25.4 micron, while that of the three boom concept was 50 micron. This means that both concepts are above the optical stability budget.

The four booms with ribbons concept had a maximum deflection of 0.73 micron under the applied excitation. This is a significant reduction compared to the concepts without ribbons. To test the effect of enhancing the damping capabilities of the CFRP the boom is made of, a model was made with four booms and ribbons and a higher constant damping ratio. The result was a further reduction in the maximum amplitude to 0.337 micron. Enhancing the damping capabilities of the CFRP is thus effective in reducing the vibration response of the system.

Based on the results, it was concluded that introducing ribbons, and with that a fourth boom, to the design is beneficial for the vibration stability of the system. Based on these conclusions, it was decided to change the system design to a four boom system with ribbons. The effect of the introduction of a fourth boom to the thermal behaviour of the system still has to be investigated.

III

Conclusions & Recommendations

12
Final Design & Performance

In the previous chapters, the design of the SMSS was discussed. The design process was described in a chronological order and since the process was iterative, it is easy to get lost in the details and loose the overview of the design. In this chapter, the final design is presented. After that, the performance of the design is checked if it fulfils the requirements given in Chapter 3.

12.1. Final Design

In this section, the final design of the SMSS is presented. In figure 12.1, a render of the entire instrument is given, including the PMSS. In the renders, the ribbon winches are clearly visible. After the overview is provided, the different components are discussed in more detail.

12.1.1. M2 and M2 Interface

In this thesis, the design of the secondary mirror itself is not discussed. Currently no weight optimisation of the mirror is performed. the topology of the mirror will be optimised later in the DST project. For now, a weight reduction of 70% was assumed, based on [4, 67].

The interface between the mirror and the spider was selected to be a hexapod structure. Since each rod has to constrain only one DOF, slots were made into the rods. The hexapod design allows for relative thermal expansion of the spider and the mirror, while keeping the mirror exactly constraint. The material of the rods was selected to be Aluminium 7075-T6. This material has a high reduced tensile strength, which is beneficial for flexures. The length of and material of the rods in combination with a boom with a CTE of 0.8 micron/m/K makes this system athermal. The mirror with its interface to the spider can be seen in Figure 12.2.

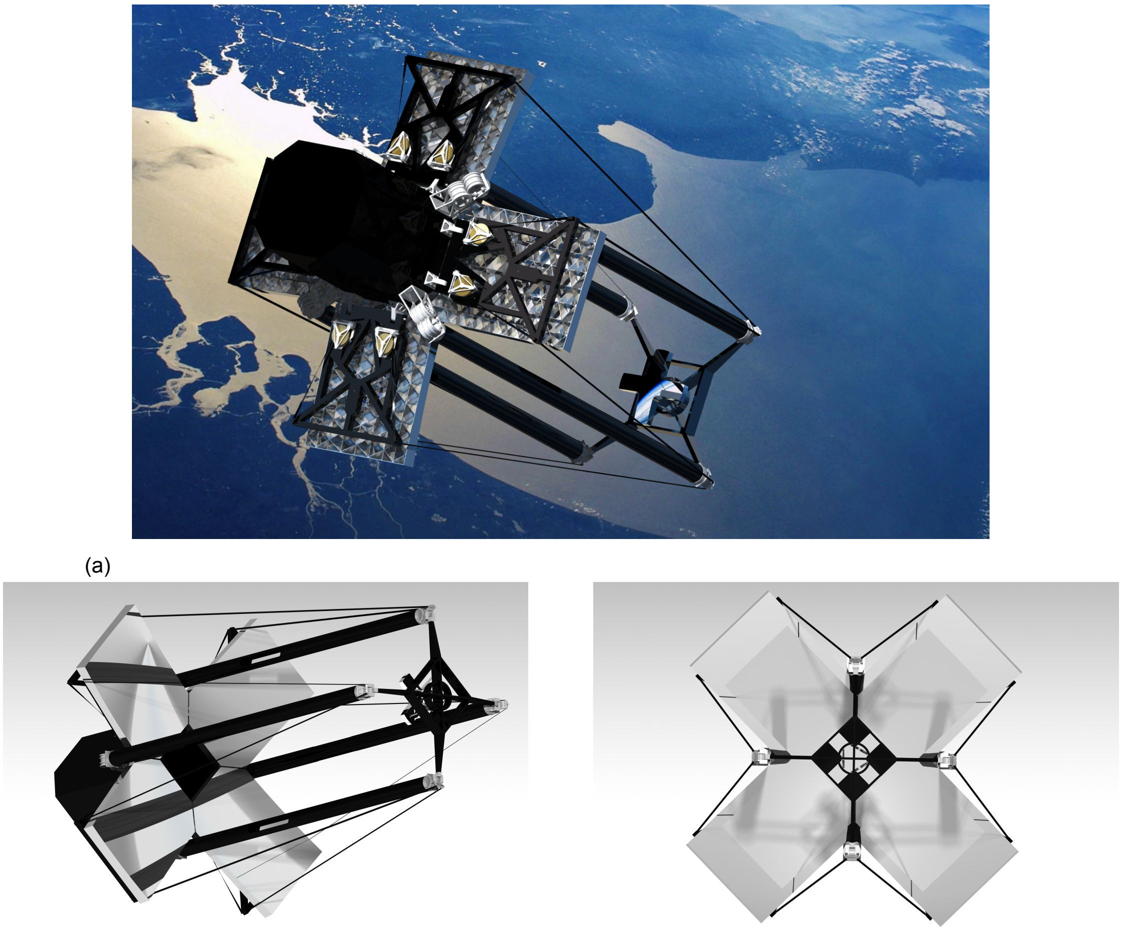

(a)

(b) (c)

Figure 12.1: Renders of the final model of the DST, as it was in June 2018

Figure 12.2: Render of the spider and the mirror interface

12.1.2. Spider

The spider is the structure connecting the booms via the mirror interface to the secondary mirror. In the last design iteration, the spider is basically a cross, connecting the four booms. At the centre of the spider, a circular structure is added. The mirror interface is mounted on this circular structure and the diameter of this structure was taken to be 2/3 of the diameter of the mirror. This was based on literature to minimise the effect of gravity on the mirror. When the exact mass distribution within the mirror is known, this value has to be updated. Besides the circular structure, there are four cross beams included in the spider design. The purpose of these beams is to increase the stiffness of the spider. The cross beams are at the edge of the primary mirror segments, and thus do not block any light.

The outer part of the spider was made wider to increase the stiffness of these parts. The width was set to 15 mm after a discussion with D. Dolkens. furthermore, the outer parts are made tapered, the height of the spider is decreasing towards the ends of the spider. The reasoning behind this is that the tips of the spider are connected to the hinges, which cannot transfer a moment over their rotation axis. The internal moment at the tips of the spider is thus zero. A render of the spider is given in Figure 12.3.

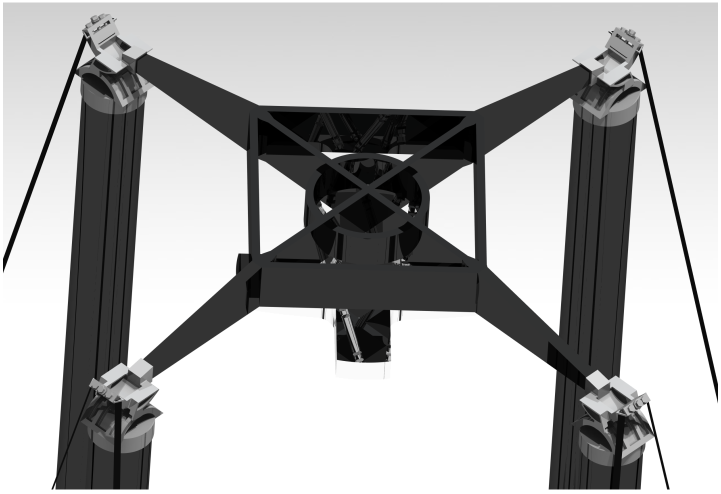

Figure 12.3: Render of the spider in final configuration.

12.1.3. Top and Root Hinges

The selected concept for the top and hinges was the CORE hinge type. The hinge was selected for its low hysteresis and friction behaviour, while forming a strong connection between the two parts in the directions other than the rotation axis. Due to the similarity between the hinges, both hinges were designed in parallel.

It was decided to use titanium Ti-6Al-4V as the material for the strips connecting the two cams. The strips are rolling over a cylinder with a radius of 29.7 mm, while cylindrical areas where the two cams touch has a radius of 35 mm. This difference makes it possible to create a preload normal force between the cams. This is required to ensure the cams do not separate during launch.

Three parameters were selected to be used as design optimisation parameters. These were the total width of the strips, the cam inner radius, and the metal strip thickness. An optimal point was found using a simple grid search.

The preload on the strips is provided by a bolt in combination with belleville washers. This setup ensures a stiff connection between the strip and the cam, while having a precise preload on the flexures with relative low sensitivity to environmental influences. An overview of the design parameters is given in Table 12.1.

The ribbons spanning from the PMSS to the SMSS are connected to the top hinges. Due to possible manufacturing difficulties, the root hinge was divided in several components. Figure 12.4 gives the renders of the two hinges. Note that in Figure 12.4b, the winch system for the ribbons as created by M. Corvers is also visible.

Table 12.1: Overview of the general dimensions of the CORE hinges.

Parameter	Dimensions [mm]
Strip thickness	0.3
Strips total width	31
Outer radius cams	35
Inner radius cams	29.7
Fillet radius	0.5
Cam contact surface width (total)	20
Total width	54
Bolt size	M4

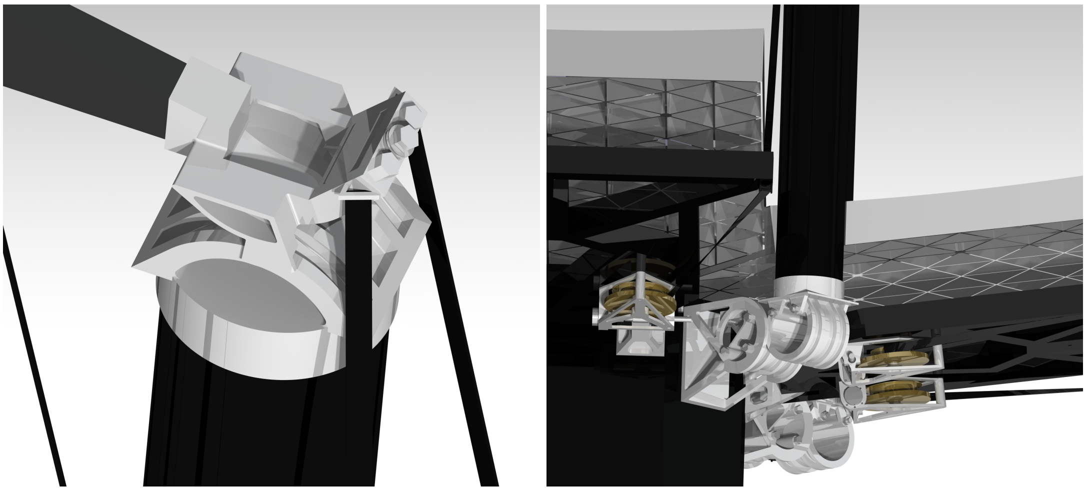

(a) Top hinge (b) Root hinge

Figure 12.4: Renders of the top and root hinges in the final design.

12.1.4. Booms and Mid Hinges

The booms and the mid hinges are one structural part. The booms have a diameter of 70 mm, with a wall thickness of 0.5 mm. The boom is made from CFRP. The hinging of the boom occurs by elastically deforming the slotted area of the boom. The layup of the boom has not been determined yet. The layup will dictate the properties of the boom, and thus also the mid hinge. The outer dimensions of the boom have been determined, together with the required CTE. The CTE was set to 0.8 micron/m/K, which is believed is achievable. This CTE was used within the athermalisation of the SMSS. A change in CTE of the boom requires a different length of the rods in the mirror interface. Only the deployment torque is still unknown and has to be investigated in the future. The required deployment torque depends mainly on the internal friction in the system and the required deployment kinematics. The parameters are given in Table 12.2.

Table 12.2: Design parameters for the booms with integral slotted hinges.

Parameter	Value
Diameter [mm]	70
Wall thickness [mm]	0.5
Total length [mm]	1765.7
Midpoint hinge [mm]	658
CTE [micron/m/K]	0.8
Deployment torque [Nm]	[TBD]

12.1.5. Ribbons

In the first modal analyses, it was observed that in the modal shape of the first eigenfrequencies the spider translates. The introduction of ribbons spanning from the PMSS to the top hinges of the SMSS should decrease the movement of the spider in the first eigenmodes. The ribbons were made out of Kevlar® and were given a width of 8 mm and a thickness of 1 mm. This resulted in a ribbon stiffness of 750 N/mm. The sizing of the ribbons was performed by M. Corvers, since the ribbon design was mainly constraint by the PMSS. The concept was tested with an harmonic analysis in ANSYS. The ribbons reduced the response amplitudes from 25.4 to 0.73 micron.

12.1.6. Mass

The design of the SMSS is currently already in a detailed stage. Based on the CAD models made and the materials chosen, a mass estimate of the entire system can be made. The overview of the mass of the components in the system is given in Table 12.3. It is concluded that the total mass of the system is about 7.8 kg. In this estimate, the mass of the bolts needed within the system is included. The mass of the adhesives is not included, although it is expected that the combined weight of the adhesives will be a few grams at most. Furthermore, the interface to the instrument bus had not been designed yet, which can alter the weight of the system.

Table 12.3: Overview of the mass of the final design of the SMSS.

Component		Subassembly		Full Assembly	
Subassembly	**Part**	#	**Mass/piece [kg]**	#	**Mass [kg]**
Root hinge					
	Bus interface	1	0.305	4	1.22
	Cams bus side	1	0.237	4	0.948
	Tension block	1	0.022	4	0.088
	Tension bolt	3	0.002	12	0.024
	Cams boom side	1	0.228	4	0.912
	Boom interface	1	0.111	4	0.444
	M5 bolt	5	0.013	20	0.26
	M5 nut	5	0.002	20	0.04
	Outer strip	2	0.001	8	0.008
	Inner strip	1	0.004	4	0.016
	Total		0.991	4	**3.964**
Top hinge					
	Cams boom side	1	0.163	4	0.652
	Cams spider side	1	0.086	4	0.334
	Tension block	1	0.012	4	0.048
	Tension bolt	3	0.002	12	0.024
	Outer strip	2	0.001	8	0.008
	Inner strip	1	0.002	4	0.008
	Total		0.273	4	**1.092**
Boom		1	0.259	4	**1.036**
Spider		1	0.584	1	**0.584**
Mirror interface					
	Rods	2	0.014	6	0.084
	Top plate	2	0.001	6	0.006
	Base plate	1	0.004	3	0.012
	Total		0.034	3	**0.102**
Mirror		1	1.01	1	**1.01**
Total					**7.8**

12.2. Design Performance

In Chapter 3, the requirements for the system were given. To check if the final design is compliant with the requirements, the design was checked. The result is given in Figure 12.5. The table will be explained in this section.

Based on the CATIA files, it was concluded that the total mass of the system is 7.8 kg, which is lower than the maximum stated mass of 14 kg, and thus the system complies with *M2-SYS-01*. Based on the model, the system will stay within the allocated space, and thus the system complies with *M2-SYS-03* and *M2-SYS-04*. In the model, it can also be seen that the mirror is indeed extended 1.6 m above the vertex of the primary mirror segments, and the system complies with *M2-MEC-01*.

In Figure 12.5, it can be seen that behind the requirements concerning the deployment and drift budgets TBC is written. This stands for To Be Confirmed. No thermal or deployment analysis have been performed, so no conclusions about the performance on these requirements can be drawn. It is however thought that the deployment budgets can be reached. This because all hinge concepts have low hysteresis. They all depend on elastic deformation or pure rolling contacts. These forms of deformation/relative motion have very little hysteresis. This means that the repeatability of the system as a whole will be high. However, before tests are performed, no hard evidence can be provided, and thus it cannot be stated that the system complies with the requirements. The requirements *M2-MEC-08, M2-MEC-09, M2-MEC-16* and *M2-MEC-17* are requirements concerning the M2 mirror itself. This thesis did not focus on the design of the M2 mirror, and are currently not really relevant to the SMSS. This automatically means that it can currently not be checked if these requirements are met.

The compliance of the system with the requirements on the stability (*M2-MEC-18* to *M2-MEC-24*) is proven with the results given in Chapter 11. Although it must be stated that actual test still have to be performed to validate the simulations.

The launch requirements are already checked if they are met for the top and root hinges, but not yet for the booms. The critical load case for the booms is buckling. The critical stress in circular booms is [2]:

$$\sigma_{cr} = \frac{\pi^2 EI}{Al^2} \tag{12.1}$$

Where σ_{cr} the critical stress is, E the young's modulus of the boom, I the area moment of inertia of the boom, A the cross sectional area of the boom, and l the length of the boom. The critical stress for this case is about 370 MPa. The stress within the booms can be calculated with:

$$\sigma_{eq} = \frac{P}{A} + \frac{2M}{AR} \tag{12.2}$$

Where P is the axial force (positive for compression), A the cross sectional area of the boom, M the moment acting on the boom, and R the radius of the boom. With the three load cases considered, the 30 G in the (X +Y), (Y + Z), (X + Z) directions, see Chapter 4, the highest stress within the boom is 150 MPa, which is lower than the critical buckling load. The launch requirements are met, except for requirement *M2-MEC-25-04* which still has to be confirmed. Since one of the child requirements are not confirmed yet, the parent requirement *M2-MEC-25* cannot be confirmed yet.

The AIT requirements, *M2-MEC-27* to *M2-MEC-29* are confirmed. By inspecting the design, it can be seen that all components of the SMSS can be produced using well known production methods, like CNC milling. Furthermore, the system allows for separate assembly of the SMSS components and thus the system does not interfere with other systems during this stage of development. The testing of the SMSS can be done without the need of replacing any components, since all moving components rely on elastic deformation and pure rolling contacts. The locking of the booms is achieved by the shape of the material and is fully reversible.

Old ID	New ID	Description	Compliant
		System	
R-M2D-GEN-3	M2-SYS-01	The total mass of the M2 mechanism shall be lower than 14 kg	Y
R-M2D-GEN-2	M2-SYS-02	The mechanism shall provide structural support for M2	Y
N/A	M2-SYS-03	The M2 mechanism in stowed configuration shall stay within the boundary box given by the primary mirror segments.	Y
N/A	M2-SYS-04	The M2 mechanism in stowed configuration height, including the instrument bus, shall be equall or less than 1.27m (goal)/2.55m (threshold)	Y
N/A	M2-SYS-05	The development, production, assembly, integration, and test cost of the M2 mechanism shall be equal to or lower than TBD	TBC
		Functionality requirements	
~~R-M2D-GEN-1~~		~~The mechanism shall extend M2 1.3m fromM1~~	
N/A	M2-MEC-01	The M2 mechanism shall deploy the M2 along the optical axis (Z axis) to obtain a distance of 1.6 m between M1 and M2, measured between the vertex of both mirrors	Y
~~R-M2D-STR-1~~		~~The deployed mechanism shall have a maximum deflection of 15 µm in the x- and y- direction, measured from the root~~	
~~R-M2D-STR-2~~		~~The deployed mechanism shall have a maximum deflection of 10 µm in the z-direction, measured from the root~~	
~~R-M2D-STR-3~~		~~The deployed mechanism shall have a maximum twist of 100 µrad about all axes, measured from the root~~	
N/A	M2-MEC-02	The M2 mechanism deployment accuracy shall be equal to or less than 15µm measured along the X axis of the telescope coordinate frame	TBC
N/A	M2-MEC-03	The M2 mechanism deployment accuracy shall be equal to or less than 15µm measured along the Y axis of the telescope coordinate frame	TBC
N/A	M2-MEC-04	The M2 mechanism deployment accuracy shall be equal to or less than 10µm measured along the optical axis (Z axis) of the telescope coordinate frame	TBC
N/A	M2-MEC-05	The M2 mechanism deployment accuracy shall be equal to or less than 100µrad measured around the X axis of the telescope coordinate frame	TBC
N/A	M2-MEC-06	The M2 mechanism deployment accuracy shall be equal to or less than 100µrad measured around the Y axis of the telescope coordinate frame of the telescope coordinate frame	TBC
N/A	M2-MEC-07	The M2 mechanism deployment accuracy shall be equal to or less than 100µrad measured around the optical axis (Z axis of the telescope coordinate frame)	TBC
N/A	M2-MEC-08	The radius of curvature of the M2 mirror shall change less than 0.01% due to the deployment of the mechanism	TBC
N/A	M2-MEC-09	The shape error of the M2 shall be less than 25 nm due to the deployment of the mechanism	TBC
N/A	M2-MEC-10	The M2 mechanism in-orbit drift shall be equal or less than 4 µm measured along the X axis of the telescope coordinate frame	TBC
N/A	M2-MEC-11	The M2 mechanism in-orbit drift shall be equal or less than 4 µm measured along the Y axis of the telescope coordinate frame	TBC
N/A	M2-MEC-12	The M2 mechanism in-orbit drift shall be equal or less than 2 µm measured along the optical axis (Z axis of the telescope coordinate frame)	TBC
N/A	M2-MEC-13	The M2 mechanism in-orbit drift shall be equal or less than 6 µrad measured around the X axis of the telescope coordinate frame	TBC
N/A	M2-MEC-14	The M2 mechanism in-orbit drift shall be equal or less than 6 µrad measured around the Y axis of the telescope coordinate frame	TBC
N/A	M2-MEC-15	The M2 mechanism in-orbit drift shall be equal or less than 12 µrad measured around the Z axis of the telescope coordinate frame	TBC
N/A	M2-MEC-16	The radius of curvature of the M2 mirror shall change less than 0.0001% due to in-orbit drift	TBC
N/A	M2-MEC-17	The shape error of the M2 shall be less than 5 nm due to in-orbit drifts	TBC
N/A	M2-MEC-18	The M2 mechanism stability shall be equal to or less than 1 µm along the X axis of the telescope reference frame	Y
N/A	M2-MEC-19	The M2 mechanism stability shall be equal to or less than 1 µm along the Y axis of the telescope reference frame	Y
N/A	M2-MEC-20	The M2 mechanism stability shall be equal to or less than 0.5 µm along the Z axis of the telescope reference frame	Y
N/A	M2-MEC-21	The M2 mechanism stability shall be equal to or less than 1.5 µrad around the X axis of the telescope reference frame	Y
N/A	M2-MEC-22	The M2 mechanism stability shall be equal to or less than 1.5 µrad around the Y axis of the telescope reference frame	Y
N/A	M2-MEC-23	The M2 mechanism stability shall be equal to or less than 3 µrad around the Z axis of the telescope reference frame	Y
R-M2D-STR-4	M2-MEC-24	The deployed mechanismshall have a minimum natural frequency of 5 Hz	Y
		Launch	
~~R-M2D-LAU-1~~		~~The stowed mechanism shall be able to withstand accelerations up to 30 g~~	
N/A	M2-MEC-25	The M2 mechanism shall be able to survive launch in the stowed configuration. Survival is defined as no impairment to the nominal functional capabilities of the system resulting from exposure to a given set of environmental conditions.	TBC
N/A	M2-MEC-25-01	The M2 mechanism shall be able to survive a quasi static acceleration of 30 G simultaniously applied in the X and Y direction in the telescope coordinate frame	Y
N/A	M2-MEC-25-02	The M2 mechanism shall be able to survive a quasi static acceleration of 30 G simultaniously applied in the Y and Z direction in the telescope coordinate frame	Y
N/A	M2-MEC-25-03	The M2 mechanism shall be able to survive a quasi static acceleration of 30 G simultaniously applied in the X and Z direction in the telescope coordinate frame	Y
R-M2D-LAU-2	M2-MEC-25-04	The stowed mechanism shall have a minimum natural frequency of 100 Hz	TBC
		Program	
R-M2D-GEN-5	M2-SYS-06	The M2 mechanism shall not contain ITAR related components	Y
R-M2D-GEN-6	M2-SYS-07	The mechanism shall comply with the Guiana Space Centre safety regulations	TBC
		Subsystem interfaces	
~~R-M2D-GEN-4~~		~~The mechanism shall have a minimumdeployment ratio of 2~~	
N/A	M2-MEC-26	The M2 system shall not come in contact or interfere with other subsystems during any mission phase	Y
N/A	M2-MEC-26-01	The M2 mechanism in stowed configuration shall not interfere with the interface between the launcher and the spacecraft	Y
N/A	M2-MEC-26-02	The M2 mechanism, with the exception of the spider, shall not block the light path of the M1 or M2 mirrors	Y
N/A	M2-MEC-26-03	The width of the spider of the M2 mechanism shall be 15 mm or less, covering no more than 3 mm of mirror of each segment	Y
N/A	M2-MEC-26-04	The M2 mechanism shall be connected to the outside of the instrument bus	Y
N/A	M2-MEC-26-05	The parts of the M2 mechanism covering part of the light path of the mirrors shall have a regular, predictable shape that minimises scattering	Y
	M2-MEC-26-06	The M2 system shall not interfere with the field stop, extending 120 mm form the M1 vertex	Y
		AIT requirements	
N/A	M2-MEC-27	The components of the SMSS shall be producable without the need to develop new production tools	Y
N/A	M2-MEC-28	The components shall be able to be assembled without interfering with other systems	Y
N/A	M2-MEC-29	The system shall be able to be tested on ground multiple times without the need to change permantly locked components	Y

Figure 12.5: Compliance matrix of the SMSS, based on the requirements stated in Chapter 3.

13 Conclusion

In the previous chapter, the final design of the secondary mirror support structure was given. It was the result of the work performed during this thesis, with as as purpose to answer the following research question:

How can the secondary mirror support structure of the Deployable Space Telescope project be designed such that it fulfils the optical alignment budgets?

In this chapter, the conclusions drawn in this thesis is summarised. After that, the research question will be answered.

Previous Design The previous design of the SMSS was made by J. W. Lopes Barreto for his MSc. thesis. In his work the focus lay on the trade-off between different deployment concepts for the secondary mirror. The hinges presented in his thesis were still in a conceptual design. In the way the hinges are installed in the design, the system cannot be stowed in the required configuration. The analysis performed in his thesis showed that the system did not fulfil the optical requirements.

Number of Booms To prevent the booms from colliding during stowage, it was suggested to increase the length of the spider. This results in that the booms in deployed condition will not be parallel. The hypothesis was that this new geometery could increase the stiffness of the structure, next to solving the stowage problem. However, results from the modal analyses performed in Chapter 8 show that the slight change in orientation of the booms did not have an effect on the eigenfrequencies of the system.

A design containing three booms instead of four booms was selected. This was done to prevent overconstraining the structure. The reduction of booms from four to three do not affect the stiffness significantly according to the results obtained in the analyses performed in the thesis. This was seen in both the modal analyses performed for the mid hinge trade-off in Chapter 7 and in the harmonic analyses based on a disturbance spectrum taken from the RW45E reaction wheel from Bradford in Chapter 11.
Although the effect of removing a boom on the stiffness of the system is limited, it was decided in Chapter 11 to abandon the three boom design and go back to the four boom design. The decision was based on the fact that the effect of adding ribbons to the design on the total deformations of the system during harmonic loading was significant. Due to the interaction with the primary support structure, a three boom design was not possible anymore. The conclusion was that the increase in stiffness and introducing symmetry in the design is favoured over exactly constrained design in this situation.

Flexures In Chapter 5 it was chosen to design the SMSS as an exactly constrained structure. When treating the booms as stiff members, flexures are needed to prevent the system from being overconstrained. These flexures are actively participating in the vibrations in resonance according to the results obtained in Chapters 7 and 8. Removing the flexures from the design has a limited effect on the first eigenmodes, but has a significant effect for the higher eigenmodes according to the results obtained in Chapter 8.

Another observation from these analyses is that the booms do not act as rigid bodies, and the first modes are dominated by the boom properties. In Chapter 8, the spider dimensions was also altered. With the new spider design, the booms are an order of magnitude less stiff than the spider. The flexibility of the booms has the thus same effect as the added flexures. Due to the lack of added value, the flexures were removed from the design. The connection between the hinge and the spider is thus a rigid connection.

Mid Hinge Design In the design made by J. W. Barreto the top, mid, and root hinges were spring actuated hinges with a hard stop. One of the recommendations he gave was to investigate the hinge design in more detail.

For the mid hinge, a trade-off was made. Three different concepts were selected for this trade-off: ball bearing hinges, strain energy hinges, and shape memory composite hinges (SMC). From literature, it was concluded that the SMC does not fulfil the deployment accuracy requirement. The result of the trade-off was that the integral slotted hinge, being a form of strain energy hinge, was the best option in this application. The thermal behaviour and its low mass were decisive features in this trade-off.

System Parameters In Chapter 7, a modal analysis was performed. The results of this analysis show that the width and height of the spider had a significant influence in the modal response of the system at higher frequencies. From this result, a new spider design was made. It was also shown that by locking the hinges, the stiffness of the system increases, but only by a factor of about two.
The main conclusion that can be drawn from the analysis is that the layout of the system, thus long thin booms, has the largest influence on the modal behaviour of the system.

Top and Root Hinges The top and root hinges were designed in more detail. The trade-off between the different concepts considered resulted in the selection of the CORE type hinge for both the top and root hinge. It was concluded that the combination of low hysteresis and high stiffness would increase the accuracy of the system.
From the equation for the stress state in the strip given in Chapter 10 it was observed that three parameters determine the stress state at a given load case. These parameters are the width of the strips, the radius of the cams, and the thickness of the strip. With this three parameters the top and root hinges were optimised.
From the equation for the stress state of the strip, it was concluded that the lowest stress level is reached when the difference in CTE of the cams and the strips are lowest. Since titanium was selected as material for the strip, the smallest strip width is reached with titanium cams and since a larger strip width will result in a larger, heavier hinge, titanium was selected as material for the cams.
According to the trade-off, the best option is to use a combination of a bolt and belleville washers to apply the preload to the strip.
Since both the cams and the strips are made from titanium, cold welding was a potential problem. Different surface treatments were investigated in Chapter 10 and a Keronite surface treatment in combination with a MoS_2 layer was selected for the cams of the hinges.

Ribbon Design In the results of the modal analyses performed in Chapters 7 and 8 it was observed that the spider moves significantly in the lower eigenmodes. The use of ribbons to prevent this motion was suggested. This suggestion was tested by running an harmonic simulation in Chapter 11. The results from this analysis show that the ribbons are effective in reducing the response of the system to base excitations. The maximum amplitude of the system was reduced from 25.4 to 0.73 micron by adding the ribbons. This reduction is enough to bring the system within the optical budgets.

The effect of damping was also investigated. By increasing the material loss factor from 0.008 for CFRP to 0.018, the amplitude of the peak responses of the system was reduced by almost a factor of 2.

The results of the harmonic analysis show that the response of the three boom system is less symmetric compared to the four boom systems: excitation in the X direction did not result in the same response as excitation in the Y direction. Furthermore, excitation in the Z direction resulted in a large response in the Y direction.

Conclusions The goal of this thesis was to answer the research question:

How can the secondary mirror support structure of the Deployable Space Telescope project be designed such that it fulfils the optical alignment budgets?

In this thesis, it was concluded that the budgets can be fulfilled by using an integral slotted hinge as mid hinge in the booms. Since the rotational DOF is provided by elastic deformation, the hysteresis within the hinge is very low, which is good for the deployment budget. The continuous thermal path and the fact that a flexible, high conductivity layer can be applied on this concept make the integral slotted hinge the best option for the mid hinge, thermally speaking.

It was concluded that by using CORE type hinges for the top and root hinges the system has the highest chance of reaching the deployment requirements, and with that, the optical budgets.The deployment error will probably be low due to the fact that the CORE hinges rely on elastic deformation and pure rolling motion, and have thus low hysteresis. This still has to be tested. Furthermore, the layout of the hinge will ensure that the system can survive launch.
It was concluded during the thesis that by introducing ribbons spanning between PMSS and the top hinges of the SMSS, the SMSS response to vibrations is significantly reduced, and can meet the optical stability requirements.

In short, the answer to the research question is thus: by designing the SMSS with integral slotted hinges as mid hinges, CORE hinges as top and root hinges, and ribbons spanning between the PMSS and the top hinges of the SMSS.

14 Recommendations

During this thesis, a lot of progress was made in the design of the SMSS. There is however still a lot of work to be done. In this chapter, the recommendations for future development of this system are given.

Thermal Design During this thesis, the thermal aspect of the design has not been covered in detail. It is recommended that more analysis is performed on this aspect of the design, especially since now the design has four booms again and is thus overconstrained. It is also recommended to investigate the use of pyrolytic graphite on the exterior/interior of the booms and other components of the system to increase the thermal conductivity, and with that reduce the gradients within the system. The pyrolytic graphite sheets are flexible, thus they do not interfere with the mid hinge. Since the hinges are only thermally connected via contact conductance, it is important to investigate a way to thermally couple the two halves of the hinges. This could be done with a flexible thermal strap for instance although this may introduce a required deployment torque.

The reduction of the gradients in the system reduces the thermal distortions. In combination with the athermal design of the system, the effect of temperature changes should be reduced. Even with the recommended use of the highly conductive pyrolytic graphite, gradients will be present within the booms when they are partially subjected to incoming heat fluxes. The use of a sleeve around the booms to minimise the gradients in the booms should be investigated. The heat flux is then absorbed by the sleeve, after which it is then partially radiated to the booms. This extra step in the heat transfer can result in a significant reduction in thermal gradients within the booms, especially when the radiation between the booms and the sleeves is minimised. Care must be taken that the sleeves are thermally insulated from the rest of the system. Furthermore, the sleeves must not be directly connected to both the root and top hinges to prevent the development of thermal stress within the system, resulting in the deformations that the sleeves had to prevent. A solution could be to make the sleeves from two parts, one connected to the top hinge, the other at the root hinge. The interface between the two parts could be similar to a spline joint used in drive shafts (the two parts having a different diameter, and one 'slides' over the other, preventing light/external heat fluxes from impinging on the boom, without imposing any loads on each other).

Apart from the booms, it was observed that the spider is subjected to incoming heat fluxes as well. In order to limit the influence of these heat fluxes on the system, a form of heat shield or thermal coating is required for the spider. This of course should not block the light for the primary mirror segments. By protecting the spider from thermal fluxes, the temperature of the spider itself will become more constant. Lowering the thermal fluctuations within the spider will decrease the gradients within the system. This in combination with an athermal design will decrease the thermal drifts of the system.

During LEOP, the system is not protected by the baffle. A detailed study on the temperature development in the system during this phase of the mission still has to be performed.

Boom Design In this thesis, the mid hinge was selected to be a integral slotted hinges. The overall system parameters have been set for this system, apart from the deployment torque. It is recommended to do a kinematic analysis in ADAMS or a similar software to investigate the deployment kinematics of the system, and to determine the required deployment torque.

Apart from that, the layup of the boom has to be designed in detail. The layup will determine both the deployment torque and the CTE of the booms. It is recommended to get back in touch with P. Greff to discuss further collaboration. This discussion was postponed due to the lack of design requirements for the boom, but since these requirements were determined during this thesis, talks about possible cooperation between the DST team and SpaceTech can be restarted.

Top and Root Hinge Designs It is recommended to produce a prototype of either one of the hinges or both to test the working principle of the hinge. When the working principle is proven, the hysteresis and friction within the hinge can be tested. This test can be done in combination with the tests of the mid hinge. Also the deployment of the booms can then be tested.

Since the hinges are all made out of the same material, cold welding is a potential problem. Tests with the suggested surface treatment have to be performed in order to verify that the surface treatment is effective against cold welding, both under impact and fretting.

It is further recommended to perform ultimate load tests, to verify if the hinge design can survive the load it was designed to take.

Another recommendation is to look into the adjustment of the hinges. Currently, it was decided to perform adjustments for production/assembly errors directly at the secondary mirror (although such a system was not included in the design yet). It could also be interesting to investigate if the hinges could be made adjustable. This could be done in a similar way as how the preload is applied to the system. The adjustment can take place at the outer strips since the inner strip is already used for introducing the preload to the strips.

Currently the hinges do not have hard stops. If the test on repeatability conclude that the system is not accurate enough, the use of hard stops within the hinges could be investigated. The booms can then be used to provide the nesting force by ensuring that the booms are slightly under bending when both hard stops are engaged. These hard stops can also increase the stiffness of the system in stowed configuration since the hard stops of the top hinges are engaged during launch.

Ribbons The current design has ribbons spanned between the PMSS and the SMSS. It is highly recommended to investigate what the effect of linking the two systems is on the stability and accuracy of both systems. If this link would be a problem, it is suggested to investigate the design of separate arms next to the primary mirror segments on which the ribbons to the SMSS can be attached. With the separate arms the ribbons can be kept in the design without linking the PMSS and the SMSS. The effect of preloading the ribbons after deployment on the system's repeatability also has to be investigated.

It is also recommended to look in the design of the ribbons. The material has a large influence on the effectiveness of the concept. Furthermore, a coating needs to be selected that both protects the ribbon fibres, allow for stowage, and has good optical properties.

It is very important that tests are performed to validate the vibration results obtained on both the models with and without ribbons. These tests do not necessarily have to be performed on the full models directly, but can first be performed on simpler test models to reduce the production time and cost. When these tests are successfully performed, full model tests can be performed. It is important that eventually tests on the full model are performed.

Spider The design of the spider can still be further optimised for mass and stiffness. Furthermore, the layup of the CFRP is still not known. This and the thermal properties of the spider have to be investigated in more detail. Furthermore, the production method of the spider still has to be investigated.

It is also suggested to change the name of the spider into the spider web, since the shape of the spider looks more like a spider web than a spider.

Mirror Interface The mirror interface is currently seen as the best position to perform adjustments, since the mirror position is directly adjusted. However, the current design is not adjustable and a new design should incorporate the adjustment function in the design. As stated before, the boom layup has to be determined. When the layup is known, the final CTE of the boom will be known. The mirror interface length has then to be updated to keep the system design athermal.

Mirror The design of the mirror was not part of this thesis. The mirror topology can be optimised for mass and stiffness. The effect of the mirror interface on the mirror surface under the applied thermal and launch loads has to be simulated and tested in order to check if the requirements on the mirror surface is met under these conditions.

Coatings and Materials It is highly recommended to look into the surface coatings for the system. These coatings are different from the surface treatments needed for the root and top hinge cams since the surface treatments in the hinges are to prevent cold welding. These coatings have the main task to keep the scattering to a minimal, and thus limit the amount of stray light in the system.
The effect of outgassing of the system on the alignment of the mirror, and on contamination of the system due to outgassing of materials still has to be investigated. This would be mainly a concern for the CFRP components.

Hold Down and Release Mechanism During launch the system has to be kept in stowed configuration. Currently, no investigation into the hold down and release mechanism (HDRM) was performed. It is thus recommended that this mechanism is investigated and designed in detail. The design will depend on the system behaviour during launch. The system eigenfrequency and modes in deployed configuration still have to be investigated, and these results will determine the design requirements on the HDRM.

A
Call with SpaceTech GmbH

Call with Pierrot Greff from SpaceTech GmbH, Immenstaad, Germany
Subject: Collapsible tube hinge (integrated slotted hinge)
Date: 20-11-2017

First of all, the hinge for the JUICE mission was not a standard product. It was a one off design. This is because the hinge design is highly depending on the use of the hinge (required stiffness, torque etc.)

Hinge size: The hinge for the JUICE mission was 40 mm round. However, the concept can be made for different sizes in this range (he suggested 40 – 60 mm was not a problem, smaller is definitely possible) The thickness of the system of the JUICE mission was 0.4 mm. The slotted area was about 20-25 mm long. However, this is highly dependent on the design.

Accuracy: when deployed, the system is very accurate. Micron level is definitely possible. When discussing the 10-15 micron deployment accuracy, he suggested that this would not be a problem at all. Submicron precision could become a problem (0.5 micron for example) Also in combination with the 1.6 m boom, accuracy was not a problem.

Stored energy: could be a problem. He asked if there is friction in the system. Without friction, the system will deploy, even though it can take some time due to large inertia and lower torque. The stored energy highly depend on the design of the hinge. Too much energy can cause overshoot, especially with a high inertia of the system. This can be prevented by including a damper on the mirror, or a hard stop in the system, although this would increase the mass. Overshoot is not dangerous in the sense that the torque will switch sign, and eventually the system will lock. However, it might be dangerous for hitting the spacecraft. During operations, when the load becomes too high, it might happen that the hinge collapses/breaks. However, when the load is removed, the hinge will lock again. This could happen during a high rate slew manoeuvre due to inertial forces. The chance increases with an increasing top mass.

Thermal: The hinge is part of the boom, thus actually the boom is made after which the slots are cut into the boom to create the hinge area. The layup of the material is 0°-(15-20°)/90°, 0.4 mm thick. The conductivity can be altered by using different fibres that have a better conductivity. The CTE can be altered a bit by varying the layup. There is a bit of room to change the layup. A CTE close to 0 can be possible. In folded condition, the CFRP will be under large local stress. At elevated temperatures, this can lead to creep. Room temperature is not a problem at all, it gets dangerous from around 100°C. After deployment, the temperature range is determined by the matrix (200-250°C depending on the matrix type). A fast deployment after launch is beneficial (less chance on creep etc.)

Stiffness: Highly dependent on the boom properties, and hinge cut-out. Before this can be determined, first the boom has to be designed in detail. A good first approximation would be to take the stiffness of the boom (without the hinge) and reduce the stiffness by 20% to account for the stiffness reduction due to the hinge. Then increase the boom diameter until the required stiffness is reached with a thickness <0.5 mm. (0.5mm is about the limit of the thickness with which the folding still can work.)

General remark: For now Pierrot cannot give more information, since that would require a deeper investigation into the project/case, and that costs money (it is a company of course). At this stage of the design there is not much know about the critical factors, which is very important for the final design. However, when the design is in a further stage (boom diameter, thickness, available budget :P etc.) he is happy to help, and can be contacted, either by mail (through original address that I already used) or by phone (saved number).

Bibliography

[1] D. S. Adams and M. Mobrem. Marsis antenna flight deployment anomaly and resolution. *47th AIAA/ASME/ASCE/AHS/ASC Structures, Structural Dynamics, and Materials Confere*, pages 1–9, May 2006. doi: 10.2514/6.2006-1684.

[2] J. Amdahl. *TMR4205 Buckling and Ultimate Strength of Marine Structures* . Norwegian University of Science and Technology, 2005.

[3] M. Bass, V. N. Mahajan, and E. Van Stryland, editors. *Handbook of Optics Volume II Design, Fabrication, and Testing; Sources and Detectors; Radiometry and Photometry*. Mc Graw Hill, third edition, 2010. ISBN 978-0-07162927-0.

[4] P. Y. Bely, editor. *The Design and Construction of Large Optical Telescopes*. Springer, New York, 2003. ISBN 0-387-95512-7.

[5] J. T. Black et al. Deployment repeatability testing of composite tape springs for space optics applications. *47th AIAA/ASME/ASCE/AHS/ASC Structures, Structural Dynamics, and Materials Conference*, May 2006. doi: 10.2514/6.2006-1905.

[6] A. Brinkmeyer, S. Pellegrino, and P. M. Weaver. Effects of long-term stowage on the deployment of bistable tape springs. *Journal of Applied Mechanics*, pages 011008–1 – 011008–11, January 2016. doi: 10.1115/1.4031618.

[7] C. Cai et al. Modelling of Material Damping Properties in ANSYS. `https://support.ansys.com/staticassets/ANSYS/staticassets/resourcelibrary/confpaper/2002-Int-ANSYS-Conf-197.PDF`. Accessed: June 2018.

[8] W. D. Callister and D. G Rethwisch. *Materials Science and Engineering SI Version*. John Wiley and Sons Ltd. (Asia), eigth edition, 2011. ISBN 978-0-470-50586-1.

[9] Q. Chen et al. Design and testing of a space deployable mechanism. *AIAA SciTech Forum, 4th AIAA Spacecraft Structures Conference*, January 2017. doi: 10.2514/6.2017-0176.

[10] D. D. L. Chung. Review materials for vibration damping. *Journal of Materials Science*, (36): 5733–5737, 2001.

[11] Solon Manufacturing Co. Belleville Spring Washers - Metric. `https://www.solonmfg.com/belleville-spring-washers/metric`. Accessed: April 2018.

[12] R. Destefanis et al. Space environment characterisation of kevlar®: Good for bullets, debris and radiation too. *11th International Symposion on Materials in a Space Environment*, September 2009.

[13] DigitalGlobe. WorldView-3, 2014. URL `http://worldview3.digitalglobe.com/`.

[14] DigitalGlobe. WorldView-4, 2015. URL `http://worldview4.digitalglobe.com/#/main`.

[15] DigitalGlobe. WorldView-2 Satellite Sensor, 2016. URL `https://dg-cms-uploads-production.s3.amazonaws.com/uploads/document/file/98/WorldView2-DS-WV2-rev2.pdf`.

[16] D. Dolkens. *A Deployable Telescope for Sub-Meter Resolutions from Micro Satellite Platforms*. Master's thesis, Delft University of Technology, 2015.

[17] D. Dolkens et al. Design and optimization of a deployable telescope for earth observation applications. *To be published*.

[18] J. L. Domber et al. Dimensional repeatability of an elastically folded composite hinge for deployed spacecraft optics. *Journal of Spacecraft and Rockets*, (5):646 – 652, September–October 2002. doi: 10.2514/2.3877.

[19] C. Dong and other. Evaluation of thermal expansion coefficient of carbon fiber reinforced composites using electronic speckle interferometry. *Optics Express*, (532), January 2018. doi: 10.1364/OE.26.000531.

[20] DuPont. Kevlar®Aramid Fiber Technical Guide, 2017.

[21] ECSS. ECSS-Q-70-71Q rev.1 Space product assurance. (June), 2004.

[22] R. Fata, V. Kradinov, and D. Fabricant. Flexure mounts for high-performance astronomical lenses. In *Proc. of SPIE*, volume 6269, page 62695T, jun 2006. doi: 10.1117/12.672634. URL http://proceedings.spiedigitallibrary.org/proceeding.aspx?doi=10.1117/12.672634.

[23] N. W. Frank and H-P Dumm. Deployment repeatability of a truss structure utilizing integral composite hinges. *AIAA SDM Conference*, September 2005.

[24] Hoch Technologie Systeme GmbH. Deployable Hinge for Articulated Deployable Boom System. https://www.htsdd.de/content/Raumfahrt_Deployment_Mechanisms.html, . Accessed: June 2018.

[25] SpaceTech GmbH. JUICE RIME Antenna. https://www.spacetech-i.com/products/satellite-equipment/juice-rime-antenna, . Accessed: June 2018.

[26] M. R. Hachkowski and C. D. Cox. Hinge assembly for deploying the petals of a sectored mirror of an optical space telescope, 10 2005.

[27] L. C. Hale and A. H. Slocum. Optimal design techniques for kinematic couplings. *Precision Engineering*, 25(2):114–127, apr 2001. ISSN 01416359. doi: 10.1016/S0141-6359(00)00066-0. URL http://linkinghub.elsevier.com/retrieve/pii/S0141635900000660.

[28] P. A. Halverson. *Multi-stable Compliant Rolling-contact Elements*. Master's thesis, Brigham Young University, 2007.

[29] P. A. Halverson, L. L. Howell, and S. P. Magleby. Tension-based multi-stable compliant rolling-contact elements. *Mechanism and Machine Theory*, pages 147–156, November 2008.

[30] S. Han and D. D. L. Chung. Mechanical energy dissipation using carbon fiber polymer–matrix structural composites with filler incorporation. *Journal of Materials Science*, (47):2434–2453, 2011. doi: DOI10.1007/s10853-011-6066-7.

[31] S. Henein et al. Flexure pivot for aerospace mechanisms. *In Proceedings of the 10th ESMATS / ESA*, pages 285–288, 2003.

[32] J. Herder and D. Brouwer. TU Delft ME46015 Precision Mechanism Design lecture slides, 2017.

[33] J. L. Herder, M. J. Horward, and W. Sjoerdsma. A laparoscopic grasper with force perception. *Min Invas Ther & Allied Technol*, (6):279–286, 1997.

[34] D. J. Inman. *Engineering Vibrations*. Pearson Education, third edition, 2009. ISBN 978-0-13-136311-3.

[35] A. Jeanneau et al. A compliant rolling contact joint and its application in a 3-dof planar parallel mechanism with kinematic analysis. *ASME Design Engineering Technical Conferences*, October 2004. doi: DETC2004-57264.

[36] Jeveka. Jeveka Catalogus 2018, 2018.

[37] J.-P. Jobin, H. S. Buddenberg, and J. L. Herder. An underactuated prosthesis finger mechanism with rolling joints. *ASME Design Engineering Technical Conferences*, October 2004. doi: DETC2004-57192.

[38] Nadeem Shafi Khan. *Generalized Statistical Tolerance Analysis And Three Dimensional Model For Manufacturing Tolerance Transfer in Manufacturing Process Planning*. Phd thesis, Arizona State University, 2011.

[39] S. Y. Kim et al. Effects of pzt particle-enhanced ply interfaces on the vibration damping behavior of cfrp composites. *Composites: Part A*, 2011. doi: 10.1016/j.compositesa.2011.06.014.

[40] W. J. Larson and J. R. Wertz, editors. *Space Mission Analysis and Design*. Microcosm Press and Kluwer Academic Publishers, third edition, 1999. ISBN 978-1881883104.

[41] D. G. Lee, S. Lee, and Y. Lee. Effect of precipitates on damping capacity and mechanical properties of ti-6al-4v alloy. *Materials Science and Engineering A*, (486):19–26, August 2007. doi: 10.1016/j.msea.2007.08.053.

[42] J. W. Lopes Barreto. *DEPLOYABLE SPACE TELESCOPE: Optimal Boom Design for High Precision Deployment of the Secondary Mirror*. Master's thesis, Delft University of Technology, 2017.

[43] Keronite International ltd. Surface solutions for superior wear protection. http://www.keronite.com/products/keronite-endure/. Accessed: June 2018.

[44] H. M. Y. C. Mallikarachchi and S. Pellegrino. Quasi-static folding and deployment of ultrathin composite tape-spring hinges. *Journal of Spacecraft and Rockets*, January-February 2011. doi: 10.2514/1.47321.

[45] H.M.Y.C. Mallikarachchi and S. Pellegrino. Optimized designs of composite booms with integral tape-spring hinges. *51st AIAA/ASME/ASCE/AHS/ASC Structures, Structural Dynamics, and Materials Conference*, pages 1–16, April 2010. doi: 10.2514/6.2010-2750.

[46] R. A. Masterson and D. W. Miller. *Development and Validation of Empirical and Analytical Reaction Wheel Disturbance Models*. Master's thesis, Massachusetts Institute of Technology, 1999.

[47] A. Merstallinger and M. Sales. *Assessment of Cold Welding between Separable Contact Surfaces due to Impact and Fretting under Vacuum*. ESA Communication Production Office. ISBN 978-92-9221-900-6.

[48] L. Minh Phu'ó'c. *Micro-disturbances in Reaction Wheels*. Phd thesis, Eindhoven University of Technology, 2017.

[49] M. Mobrem and D. S. Adams. Deployment analysis of lenticular jointed antennas onboard the mars express spacecraft. *Journal of Spacecraft and Rockets*, (2):394–402, March-April 2009. doi: 10.2514/1.36890.

[50] T. Y. Nai, J. L. Herder, and G. J. M. Tuijthof. Steerable mechanical joint for high load transmission in minimally invasive instruments. *Journal of Medical Devices*, September 2011. doi: 10.1115/1.4004649.

[51] T. G. Nelson, R. J. Lang, S. P. Magleby, and L. L. Howell. Curved-folding-inspired deployable compliant rolling-contact element (d-core). *Mechanism and Machine Theory*, (96):225–238, June 2015. doi: dx.doi.org/10.1016/j.mechmachtheory.2015.05.017.

[52] S. D. Nigam and J. U. Turner. Review of statistical approaches to tolerance analysis. *Computer-Aided Design*, (27):6–15, January 1995.

[53] ECSS Secretariat. *Space Engineering, Mechanical - Part 1: Thermal control*. ESA Publications Division, 2000. ISBN 1028-396X.

[54] J. E. Sighley and C. R. Mischke. *Mechanical Engineering Design*. McGraw-Hill Higher Education, sixth edition, 2001. ISBN 0-07-365939-8.

[55] M. J. Silver et al. Precision high-strain composite hinges for the deployable in-space coherent imaging telescope. *3rd AIAA Spacecraft Structures Conference*, pages 1–21, January 2016. doi: 10.2514/6.2016-0969.

[56] P. K. Singh, P. K. Jain, and S. C. Jain. Important issues in tolerance design of mechanical assemblies. part 1: tolerance analysis. *Proc. IMechE Vol. 223 Part B: J. Engineering Manufacture*, April 2009. doi: 10.1243/09544054JEM1304A.

[57] SKF. Producten. http://www.skf.com/benelux/nl/products/index.html. Accessed: March 2018.

[58] B. Sundström, editor. *Handbook of Solid Mechanics*. Instant Book AB, Stockholm, first edition, 2010. ISBN 978-91-972860-4-6.

[59] T Tanimoto. Carbon-fiber reinforced plastic passive composite damper by use of piezoelectric polymer/ceramic. *Japanese Journal of Applied Physics*, (41):7166–7169, November 2002. doi: 10.1143/JJAP.41.7166.

[60] T Tanimoto. A new vibration damping cfrp material with interlayers of dispersed piezoelectric ceramic particles. *Composites Science and Technology*, 2006. doi: 10.1016/j.compscitech.2006.08.022.

[61] R. Trento et al. Development of long deployable dipole antennas for sounder radars in thalesaleniaspace-italia. *31st AIAA International Communications Satellite Systems Conference*, pages 1–10, October 2013. doi: 10.2514/6.2013-5650.

[62] B. T. van Putten. *Design of the Deployment Mechanism for the Primary Mirror Elements of a Deployable Space Telescope*. Master's thesis, Delft University of Technology, 2017.

[63] D. Vukobratovich and R. M. Richard. Flexure Mounts For High-Resolution Optical Elements. In *Proc. of SPIE*, volume 0959, pages 18–36, nov 1988. doi: 10.1117/12.947774. URL http://proceedings.spiedigitallibrary.org/proceeding.aspx?articleid=1253243.

[64] F. Wardle. *Ultra-precision Bearings*. Woodhead Publishing, first edition, 2015. ISBN 978-0-85709-162-8.

[65] P. A. Warren et al. Experimental characterization of lightweight strain energy deployment hinges. *46th AIAA/ASME/ASCE/AHS/ASC Structures, Structural Dynamics & Materials Conference*, April 2005. doi: 10.2514/6.2005-1809.

[66] D. H. Wiersma et al. Large stroke performance optimization of spatial flexure hinges. *Proceedings of the ASME 2012 International Design Engineering Technical Conferences & Computers and Information in Engineering Conference IDETC/CIE*, August 2012.

[67] P. R. Yoder. *Mounting Optics in Optical Instruments*. SPIE Press, second edition, 2008. ISBN 978-0-8194-7129-1.

[68] P. R. Yoder and D. Vukobratovich. *Opto-Mechanical Systems Design*. CRC Press, fourth edition, 2015. ISBN 978-1-4822-5770-0.

[69] J. Zhang, R.J. Perez, and E. J. Lavernia. Documentation of damping capacity of metallic, ceramic and metal-matrix composite materials. *JOURNAL OF MATERIALS SCIENCE*, (28):2395–2404, 1993 .